University of Reading

Department of Chemistry

# Density Functional Theory Studies of Metal-Based Interfaces

Jorge Eduardo Ontaneda Rojas

Thesis submitted for the degree of
Doctor of Philosophy

Supervisor: Dr Ricardo Grau-Crespo

August 2018

# Abstract

By employing state-of-the-art Density Functional Theory (DFT) simulations, and in tight collaboration with experimental research, the present doctoral thesis examines the properties of three types of metal-based functional interface. After two chapters containing a general introduction and a presentation of the theoretical methods, Chapter 3 discusses the geometry of adsorption of methyl acetoacetate (MAA) on Ni{111} and Ni{100} surfaces. A combination of X-ray photoemission spectroscopy (XPS), near-edge X-ray absorption fine structure (NEXAFS) and DFT simulations identified deprotonated enol species with bidentate coordination as the most stable adsorption complex of MAA on both Ni surfaces. In Chapter 4 the electronic structure of an unstrained metal-metal interface, Pd/Re(0001), is examined. The XPS spectrum of this interface is explained on the basis of the charge transfer occurring from the Re support to the *s-p* levels of Pd adlayers. A general analogy between the effects of charge transfer and strain is established for bimetallic interfaces. In Chapter 5, the electronic and vibrational properties of isolated and Ni{111}-supported hexagonal boron nitride (*h*-BN) monolayers are examined. It is shown that an isolated *h*-BN monolayer exhibits an intrinsic upshift in the Raman peak position with respect to its bulk value, which is caused by non-local (inter-plane) correlation effects. The intrinsic Raman signature in *h*-BN monolayers can be affected by thermal expansion (which partially "erases" it) and by a "direct" effect from the metal support (which increases the absolute Raman frequency of the supported *h*-BN monolayers). Our work demonstrates the excellent synergy between the theoretical and experimental investigation of metal-based interfaces.

# List of Publications

1. **Origin of the monolayer Raman signature in hexagonal boron nitride: a first-principles analysis**

   Jorge Ontaneda, Anjali Singh, Umesh V. Waghmare, and Ricardo Grau-Crespo

   *J. Phys.: Condens. Matter* **2018**, 30, 185701

2. **Combined Experimental and Theoretical Study of Methyl Acetoacetate Adsorption on Ni{100}**

   Panayiotis Tsaousis, Jorge Ontaneda, Luca Bignardi, Roger A. Bennett, Ricardo Grau-Crespo, and Georg Held

   *J. Phys. Chem. C* **2018**, 122, 6186

3. **Adsorption of Methyl Acetoacetate at Ni{111}: Experiment and Theory**

   Jorge Ontaneda, Richard E. J. Nicklin, Alix Cornish, Alberto Roldan, Ricardo Grau-Crespo, and Georg Held

   *J. Phys. Chem. C* **2016**, 120, 27490

4. **Electronic Structure of Pd Multilayers on Re(0001): The Role of Charge Transfer**

   Jorge Ontaneda, Roger A. Bennett, and Ricardo Grau-Crespo

   *J. Phys. Chem. C* **2015**, 119, 23436

To Joana and Daniela…

# Declaration

I confirm that this is my own work and the use of all material from other sources has been properly and fully acknowledged.

Jorge Eduardo Ontaneda Rojas

# Acknowledgments

Every undertaking in life requires sources of inspiration and support, and this one of course is not the exception. I have found such sources in the people nearby, who made of this journey a truly fruitful experience. And although it is impossible to list everyone, those missed here will always have my greatest respect and gratitude.

First and foremost, I would like to express my sincerest gratitude to my PhD supervisor, Dr Ricardo Grau-Crespo, for his support and encouragement throughout this stage of my life. His mentoring has been tremendously inspirational and his academic excellence made of my PhD a success. I could not have envisaged a better mentor, thank you Ricardo.

I am grateful for the support of my second supervisor, Dr Roger Bennett, who has been a constant source of advice and ideas. I am sure that this thesis would not have been possible to happen without his help. I also would like to thank the experimental groups in the Department, in the person of Prof Georg Held, who provided me new angles to run simulations and to interpret results. I could not have been happier with the work done in close collaboration with his group.

My gratitude also goes to Dr Silvia Gonzalez, my former supervisor and now my friend, who initiated me into this fantastic world of simulation of materials. Her mentoring prior this journey was essential; I would not have been here without her advice and guidance.

I would like to express some words toward the collaborators of our group. To Prof Umesh Waghamare from JNCASR in India, for his support and encouragement during my visit to his group. He is truly encouraging. To Dr Fransis Viñes and Dr Fransis Illas, from the University of Barcelona, for their supportive help in the last stage of my PhD.

This PhD would not be possible without the financial support from the National Secretariat for Higher Education, Science, Technology and Innovation (SENESCYT) of Ecuador, under the scholarship program "Convocatoria Abierta 2012 segunda fase". Computational time given by ARCHER, the U.K.'s national high-performance computing service, is also acknowledged.

There are many people to whom I owe a lot. I would like to say thanks to the members of the group, Victor and Scott, and Alex who left us recently. To the guys I met in Reading: Edna, Nataly, Diego R., Nayer, Diego F., Jesus, Ana, Diego M., and Sarah. To my forever friends in Loja: Ricardo, Julia, Patricia, Juliana, Jhoanna, María Cristina, Paola, José and Daniel. To those ones I met in the ITSDAB and in the UTPL. You guys are the best. Last but not least, to Richard and Luis; I will be always grateful for your honest support. I hope to work together again in the near future.

Finally and most importantly, I want to dedicate this thesis to my parents, Bolívar and Digna, and to my brothers, Fabián and Pablo. I have received nothing but unwavering support and uncompromising love from you, and I hope this makes you proud. My last lines go to Joana, my wife, and Daniela, my daughter. I cannot be grateful enough for the enormous belief and encouragement of you both, and none of this would have been possible without you being here.

# Table of Contents

‘They float, Georgie, and when you’re down here with me, you’ll float, too’

– Pennywise the Dancing Clown

*It* by Stephen King

# 1 Introduction

## 1.1 GENERAL SCOPE: INTERFACES

Some of the most significant physical and chemical processes in nature occur on surfaces and interfaces. They are highly critical in dictating the properties of many engineered materials such as gas sensors, surface protectors, nanostructured materials and catalysts. The underlying principles of solids surfaces and interfaces are the main subject of the broad field of Surface Science, whose aim is the study of physical and chemical phenomena that happen at either the interface of two phases (solid-liquid interfaces, solid–gas interfaces, solid-vacuum interfaces) or same phase (solid-solid interface). It is not surprising that Surface Science involves concepts related to heterogeneous catalysis, as important adsorption and reaction mechanisms of molecules occur on catalytically active surfaces. Therefore, a vast amount of work has been devoted to the understanding of the electronic and geometrical structure of catalyst surfaces.[1]

In solid materials, an interface is a two-dimensional defect consisting of planes of atomic sites where the solid meets another environment. A solid surface can be seen as a simple type of interface, in which the solid is in contact with the surrounding world. For instance, a thin film solid deposited on a substrate is bounded by a solid-solid interface and by the film-vacuum interface, and the properties of such a thin film are basically determined by the properties of its two interfaces.[2] Chemical, electronic, mechanical and other properties are determined by the tendency of atoms on either side of the interface plane to rearrange themselves to restore their bonding environment.[3] Therefore, a central topic in surface science concerns the interrelation between the interfacial properties and the underlying structure. Such knowledge has led to significant technological advances in the last decades.[4]

Solid-based interfaces can be classified into homogeneous (grain boundaries), and heterogeneous (those between two different solids, or between a solid and a different phase).[1] Metal-based heterogeneous interfaces are the subject of this thesis, and a brief discussion regarding a few general cases of this type of interface is given below.

### 1.1.1 Metal surfaces–molecules (in gas or liquid phase)

The self-assembly of organic molecules on metal surfaces is controlled mainly by the interplay between the molecule-molecule and molecule-surface interactions.[5] The latter, in particular, is a highly-active topic of research in the field of heterogeneous catalysis. In general, the heterogeneous catalytic reactions happen in five well-defined steps: i) diffusion of reactants from the gas/liquid phase to the surface of the catalyst; ii) adsorption of the reactants molecules onto the catalytic surface; iii) the catalytic reaction takes place; iv) desorption of products from the surface of the catalyst; v) diffusion of products into the gas/liquid phase.[6]

The adsorption of molecules at surfaces is a phenomenon of crucial importance in heterogeneous catalysis. The surfaces of a metal (and any solid in general) tend to adsorb molecules and/or atoms because the surface atoms have less neighbors compared to those in the bulk, so usually the addition of interactions is favorable. The strength of the metal-molecule interaction defines two types of adsorption. In *chemisorption*, the strength of the interaction between adsorbates and the solid is large enough to be considered as a chemical bond and typically involves adsorption energies above 20 kJ mol$^{-1}$ (in absolute value). In the second type, *physisorption*, the main contribution comes from van der Waals (vdW) interactions and typically involves much lower adsorption energies.[6,7]

A vast amount of work has been devoted to the understanding at molecular-scale of chemical reactions catalyzed by a metal surface.[1] One particular area of wide interest, where active research efforts are taking place, is that of enantioselective reactions catalyzed by base metals. Most of the current knowledge in this topic refers to the asymmetric hydrogenation of C=O bonds in ketoesters over modified surfaces of Ni,[8] and the asymmetric hydrogenation of C=C on Pd.[9] In these systems, chiral modifiers are used to alter the otherwise achiral heterogeneous catalytic process.[10] Undoubtedly, determining the adsorption geometry of the reactants at molecular level is a key step to understand and optimize the enantioselective behavior of metal-based catalysts.

### 1.1.2 Metal–metal interfaces

The properties of metal-metal interfaces, including morphology, film growth, friction, and bimetallic adhesion, are of interest in many metallurgical applications.[11] In the field of heterogeneous catalysis, research on noble metal-based nanocatalysts has provided important basis for the modeling of structure-dependent catalysis,[12] which in turn has delivered new composites that are essential in modern catalytic processes. In such composites, structural and geometrical modifications with respect to bulk environments play a key role. The most common pathway to achieve improved catalytic performances is by mixing metals to form alloys or composites. Typical cases include core-shell nanoparticles (in which a reactive outer skin is supported on a core metal) and ultrathin films (atomically thin layers of a metal supported on another metal), the latter being the simplest way to create new materials with properties different to that of the metal bulk.[13,14]

The peculiar properties of ultrathin bimetallic films and their important applications are still a rich landscape of research.[15]

The electronic properties of bimetallic interfaces, as well as of metal surfaces in general, are often described in the context of the so-called *d*-band model,[16] which we will use in Chapter 4 in the investigation of Pd/Re interfaces. The relative position of *d*-band center with respect to the Fermi level is an important theoretical parameter in this model to characterize the reactivity of metal surfaces. The *d*-band model establishes that the binding energy between an atom or molecule (adsorbate) and a transition-metal or noble-metal surface is largely dependent on the electronic structure of the surface itself. According to this model, the adsorbate-metal interaction energy has two primary contributions. The first of these is the interaction between the filled *s* states of the adsorbate with the empty metal *s* band which, according to Molecular Orbital Theory, results in the creation of a deep-lying ($\sigma$) bonding state and an empty ($\pi^*$) antibonding state. The second contribution comes from the interaction of these states with the metal *d* states.

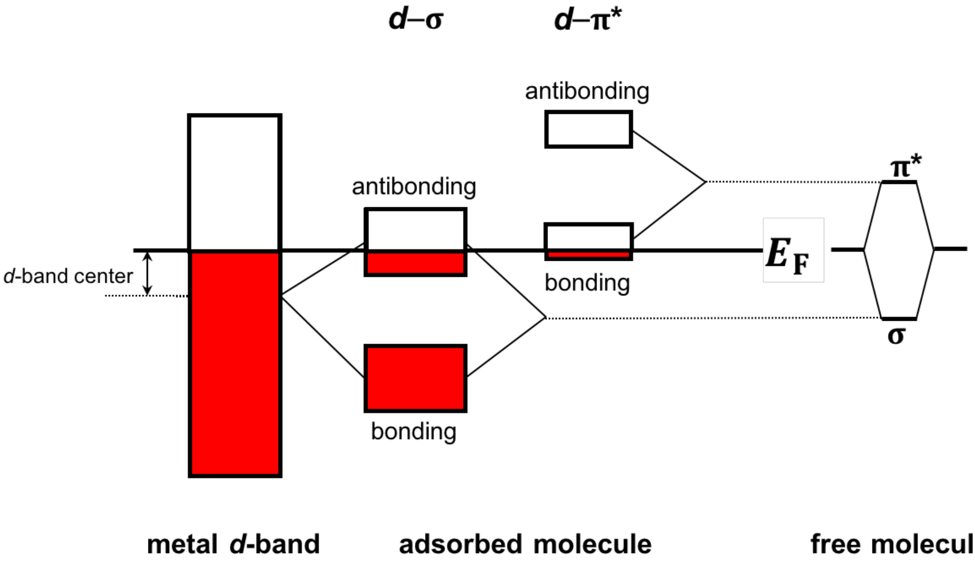

**Figure 1.1** Schematic representation of the *d*-band model proposed by Hammer, Nørskov, and collaborators.[16]

As illustrated in **Figure 1.1**, the hybridization of the metal *d*-band with the bonding ($\sigma$) orbital of the adsorbate results in the formation of bonding and antibonding (*d*–σ) states. In a similar fashion, the metal *d*-band interacts with the antibonding (π*) orbital of the adsorbate to form also bonding and antibonding (*d*–π*) states. The bonding (*d*–σ) state is full, while the extent of filling of the remaining ones depends on the surface electronic structure of the metal, i.e. the relative position of the *d*-band center. If we assume a constant degree of filling of the *d* band, it is apparent that a higher *d*-band center (with respect to the Fermi level) corresponds to a decrease in filling of both antibonding states, and an increase in the filling of the bonding (*d*–π*) state. Consequently, the metal-adsorbate system is less destabilized, resulting in a stronger interaction energy between the metal and the adsorbate. Conversely, a lower *d*-band center corresponds to a weaker metal-adsorbate interaction. In summary, a higher *d*-band center (smaller $E_\mathrm{d} - E_\mathrm{F}$ ) results in stronger bonding whereas a lower *d*-band center (larger $E_\mathrm{d} - E_\mathrm{F}$) means weaker bonding in the context of chemisorption of molecules to a metal surface.[17,18]

An important feature of the (*d*–σ) and (*d*–π*) states has to do with the direction of the charge transfer between the adsorbate and the surface metal. The (*d*–σ) states results in a net charge transfer from the adsorbate to the metal and the (*d*–π*) states in a net charge transfer in the opposite direction. This is the case of carbon monoxide adsorbed on transition metals.[19]

Some other and equally important features that have to be studied in order to understand the electronic properties of bimetallic interfaces are: i) the nature of the hetero-nuclear metal-metal bond and the occurrence of charge transfer at the interface; ii) the effect of these bonds on the physical and chemicals properties of metals; and iii) the effect of the reduced coordination numbers and the altered atomic structure (reconstruction and relaxations) on the surface and interface regions.[3,20]

Surprisingly, the occurrence of charge transfer is not often considered on bimetallic systems, despite of the fact that charge transfer should always be expected at the interface of metals with different workfunctions: if one aligns the electronic structure of two metals by the vacuum level, electrons have to flow from the metal with the lower workfunction to the one with the higher workfunction. The flow stops when a created interface dipole prevents further charge transfer, recovering the electronic equilibrium.[3] The *d*-band model discussed above is probably the main reason why charge transfer has been overlooked in the literature. After all, such a model assumes a constant filling of (and therefore no charge transfer to or from) the adlayer *d*-band. However, the charge transfer should be considered in bimetallic system, especially on those where the level of strain is negligible.

### 1.1.3 Metal–2D materials interfaces

The so-called 2D materials are crystalline structures consisting of a single layer of atoms. Such systems feature exceptional strength and electron mobility, providing a wide range of applications. The in-plane bonding in these materials can be covalent (as in graphene) or ionic (as in hexagonal boron nitride, *h*-BN). The vdW forces play a key role in the inter-layer interactions when 2D materials are stacked to form more bulk-like materials (from the same crystalline structure) or 2D heterostructures (from different crystalline structures).

Of course, a 2D material has to be supported in order to be used in practical situations. This condition can lead to an alteration of the peculiar properties of the material, not only in its geometry but also in its electronic structure. The first of these is best represented by the so-called Moiré patterns. When a metal surface (or another substrate) adsorbs an adlayer with a sufficiently different lattice constant and no reconstruction of the adlayer occurs, the mismatch results in the formation of structures with large unit. In addition to mismatch, the relative rotation between the adlayer and the substrate can trigger such superstructures. Either of these (or both) cause the formation of commensurate phases, areas where both structure lattices coincide and therefore strain is accumulated, favoring the vdW interactions. Conversely, incommensurate phases are unstrained (unsynchronized) areas where the elastic energy dominates.[21,22] The distribution of these phases over the interface is periodic, resulting in the formation of a Moiré pattern on the surface, i.e. a two-dimensional array of so-called *moirons*.[21] The balance between elastic energy and vdW energy determines the size of the lattice vectors of the superstructures: in large Moiré patterns, the vdW energies dominates whereas in small ones, the elastic energy. **Figure 1.2** illustrates a case where a long-range Moiré lattice is formed when graphene is adsorbed on Ru(0001), as reported in Ref. 23.

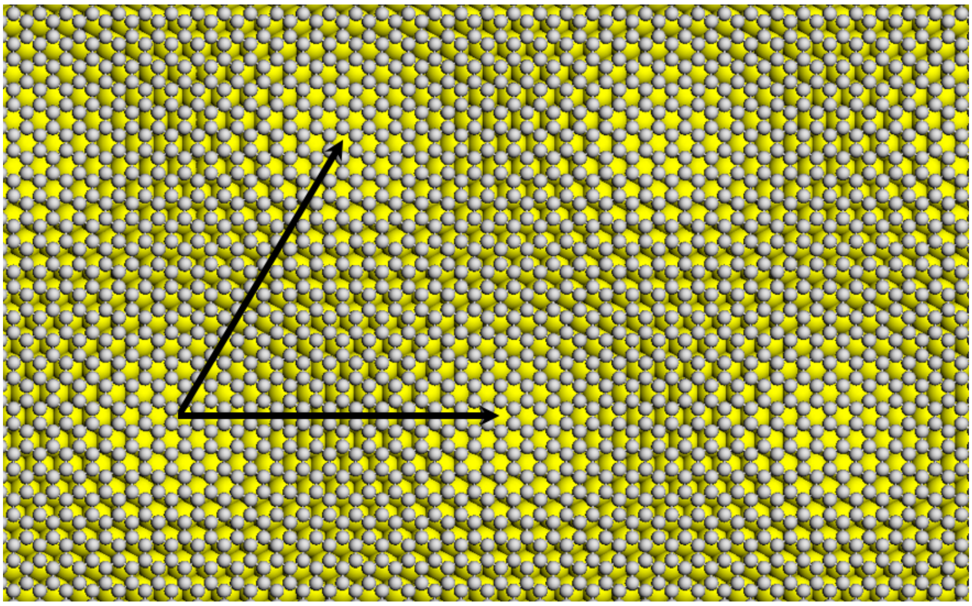

**Figure 1.2** Two-dimensional array of moirons between 25×25 unit cell of graphene and 23×23 unit cell of Ru(0001) surface. The arrows indicate the Moiré lattice vectors. Grey and yellow spheres correspond to C and Ru atoms, respectively.

Two-dimensional materials can exhibit a different electronic structure to their bulks when supported on metals. A monolayer of *h*-BN adsorbed on Ni(111) surface, for example, exhibits metallic behavior;[24] on the other hand, BN bulk poses a large bandgap of >5 eV.[25–27] Other transition metal substrates, including Rh(111) and Pt(111) surfaces, have been also reported to modify electronic properties of supported *h*-BN in a similar way.[28,29] It is not strange therefore that free-standing monolayers of *h*-BN, initially thought to be inert, can be engineered for catalytic oxidation processes[30] and spintronic applications.[31]

The metallic substrate could have, in principle, a non-negligible effect in the Raman spectrum, which is often used to "hunt" 2D structures.[25] So simulations that take into account vdW interactions should be used to resolve the induced-substrate effects in experimental measurements of adsorbed adlayers on metals or other substrates.[32]

## 1.2 THESIS OBJECTIVES

The overall aim of this thesis is to make a theoretical contribution to the understanding of the interaction of metal surfaces with other metals, molecules and 2D materials. Specific objectives of this theoretical work are as follows:

- To interpret and rationalize experimental data from X-ray photoelectron spectroscopy (XPS) and near-edge X-ray absorption fine structure (NEXAFS), to gain insight into the geometry of adsorption of methyl acetoacetate on Ni{111} and Ni{100} surfaces.

- To understand the geometry and electronic structure of the Pd/Re(0001) heteroepitaxial system, where interfacial strain is negligible and therefore direct support–adlayer interactions can be isolated, and contribute to the interpretation of XPS and low-energy electron diffraction (LEED)-IV measurements on this system.

- To determine the effect of the Ni{111} support on the Raman signature of monolayers of hexagonal boron nitride system, which exhibit an intrinsic upshift in the frequency of the $E_{2g}$ vibrational mode with respect to the bulk value.

## 1.3 REFERENCES

1 E. Kaxiras, *Atomic and Electronic Structure of Solids*, Cambridge University Press, New York, 2003.

2 C. Kittel, *Introduction to Solid State Physics*, John Wiley & Sons, New York, 1996.

3 H. Lüth, *Solid Surfaces, Interfaces and Thin Films*, Springer, Germany, Fifth Edit., 2010.

4 D. Wolf and S. Yip, Eds., *Materials Interfaces: Atomic-level Structure and Properties*, Springer Science & Business Media, First edit., 1992.

5 M. Mura, A. Gulans, T. Thonhauser and L. Kantorovich, *Phys. Chem. Chem. Phys.*, 2010, **12**, 4759–4767.

6 S. R. Logan, *Fundamentals of chemical kinetics*, Longman, 1996.

7 J. R. H. Ross, *Heterogeneous catalysis : fundamentals and applications*, Elsevier, 2012.

8 Y. Izumi, *Adv. Catal.*, 1983, **32**, 215–271.

9 Y. Nitta, *Chem. Lett.*, 1999, **28**, 635–636.

10 D. J. Watson, R. J. B. R. J. Jesudason, S. K. Beaumont, G. Kyriakou, J. W. Burton

and R. M. Lambert, *J. Am. Chem. Soc.*, 2009, **131**, 14584–14589.

11 A. Yaniv, *Phys. Rev. B*, 1978, **17**, 3904–3918.

12 B. Wu and N. Zheng, *Nano Today*, 2013, **8**, 168–197.

13 J. A. Rodriguez, R. A. Campbell and D. W. Goodman, *J. Phys. Chem.*, 1991, **95**, 2477–2483.

14 E. Kampshoff, E. Hahn and K. Kern, *Phys. Rev. Lett.*, 1994, **73**, 704–707.

15 R. Q. Hwang and M. C. Bartelt, *Chem. Rev.*, 1997, **97**, 1063–1082.

16 B. Hammer and J. K. Norskov, *Nature*, 1995, **376**, 238–240.

17 B. Hammer and J. K. Nørskov, *Theoretical Surface Science and Catalysis — Calculations and Concepts*, Elsevier, 2000, vol. 45.

18 J. K. Nørskov, T. Bligaard, J. Rossmeisl and C. H. Christensen, *Nat. Chem.*, 2009, **1**, 37–46.

19 C. D. Zeinalipour-Yazdi, A. L. Cooksy and A. M. Efstathiou, *Surf. Sci.*, 2008, **602**, 1858–1862.

20 R. Wu and A. Freeman, *Phys. Rev. B*, 1995, **52**, 12419–12425.

21 K. Hermann, *J. Phys. Condens. Matter*, 2012, **24**, 314210.

22 C. R. Woods, L. Britnell, A. Eckmann, R. S. Ma, J. C. Lu, H. M. Guo, X. Lin, G. L. Yu, Y. Cao, R. V. Gorbachev, A. V. Kretinin, J. Park, L. A. Ponomarenko, M. I. Katsnelson, Y. N. Gornostyrev, K. Watanabe, T. Taniguchi, C. Casiraghi, H.-J.

Gao, A. K. Geim and K. S. Novoselov, *Nat. Phys.*, 2014, **10**, 451–456.

23 D. Martoccia, P. R. Willmott, T. Brugger, M. Björck, S. Günther, C. M. Schlepütz, A. Cervellino, S. A. Pauli, B. D. Patterson, S. Marchini, J. Wintterlin, W. Moritz and T. Greber, *Phys. Rev. Lett.*, 2008, **101**, 126102.

24 E. Rokuta, Y. Hasegawa, K. Suzuki, Y. Gamou, C. Oshima and A. Nagashima, *Phys. Rev. Lett.*, 1997, **79**, 4609–4612.

25 R. V. Gorbachev, I. Riaz, R. R. Nair, R. Jalil, L. Britnell, B. D. Belle, E. W. Hill, K. S. Novoselov, K. Watanabe, T. Taniguchi, A. K. Geim and P. Blake, *Small*, 2011, **7**, 465–8.

26 S. N. Shirodkar, U. V. Waghmare, T. S. Fisher and R. Grau-Crespo, *Phys. Chem. Chem. Phys.*, 2015, **17**, 13547–13552.

27 F. A. Rasmussen, P. S. Schmidt, K. T. Winther and K. S. Thygesen, *Phys. Rev. B*, 2016, **94**, 155406.

28 A. B. Preobrajenski, A. S. Vinogradov and N. Mårtensson, *Surf. Sci.*, 2005, **582**, 21–30.

29 A. B. Preobrajenski, S. A. Krasnikov, A. S. Vinogradov, M. L. Ng, T. Käämbre, A. A. Cafolla and N. Mårtensson, *Phys. Rev. B*, 2008, **77**, 085421.

30 A. H. M. A. Wasey, S. Chakrabarty, G. P. Das and C. Majumder, *ACS Appl. Mater. Interfaces*, 2013, **5**, 10404–10408.

31 A. A. Tonkikh, E. N. Voloshina, P. Werner, H. Blumtritt, B. Senkovskiy, G. Güntherodt, S. S. P. Parkin and Y. S. Dedkov, *Sci. Rep.*, 2016, **6**, 23547.

32 Q. Cai, D. Scullion, A. Falin, K. Watanabe, T. Taniguchi, Y. Chen, E. J. G. Santos and L. Li, *Nanoscale*, 2017, **9**, 3059–3067.

# 2 Methodology

## 2.1 THE SCHRÖDINGER EQUATION

The fundamental goal in computational materials science is to describe the properties of a well-defined collection of atoms (i.e. nuclei plus electrons); for example, an isolated molecule or the atoms defining a crystal. One of the fundamental features to know about these atoms is the energy, and more importantly, how this energy changes as the atoms move around. The mathematical or graphical relationship between the energy of a collection of atoms and its spatial arrangement is called the potential energy surface (PES),[1] which is a central concept in computational material science that can be used to theoretically explore, for example, the lowest-energy spatial arrangement of a crystal.

Quantum Mechanics says that the wavefunction, ψ, contains all the nuclear and electronic information about a given system, and thus the basic equation to be solved is the time-independent Schrödinger equation:[2]

$$\hat{H}\psi = E\psi \tag{2.1}$$

In this equation, $\hat{H}$ is the Hamiltonian operator and $E$ is the energy (or eigenstates) of the system. The Hamiltonian operator includes the kinetic energy ($\hat{T}$) of electrons and nuclei and the potential energy of interaction ($V$) between the two types of particles:

$$\hat{H} = \hat{T}_{\mathrm{N}} + \hat{T}_{\mathrm{e}} + V_{\mathrm{NN}} + V_{\mathrm{Ne}} + V_{\mathrm{ee}} \tag{2.2}$$

The dynamics of interacting electrons and nuclei is very complex and consequently a practical implementation of **Equation 2.2** is not easy. The Born–Oppenheimmer approximation[3] facilitates such a task by allowing the decoupling of the nuclei and electronic motion rationalized by their great difference in mass. One consequence of this is that the Schrödinger equation can be solved by considering only the electronic part of the Hamiltonian:

$$\hat{H} = \hat{T}_{\mathrm{e}} + V_{\mathrm{Ne}} + V_{\mathrm{ee}} \tag{2.3}$$

with the nuclear coordinates ($\mathbf{R}_a$) as parameters. In atomic units:

$$H = -\sum_i \frac{1}{2}\nabla_i^2 - \sum_a \sum_i \frac{Z_a}{|\mathbf{R}_a - \mathbf{r}_i|} + \sum_i \sum_{j>i} \frac{1}{|\mathbf{r}_i - \mathbf{r}_j|} \tag{2.4}$$

The nucleus-nucleus interaction can be evaluated classically because nuclei are sufficiently heavy particles that display only small quantum effects. The electronic energy is obtained from the eigenvalues of the Hamiltonian above (the *electronic groundstate* being the lowest-energy solution for each configuration), and added to the nuclear energy to get the total internal energy. Once the internal energy is determined for a large number of nuclear geometries, the PES is known. We can then find the lowest-energy configuration, or *ionic groundstate*, for a given system.

Despite this simplification, the task is still complex because the electron wavefunction is a function of each of the spatial coordinates of each of the *N* electrons. Furthermore, the number of electrons in a particular system is considerably larger than the number of nuclei, simply because each atom has one nucleus and many electrons. For instance, the full wavefunction of a simple molecule like $CO_2$ is a 66-dimensional function (3 dimensions for each of the 22 electrons) even before considering spin. These two facts make the Schrödinger equation extremely challenging to solve. The situation looks even worse if one considers the third right-hand term in **Equation 2.4**. The form of this contribution means that the individual electron wavefunction cannot be found without simultaneously considering the individual electron wavefunctions associated with the rest of the electrons: the Schrödinger equation is a many-body problem.

It is worth understanding that the wavefunction of a particular set of electrons cannot be directly observed. The quantity of physical interest that in principle can be measured is the probability of locating those electrons at a particular set of coordinates. A closely related quantity is the density of electrons at a particular position in space, $\rho(\mathbf{r})$, which for a close-shell system, assuming independent electrons, is:

$$\rho(\mathbf{r}) = 2\sum_{i} \psi_i^*(\mathbf{r})\psi_i(\mathbf{r}) \tag{2.5}$$

Here, the summation goes over all the individual electron wavefunctions that are occupied by electrons, so the term inside the summation is the probability density for an electron in individual wavefunction $\psi_i(\mathbf{r})$ to be located around position $\mathbf{r}$. The electron density contains a great amount of information and is actually physically observable, and is the foundation of a whole theory in Computational Materials Science.

## 2.2 DENSITY FUNCTIONAL THEORY

The entire field of Density Functional Theory (DFT) rests on two fundamental mathematical theorems proved by Hohenberg and Kohn.[4] The first theorem is: *The groundstate energy from Schrödinger's equation is a unique functional of the electron density:*

$$E = E[\rho(\mathbf{r})] \tag{2.6}$$

From this theorem it is deduced that the groundstate electron density uniquely determines all properties, including the energy and wavefunction, of the groundstate. This result is important because it means that the Schrödinger equation can be solved by finding a function of three spatial variables, the electron density, rather than a function of $3N$ variables, the wavefunction.

The second Hohenberg–Kohn theorem defines an important property of the functional: *The electron density* $\rho_0(\mathbf{r})$ *that minimizes the energy of the overall functional is the true electron density corresponding to the full solution of the Schrödinger equation.* Any density different from the true density will lead to a higher energy:

$$E[\rho(\mathbf{r})] \geq E[\rho_0(\mathbf{r})] \tag{2.7}$$

This theorem suggest that it is possible to vary the electron density until the energy from the functional is minimized, giving a prescription for finding the relevant electron density.

A practical implementation of the Hohenberg–Kohn theorems is provided by the Kohn–Sham formalism,[5] which introduces *orbitals* in an effort to account for the poor representation of the kinetic energy of interacting electrons in *orbital-free* or *pure* DFT.[1] The Kohn–Sham approach employs non-interacting electrons as reference system, in which the groundstate electron density distribution is exactly the same as that in the real system.[6]

The electron energy in the Kohn–Sham formalism[5] can be expressed in terms of *Kohn-Sham orbitals* or one-electron spatial orbitals, $\psi_i^{\mathrm{KS}}(\mathbf{r})$:

$$\begin{aligned} E[\rho(\mathbf{r})] = -\frac{1}{2}\sum_i \int \psi_i^{\mathrm{KS}^*} \nabla^2 \psi_i^{\mathrm{KS}}\, \mathrm{d}\mathbf{r} + \int V(\mathbf{r})\rho(\mathbf{r})\mathrm{d}\mathbf{r} + \frac{1}{2}\iint \frac{\rho(\mathbf{r})\rho(\mathbf{r}')}{|\mathbf{r}-\mathbf{r}'|}\mathrm{d}\mathbf{r}\mathrm{d}\mathbf{r}' \\ + E_{\mathrm{xc}}[\rho(\mathbf{r})] \end{aligned} \tag{2.8}$$

The first three terms on the right are the electron kinetic energies, the Coulomb interactions between the electrons and the nuclei, and the Coulomb interactions between pairs of electrons. The fourth term, $E_{\mathrm{xc}}[\rho(\mathbf{r})]$, is the exchange-correlation functional which includes all the quantum mechanical effects that are not included in the known terms (a brief discussion of these effects is given further below).

The Kohn–Sham orbitals are found by solving the Kohn–Sham equations, which are derived by applying the variational principle to the electronic energy $E[\rho(\mathbf{r})]$ with the charge density given by **Equation 2.5**. The Kohn–Sham equations have the form:

$$\left[-\frac{1}{2}\nabla^2 + V(\mathbf{r}) + V_{\mathrm{H}}(\mathbf{r}) + V_{\mathrm{xc}}(\mathbf{r})\right]\psi_i^{\mathrm{KS}}(\mathbf{r}) = \varepsilon_i^{\mathrm{KS}}\psi_i^{\mathrm{KS}}(\mathbf{r}) \tag{2.9}$$

where $\varepsilon_i^{\mathrm{KS}}$ are the Kohn–Sham orbital energies. The exact groundstate electron density is then constructed via **Equation 2.5**. The solution of the Kohn–Sham equations are single-electron wavefunctions that depend on three spatial variables (ignoring spin). On the left-hand side of the Kohn–Sham equations there are three potentials: $V$, $V_{\mathrm{H}}$, and $V_{\mathrm{xc}}$. The first one defines the interaction between an electron and the collection of atomic nuclei. The second one is called the Hartree potential, $V_{\mathrm{H}}$, and is defined by:

$$V_{\mathrm{H}}(\mathbf{r}) = \int \frac{\rho(\mathbf{r}')}{|\mathbf{r} - \mathbf{r}'|}\mathrm{d}\mathbf{r}' \tag{2.10}$$

$V_{\mathrm{H}}$ describes the Coulomb repulsion between a single electron and the total electron density, which is defined by all electrons of the system. Part of $V_{\mathrm{H}}$ involves a Coulomb interaction between the electron and itself, because the electron is part of the total electron density. However, this self-interaction is unphysical and its correction has to be accounted into the final potential in the Kohn–Sham equations, $V_{\mathrm{xc}}$, which defines exchange and correlation contributions. Mathematically, $V_{\mathrm{xc}}$ can be defined as a functional derivative of the exchange-correlation energy, that is, $E_{\mathrm{xc}}[\rho(\mathbf{r})]$ is a functional $\rho(\mathbf{r})$ and the process of obtaining $V_{\mathrm{xc}}$ is a functional differentiation:[6]

$$V_{\mathrm{xc}}(\mathbf{r}) = \frac{\delta E_{\mathrm{xc}}[\rho(\mathbf{r})]}{\delta \rho(\mathbf{r})} \tag{2.11}$$

The term $E_{\mathrm{xc}}[\rho(\mathbf{r})]$ accounts for the *correlated* electron motion: i.e. for the fact that the multi-electron wavefunction cannot be obtained as a simple product of one-electron orbitals. Because of Pauli's exclusion principle, two electrons of the same spin have a greater separation distance than two of opposite spin, consequently their interaction energies are different. The energy reduction due to the larger spatial separation of electrons with the same spin is known as *exchange energy*, and can be calculated using an anti-symmetric all-electron wavefunction. This is the basis of the Hartree–Fock (HF) method,[a] where the all-electron wavefunction is written as a Slater determinant of the one-electron orbitals (the simplest anti-symmetric function). The correlation energy, on the other hand, is the part of the electron-electron interaction that cannot be described by the HF method. The combined contribution of exchange and correlation is a rather small fraction of the total energy. However, both effects are crucial in chemistry: covalent bonds result from exchange interactions, and dispersion forces result from correlation effects.

It is precisely these quantum mechanical effects that make extremely difficult the task of defining the exchange-correlation functional in **Equation 2.8**. And although its existence is guaranteed by the Hohenberg–Kohn theorem, it is simply *unknown*. Therefore, it is necessary to make use of approximations, which will be discussed next.

### 2.2.1 Jacob’s ladder of exchange–correlation functionals

The development of approximate forms for the functional for the exchange-correlation energy remains one of the most important areas of active research in the quantum

---

[a] The description of the Hartree–Fock method goes beyond the scope of the present chapter.

chemistry community. Numerous schemes have been developed that give good results in a large variety of physical problems. Reports of "failure" of DFT are in fact failures of approximations, not of the theory, which is exact in principle. Experience and intuition helps to decide which functional is "good" for a particular system.

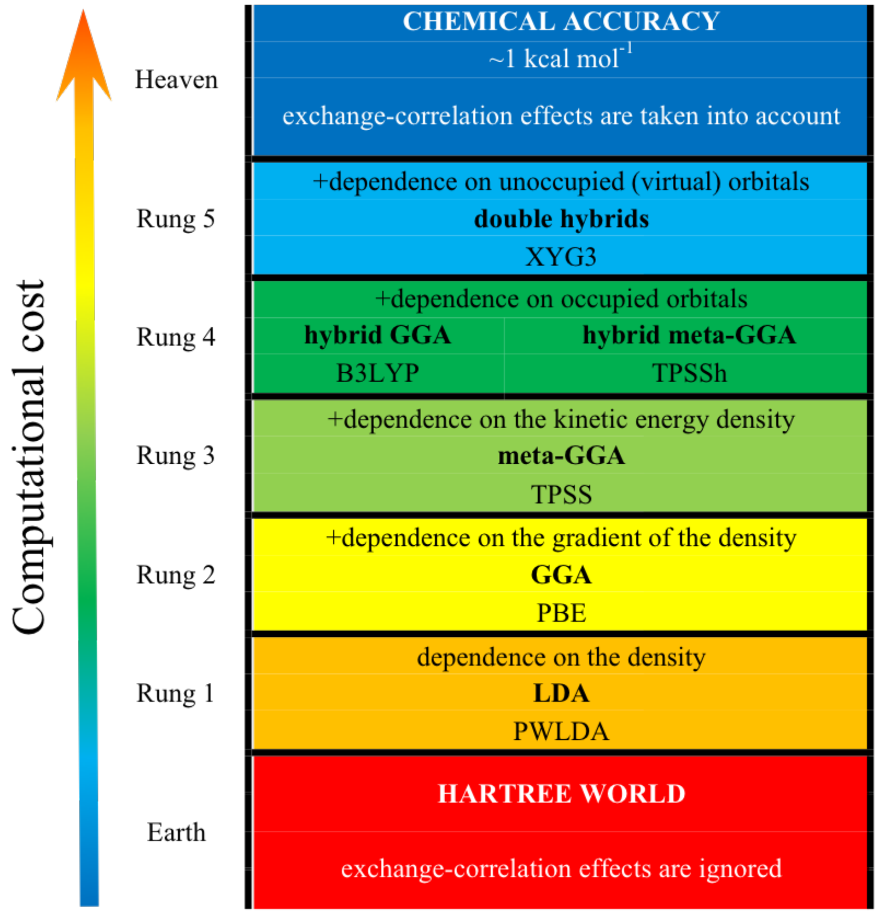

**Figure 2.1** Classification of the approximate exchange-correlation functionals according to Perdew's view of Jacob's ladder.[7,8]

Exchange-correlation functionals have mathematical forms containing parameters. There are two philosophies for assigning values to those parameters, either by requiring the functional to fulfil certain theoretical criteria (for example, minimizing electron self-interaction, exhibiting a certain asymptotic behavior of the exchange and correlation potentials, etc.) or by fitting the parameters to experimental data.[1] Either way, the quality of the functionals will have to be settled by comparing the performance with experiments or at least with high-level quantum-mechanical calculations. Such calibration only evaluates the quality for the chosen selection of systems and properties; some functionals being good for molecular systems, other for delocalized (periodic) systems and other for properties such as excitation energies.

Still, it is possible to establish a rough ranking of functionals based on their general accuracy. A popular illustration of the hierarchy of functionals is that of Jacob's ladder[7,8] connecting the "Earth to Heaven" (**Figure 2.1**). There are five rungs in this ladder, rising from "Hartree world", where the exchange-correlation effects are completely ignored, towards the "chemical accuracy", where the exchange-correlation effects are adequately taken into account. Each rung should recover the results of lower steps in the appropriate limits, but add more capabilities. This ladder brings DFT closer to the *heaven of chemical accuracy*, ~1 kcal $\text{mol}^{-1}$ or less for some representative energy properties like heats of formation, bond dissociation energies, reaction barriers heights and non-bonded interaction energies. We now discuss the basic features of each level of approximation.

#### 2.2.1.1 First rung: Local Density Approximation

In the Local Density Approximation (LDA) it is assumed that the exchange-correlation energy per particle at a given point of space is just a function of the electron density at that point. That function is taken to be exactly the same as the exchange-correlation energy per particle in a homogeneous electron gas of the given density, $\varepsilon_{\text{xc}}^{\text{hom}}(\rho)$, which is known to high accuracy. Note that the LDA does not assume that the electron density in a system, a molecule for instance, is homogeneous (uniform), the spatial variation of the density is recognized, as shown in the equation:

$$E_{\mathrm{xc}}^{\mathrm{LDA}}[\rho(\mathbf{r})] = \int \rho(\mathbf{r})\varepsilon_{\mathrm{xc}}^{\mathrm{hom}}(\rho(\mathbf{r}))\mathrm{d}\mathbf{r} \tag{2.12}$$

It is customary to separate $E_{\mathrm{xc}}[\rho(\mathbf{r})]$ into two parts, a pure exchange $E_{\mathrm{x}}[\rho(\mathbf{r})]$ and a correlation part $E_{\mathrm{c}}[\rho(\mathbf{r})]$:

$$E_{\mathrm{xc}}[\rho(\mathbf{r})] = E_{\mathrm{x}}[\rho(\mathbf{r})] + E_{\mathrm{c}}[\rho(\mathbf{r})] \tag{2.13}$$

The exchange part $E_{\mathrm{x}}[\rho(r)]$ can be expressed analytically by the Dirac Formula:[1]

$$E_{\mathrm{x}}^{\mathrm{LDA}}[\rho(\mathbf{r})] = -\frac{3}{4}\left(\frac{3}{\pi}\right)\int \rho^{4/3}(\mathbf{r})\mathrm{d}\mathbf{r} \tag{2.14}$$

The analytical form for the correlation form of uniform electron gas has been derived in the high and low density limits.[9] For intermediate densities, the correlation energy has been determined to a high precision by quantum Monte Carlo methods. In order to use these results in DFT calculations, it is necessary to have a suitable analytic interpolation formula, and such a formula has been constructed by *Vosko*, *Wilk* and *Nusair* (VWN)[10] and by *Perdew* and *Wang* (PW),[11] and are considered to be accurate fits.

The corresponding spin-dependent version of LDA is called Local Spin-Density Approximation (LSDA) which can handle systems with one or more unpaired electrons, like radicals. For species in which all the electrons are spin-paired, LSDA is equal to LDA and, since this is the most common case, LDA is often used interchangeably with LSDA.

Despite the simplicity in the fundamental assumption that exchange-functional and correlation functional depend only on $\rho(\mathbf{r})$, LDA has been successful at describing extended systems, such as metals, where the approximation of a slowly varying electron density is quite valid. However, the accuracy decreases when there is a rapid variation of the electron density in the system, like in the case of molecules. For example, LDA leads to low excitation energies in both molecules and solids,[12] and often overestimates activation barriers in chemical reactions.[13]

#### 2.2.1.2 Second rung: Generalized Gradient Approximation

Improvements over LDA must consider the inhomogeneity of the electron density. A step in this direction is to make the exchange-correlation energy depend also on derivatives of the electron density. In the Generalized Gradient Approximation (GGA) methods, both the electron density $\rho(\mathbf{r})$ and the first derivative (gradient) of $\rho(\mathbf{r})$ with respect to position are included as variables for the exchange-correlation energy per particle:

$$E_{\mathrm{xc}}^{\mathrm{GGA}}[\rho(\mathbf{r})] = \int \rho(\mathbf{r})\varepsilon_{\mathrm{xc}}\left(\rho(\mathbf{r}), \nabla\rho(\mathbf{r})\right)\mathrm{d}\mathbf{r} \tag{2.15}$$

There are many ways in which information from the gradient of the electron density can be included in a GGA functional, so there are a considerable number of distinct GGA functionals. Two of the most widely used functionals are the Perdew–Wang functional (PW91)[14] and the Perdew–Burke–Ernzerhof functional (PBE).[15] PW91 is a first-principles numerical functional constructed from the second-order density-gradient expansion for the exchange-correlation hole[b] surrounding the electron in a system of slowly varying density, then cutting off the spurious *non-local* parts to satisfy sum rules on the exact hole (other exact condition that a functional should meet). The PBE functional, probably the best on average for all properties,[16] is a simplified version of PW91. PBE improves six shortcomings over PW91, including a simple mathematical form for both the enhancement factor in the exchange functional, and for the gradient contribution in the correlation functional. Such expressions contain the parameters $\kappa$ and $\mu$ for the exchange

---

[b] Defined as the region around an electron with reduced probability of finding another electron; it is a direct consequence of exchange-correlation effects. In DFT literature, it is common to discuss the exchange-correlation features in terms of probability *holes*.

enhancement factor, and $\alpha$ and $\beta$ for the gradient contribution in the correlation. The refinements were considered to satisfy those conditions that are energetically significant, in contrast to PW91 that was designed to satisfy as many exact conditions as possible. Despite the sacrifices made in the simpler PBE functional, results obtained using this method are essentially the same results as those obtained using PW91.

Note that the aforementioned parameters in PBE are fundamental constants; however, there remains flexibility in the choice of values,[15] allowing the PBE functional to be slightly modified to improve its performance. For example, the revised version of Zhang and Yang adopts a different value for $\kappa$, improving significantly the reference atomic energies and molecule atomization energies. This revised version of PBE is labeled as revPBE.[17] In a similar way, the modified PBE version for solids and surfaces, PBEsol,[18] employs other values for the parameters $\beta$ and $\mu$.

There are significant improvements thanks to the inclusion of $\nabla\rho(\mathbf{r})$ as an additional variable. Usually GGA gives better results than LDA, particularly in atomization energies of molecules and energy barriers of chemical reactions. Also, there is improved description of relative stability of bulk phases. On the other hand, it is well-known the overestimation of the lattice parameters in metals by GGA,[19] and excitation energies are still underestimated,[20] as in the LDA.[12] Hence, further improvements should be made.

#### 2.2.1.3 Third rung: Meta-GGA methods

The next extension of GGA approach is to allow the exchange-correlation energy per particle to depend also on the second derivative of $\rho(\mathbf{r})$ with respect to position. Such higher order derivative is the Laplacian of the electron density, $\nabla^2\rho(\mathbf{r})$. Alternatively, the functionals can be taken to depend on the orbital kinetic energy density $\tau(\mathbf{r})$, defined as the sum of the squares of the gradients of the KS orbitals:[6]

$$\tau(\mathbf{r}) = \frac{1}{2} \sum_{i=1}^{\text{occupied}} \left|\nabla\psi_i^{\text{KS}}(\mathbf{r})\right|^2 \tag{2.16}$$

$\tau(\mathbf{r})$ and $\nabla^2\rho(\mathbf{r})$ carry the same information, since they are related via the orbitals and the effective potential (i.e. all potential terms in the KS equations).[1] In practice, calculation of the former is numerically more stable than calculation of the latter.[1,6] Functionals that include either of them as a third variable are called meta-GGA functionals.

The TPSS (Tao-Perdew-Staroverov-Scuseria) functional,[21] which is probably the best known within the meta-GGA family, does not contain empirical parameters and can be considered as the next improvement over the PBE functional.

#### 2.2.1.4 Fourth rung: Hybrid and Hyper-GGA methods

In this rung, the information of the occupied KS orbitals is employed. Such information is contained in the exact exchange energy calculated through the HF method. The hybridization of both methods lies in the Adiabatic Connection Formula (ACF),[22] which allows to take the $E_{\text{xc}}[\rho(\mathbf{r})]$ as a weighted sum of DFT exchange-correlation energy and HF exchange energy. *Hybrid* DFT functionals compute the HF-type electron exchange from the KS wavefunction of the non-interacting electrons, thanks to the formalism of ACF that “turns on” the electron-electron interaction.[1]

A simple expression of this idea is:

$$E_{\text{xc}} = a_{\text{x}}E_{\text{x}}^{\text{HF}} + (1 - a_{\text{x}})E_{\text{x}}^{\text{GGA}} + E_{\text{c}}^{\text{GGA}} \tag{2.17}$$

In the hybrid-GGA family, the base is a GGA functional and the coefficient $a_{\mathrm{x}}$ gives the percentage of HF exchange energy incorporated into it. The most popular and successful hybrid method is B3LYP[23,24] which has a total of eight purely empirical parameters and includes 20% of HF exchange. The PBE functional has also been improved by addition of 25% of exact exchange to give the PBE0 functional.[25]

If the base is one of the third-rung, the hybrid functional falls into the *hyper-GGA* family. TPSS functional, for example, has been augmented with 10% of exact exchange to give the TPSSh method.[26,27]

#### 2.2.1.5 Fifth rung: Double-hybrid methods

At the fifth level of the Jacob's ladder classification, the full information of the KS orbitals should be employed, i.e. not only the occupied but also the virtual (unoccupied) orbitals are included, by introducing a hybrid calculation of both exchange and correlation (thus *double hybrid*). Inclusion of the virtual orbitals is expected to significantly improve, for example, dispersion interactions, which is a significant problem for almost all current functionals.

Following the idea of the previous rung, the information of the unoccupied Kohn–Sham orbitals is embedded in the second-order perturbative correlation energy,[28] which can be obtained via wavefunctions methods; for example, second-order Møller–Plesset perturbation theory (MP2)[6] or second-order Görling–Levy coupling-constant perturbation therory (PT2).[29] The XYG3 functional[30] incorporates this information from the latter. In a similar fashion than the previous rung, the percentage of correlation is given by a constant:

$$E_{\mathrm{xc}} = a_{\mathrm{x}} E_{\mathrm{x}}^{\mathrm{HF}} + (1 - a_{\mathrm{x}}) E_{\mathrm{x}}^{\mathrm{GGA}} + b E_{\mathrm{c}}^{\mathrm{GGA}} + c E_{\mathrm{c}}^{\mathrm{PT2}} \tag{2.18}$$

The B2-PLYP contains, for example, 53% of HF exact exchange and 27% of perturbative second-order correlation.[31]

## 2.2.2 Functionals overview

Perdew *et al.*[8] said the "divine functional" must be fully non-local. Kurth *et al.*[12] use *local*, *semi-local*, and *non-local* to refer to properties that are determined at a point, at an infinitesimal distance beyond the point, and at a finite distance beyond the point, respectively. Based on these definitions, local (LDA) and semi-local (GGA) functionals are common ways to term DFT methods. *Fully* non-local functionals, with all relevant properties treated non-locally, are apparently not yet available for practical calculations.[31] Exact electron exchange energy is an example of a non-local property of $\rho(\mathbf{r})$, because it arises from "Pauli repulsion" between electrons a finite distance apart.

Dispersion interactions, or van der Waals (vdW) interactions, are effects arising from non-local correlation. Standard DFT functionals do not account for vdW interactions because they are "short-sighted" at considering correlation. Many DFT-based dispersion methods, however, have been developed to overcome this issue. The basic requirement for any of those approaches is to yield reasonable $-1/R^6$ asymptotic behavior for the interaction of particles in the gas phase.

The simplest way to achieve such a behavior is to include an additional energy term in the computed total energy, $E_{\text{total}}$, that accounts for the missing long-range attraction:

$$E_{\text{total}} = E_{\text{DFT}} + E_{\text{disp}} \tag{2.19}$$

where $E_{\text{DFT}}$ is the DFT total energy calculated with a given exchange-correlation functional, and $E_{\text{disp}}$ denotes the dispersion interaction, which is expressed as:

$$E_{\text{disp}} = -\sum_{\text{A,B}} \frac{C_6^{\text{AB}}}{R_{\text{AB}}^6} \tag{2.20}$$

The term $C_6^{\text{AB}}$ is the dispersion coefficient that depends on the elemental pairs A and B; $R_{\text{AB}}$ is the distance between the two nuclei. This approach is pair-wise additive and can therefore be calculated as a sum over all pairs of atoms A and B. The coefficients are tabulated empirically (from experimental ionization potentials and polarizabilities) and they must be isotropic (direction independent) and constant.[32] Techniques that use **Equation 2.20** are termed as DFT-D methods.

The $C_6/R^6$ function acts very strongly within typical bonding distances, where the quantum-mechanical description is more accurate, so at short distance the empirical contribution must be removed. To "damp" the dispersion correction at short values of $R$, a damping function must be used:

$$E_{\text{disp}} = -\sum_{\text{A,B}} \frac{C_6^{\text{AB}}}{R_{\text{AB}}^6} f_{\text{AB}}(R_{\text{AB}}) \tag{2.21}$$

where $f(R)$ is equal to one for larger $R$ and decreases to zero or to a constant for small values of $R$.

In the so-called DFT-D2 proposed by Grimme[33] the damping function is sensitive to the definition of atomic size (referred to as vdW radii) and must be chosen carefully. The dispersion energy is also sensitive to a "global scaling factor" which adjusts the correction to the repulsive behavior of the chosen exchange-correlation functional used to get the DFT total energy. Grimme also proposed one scheme to calculate the $C_6$ coefficients from a formula which couples ionization potentials and static polarizabilities of isolated atoms. Such coefficients, as well as the atomic vdW radii, are available for all elements up to Xe.[33]

A drawback of the D2 method is that the dispersion coefficients are kept constant during the calculation, therefore, the effect of different chemical states of the atom or of its environment are neglected. The DFT-D3 of Grimme *et al.*[34] captures the environmental dependence of $C_6$ coefficients by considering the number of neighbors each atom has. When an atom has more neighbors, the $C_6$ coefficient decreases because the atom is "squeezed" and its electron cloud becomes less polarizable. The damping function was also reworked within this method. The DFT-D3 with "zero-damping"[34] has two fitted parameters whereas the DFT-D3 with Becke and Johnson (BJ)-damping has three.[35]

The methods discussed so far require predetermined input parameters to calculate the dispersion interaction. There are methods that do not rely on external input parameters but rather obtain the dispersion interaction directly from the electron density. They are termed non-local correlation functionals, since they add non-local correlations to local or semi-local correlation functionals.

Dion *et al.* in 2004[36] proposed the first non-local correlation functional which calculates the exchange-correlation energy $E_{\mathrm{xc}}[\rho(\mathbf{r})]$ as:

$$E_{\mathrm{xc}}[\rho(\mathbf{r})] = E_{\mathrm{x}}^{\mathrm{GGA}}[\rho(\mathbf{r})] + E_{\mathrm{lc}}^{\mathrm{LDA}}[\rho(\mathbf{r})] + E_{\mathrm{nlc}}[\rho(\mathbf{r})] \qquad (2.22)$$

where $E_{\mathrm{x}}^{\mathrm{GGA}}[\rho(\mathbf{r})]$ is the exchange energy in the revPBE approximation,[17] $E_{\mathrm{lc}}^{\mathrm{LDA}}[\rho(\mathbf{r})]$ denotes the LDA correlation and $E_{\mathrm{nlc}}[\rho(\mathbf{r})]$ corresponds to the non-local correlation energy term that accounts approximately for the non-local electron correlation effects. This method has been called the van der Waals density functional (vdW-DF). Note that vdW-DF removes the GGA correlation and incorporates it as the sum of two components: the local and non-local correlation. The local part is obtained within LDA, whereas the non-local correlation part is obtained using an expression like this:

$$E_{\mathrm{nlc}}[\rho(\mathbf{r})] = \iint \mathrm{d}\mathbf{r}\,\mathrm{d}\mathbf{r}'\rho(\mathbf{r})\varphi(\mathbf{r},\mathbf{r}')\rho(\mathbf{r}') \tag{2.23}$$

This is a double space integral where $\varphi(\mathbf{r},\mathbf{r}')$ is the vdW kernel, which is analogous to the classical Coulomb interaction kernel $1/|\mathbf{r}-\mathbf{r}'|$ but the vdW kernel has $1/|\mathbf{r}-\mathbf{r}'|^6$ asymptotic behavior. The vdW kernel can be tabulated in advance in terms of "two dimensionless variables".[37]

Since the development of the original vdW-DF, there is still ongoing work to improve the performance of the method. The original flavor for the exchange part of vdW-DF method often leads to too large intermolecular binding distances and inaccurate binding energies.[38] Fortunately, **Equation 2.22** leaves open the possibility to choose alternative exchange functionals. Hence, "less repulsive" exchange functionals have been proposed. Of these, the "opt" series (optB88, optB86b and optPBE)[38,39] have been incorporated within the vdW-DF scheme, leading to much improved accuracy.

### 2.2.3 Iterative procedure to solve the KS equations

An important aspect to discuss is the procedure for solving the KS equations. To do so, it is required to define the Hartree potential $V_{\mathrm{H}}(\mathbf{r})$, and to define it, the electron density $\rho(\mathbf{r})$ must be known. However, finding the electron density $\rho(\mathbf{r})$ requires knowing the KS orbitals $\psi_i^{\mathrm{KS}}(\mathbf{r})$, and to know these orbitals, it is required to solve the KS equations. To break this circle, the problem is usually addressed in an iterative way as outlined in the following algorithm:

1. Construct the external potential, defined by atomic numbers and the ionic position.

2. Define a trial (initial) $\rho(\mathbf{r})$.

3. Calculate $V_H(\mathbf{r})$ and the exchange-correlation potential $V_{xc}(\mathbf{r})$.

4. Solve the KS equations (**Equation 2.9**).

5. Calculate $\rho(\mathbf{r})$ defined by the $\psi_i^{KS}(\mathbf{r})$ (**Equation 2.5**).

6. Compare the calculated $\rho(\mathbf{r})$ with the trial (initial) $\rho(\mathbf{r})$ used to solve the KS equations:

    a. If the two densities are the same, then this is the groundstate $\rho(\mathbf{r})$, and it can be used to compute the total energy (**Equation 2.8**).

    b. If the two densities are different, then the trial (initial) $\rho(\mathbf{r})$ must be updated in some way, and the process begins again from step 2.

Depending on the implementation, the convergence test of step 6 can be done also in terms of the total energy, or the eigenvalues, or a combination of both.

## 2.3 Convergence in DFT calculations

The DFT groundstate energy of a given system is defined by a complex set of mathematical equations, as it was seen in the previous section. To solve such equations computationally, one has to make use of a series of numerical approximations, such as truncation of infinite sums to finite sums, and evaluation of the multidimensional-space function over a finite collection of points. Such approximations facilitate the task of finding numerically a solution of the DFT equations with a specific exchange-correlation functional. Of course, such a solution has to be "well-converged" that is, a solution that accurately approximates the exact solution of the mathematical problem posed by DFT. In this section, we briefly focus on what is required to perform well-converged

DFT calculations with particular emphasis on the relationship between physical concepts in solids and numerical convergence.

### 2.3.1 Reciprocal space and planewaves

In computational material science, we are interested in applying DFT calculations to solids that are periodic in space. The periodicity in solids allow us to do some simplifications to describe their properties, considering only a small portion of the solid: the *unit cell*, which reproduces the macroscopic solid by applying translational operators. This singular property facilitates the study of periodic solids by just considering the unit cell to solve the Schrödinger equation. The only condition is that the solution must satisfy a fundamental property known as Bloch's theorem,[1] which states that the solution of the Schrödinger equation (or KS equations) can be expressed as the product of two functions:

$$\psi_i(\mathbf{r}) = e^{i\mathbf{k}\cdot\mathbf{r}} f_i(\mathbf{r}) \tag{2.24}$$

where the term $e^{i\mathbf{k}\cdot\mathbf{r}}$ represents a set of functions called *planewaves*,[c] and $f_i(\mathbf{r})$ is a periodic function with the same periodicity as that of the solid.

The space defined in $e^{i\mathbf{k}\cdot\mathbf{r}}$ by vectors $\mathbf{r}$ is called *real space* whereas the space of vectors $\mathbf{k}$ is called *reciprocal space* (or $\mathbf{k}$ space). In real space, we defined the atomic positions in terms of the lattice vectors $\mathbf{a}_1$, $\mathbf{a}_2$, and $\mathbf{a}_3$, and the corresponding three vectors that define positions in the reciprocal space are called reciprocal lattice vectors $\mathbf{b}_1$, $\mathbf{b}_2$, and $\mathbf{b}_3$, which are defined as:

$$\mathbf{b}_1 = 2\pi\frac{\mathbf{a}_2\times\mathbf{a}_3}{\mathbf{a}_1\cdot(\mathbf{a}_2\times\mathbf{a}_3)}, \qquad \mathbf{b}_2 = 2\pi\frac{\mathbf{a}_3\times\mathbf{a}_1}{\mathbf{a}_2\cdot(\mathbf{a}_3\times\mathbf{a}_1)}, \qquad \mathbf{b}_3 = 2\pi\frac{\mathbf{a}_1\times\mathbf{a}_2}{\mathbf{a}_3\cdot(\mathbf{a}_1\times\mathbf{a}_2)} \tag{2.25}$$

---

[c] Calculations based on this idea are referred to as planewave calculations.

Similar to the definition of the unit cell in real space, these three vectors define a unit cell in reciprocal space called the *Brillouin zone* (often abbreviated to BZ in the literature). The Brillouin zone plays a central role in the physical description of solids.[40] Furthermore, many parts of the mathematical equations in DFT applied to periodic solids are more convenient to solve in this cell (in terms of **k**) rather than in the direct unit cell (in terms of **r**).[41]

The second term in **Equation 2.24**, $f_i(\mathbf{r})$, can be expanded in terms of a Fourier series since it is a periodic function:

$$f_i(\mathbf{r}) = \sum_{\mathbf{G}} c_{j,\mathbf{G}} e^{i\mathbf{G}\cdot\mathbf{r}} \tag{2.26}$$

where **G** represents reciprocal lattice vectors defined by $\mathbf{G} \cdot \mathbf{r} = 2\pi m$ with integers values for $m$, and $c_{j,\mathbf{G}}$ are planewave expansion coefficients.

By combining **Equation 2.24** and **Equation 2.26**, the electron wavefunctions can be written as a linear combination of planewaves:

$$\psi_i(\mathbf{r}) = \sum_{\mathbf{G}} c_{j,\mathbf{k}+\mathbf{G}} e^{i(\mathbf{k}+\mathbf{G})\cdot\mathbf{r}} \tag{2.27}$$

Each planewave in **Equation 2.27** is characterized by a specific kinetic energy with the following mathematical form:

$$E = \frac{1}{2}|\mathbf{k} + \mathbf{G}|^2 \tag{2.28}$$

At first glance, the evaluation of the integrals in **Equation 2.27** seems to be a formidable task since **k** needs to be sampled with infinity density and **G** has infinite range. Fortunately, one can do two important approximations in order to evaluate the integrals in the Brillouin zone.

First, integrals in **k** space can be approximately evaluated using a set of discrete **k** *points*, where each **k** point can be taken as representative of a small region of **k** space. The process of choosing the **k** points to evaluate the integrals is known as “sampling the Brillouin zone”. The Monkhorst-Pack method[42] is the most widely used approach to sample the Brillouin zone; within this method, we just need to specify a grid density of $M\times M\times M$ **k** points (where $M$ is the number of **k** points in each direction in reciprocal space). Other interesting feature we can use to sample the Brillouin zone is the inverse relation between the unit cell and the corresponding reciprocal unit cell (**Equation 2.25**). Large (small) unit cells require relatively a few (large) number of **k** points to evaluate integrals in **k** space because large (small) volume in real space correspond to small (large) volume in reciprocal space.

The second assumption has to do with the “cutoff energy”. In **Equation 2.28**, it is reasonable to expect that planewaves with lower kinetic energies are more physically important than those with higher energies in the description of valence states. As a result, we can truncate the planewave basis set to include only planewaves with kinetic energy less than some particular cutoff energy:

$$E_{\text{cut}} = \frac{1}{2}\mathbf{G}_{\text{cut}}^2 \tag{2.29}$$

Therefore, the infinite sum in **Equation 2.27** is truncated to:

$$\psi_i(\mathbf{r}) = \sum_{|\mathbf{G}+\mathbf{k}|<\mathbf{G}_{\text{cut}}} c_{j,\mathbf{k}+\mathbf{G}} e^{i(\mathbf{k}+\mathbf{G})\cdot\mathbf{r}} \tag{2.27}$$

Of course, the truncation of the planewave basis set at a finite cutoff energy, $E_{\text{cut}}$, will lead to an error in the computed total energy and its derivatives. It is possible to reduce the magnitude of the error in a systematic way by increasing the value of $E_{\text{cut}}$ until the calculated total energy converges within a required tolerance. These arguments are also valid for the convergence testing of Brillouin zone sampling. It is good practice, therefore, to report both the cutoff energy and the $\mathbf{k}$ points used in the DFT calculations for reproducibility purposes.

### 2.3.2 Pseudopotentials: Projector Augmented Wave method

From a physical point of view, the chemical bonding and other physical properties of materials are defined mostly by the *valence electrons* in atoms. The tightly bound *core electrons* are not especially important in defining such characteristics, and their description requires planewaves with very high kinetic energies. Therefore, we can greatly reduce both the number of electrons and the number of planewaves necessary in a DFT calculation by calculating only the valence electrons. The effective potentials experienced by the valence electrons from the interaction with the *core* (the nucleus plus core electrons) are called *pseudopotentials*.[41] In some cases, pseudopotentials are not employed and instead the core electrons states are considered just fixed to a reference (atomic) state; this is the *frozen-core* approach. Calculations that do not include pseudopotentials or a frozen core approximation, i.e. where the core electrons are relaxed, are called *all-electron* calculations.

Conventionally, a pseudopotential is developed by considering a fixed electronic configuration of an isolated atom (or ion) such that the pseudopotential reproduces the scattering properties of a nucleus in that particular configuration. The resulting pseudopotential can be used then reliably in calculations for any other chemical environment of the atom without further adjustment of the pseudopotential. This desirable feature is referred to as *transferability* of the pseudopotential. Other equal important feature is the degree of *hardness* of the pseudopotential.[41] The pseudopotential is constructed with pseudo wavefunctions that have no nodes within the core region, but the pseudo wavefunctions and pseudopotential agree with the true wavefunction and potential outside some cut-off radius. A small cut-off radius defines a "hard" pseudopotential whereas a "soft" pseudopotential is defined by a large cut-off radius.[1] The former requires more planewave basis functions for describing the region beyond the core region than the latter. There are different ways to define a pseudopotential. The two most common forms include the norm-conserving[43] and ultrasoft[44] pseudopotentials.

The projector augmented wave (PAW) method[45] is a frozen-core approximation which is widely used nowadays in the planewave-DFT community. In the PAW method, the wavefunction is written as a valence term expanded in a planewave basis set plus a contribution from the region within the cut-off radius. The core contribution is calculated as the difference between two sets of grid densities, one coming from the atomic orbitals, the other from a set of nodeless pseudo-atomic orbitals. This allows to describe the behavior of the core region at different environments. The evaluation of the atomic orbitals requires an all-electron calculation, although the atomic orbitals are kept fixed at their form for the isolated atom. The success of the PAW method is due to its low computational cost. Furthermore, it incorporates a proper description of the core region (even if this is done using the frozen-core approach). Virtually it resembles the features of an all-electron calculation.

## 2.4 Slab model

A solid surface can be seen as a slice of material that is infinite in two dimensions, but finite along the surface normal. The so-called *slab* model takes advantage of periodic boundary conditions in two dimensions, and for the third dimension it makes use of a concept called *vacuum space*. The basic idea is illustrated in **Figure 2.2a**. The model contains atoms filling the entire space in the **x** and **y** directions, whereas along the **z** direction only a fraction of the space is occupied by atoms. The empty space left above the atoms in the top portion of the model is the vacuum space, which separates periodic images of the slab. When this *supercell* (atomic layers plus vacuum space) is repeated in all three dimensions, it defines a series of stacked slabs of a solid material separated by empty spaces, as shown in **Figure 2.2b**.

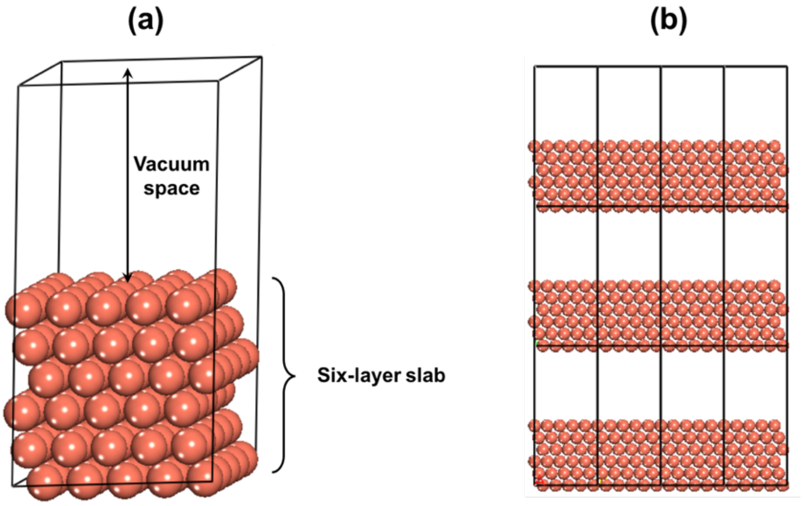

**Figure 2.2** (a) Schematic representation of a solid surface within the slab model. (b) View of the material showing replicas of the supercell with periodic boundary conditions in all three directions.

It is important when using the slab model to consider three important aspects. The first of those has to do with the *size of the vacuum space*. This must be large enough to avoid interaction between neighboring slabs. But a larger vacuum space increases the required computational resources. In practice, we can determine how much vacuum is “enough” by performing a total energy convergence test with respect to the width of the vacuum region– typically ~10 Å it is enough. Ideally, a proper size of vacuum space will make the electron density tails off to zero a short distance from the edge of the slab. This means that accurate results can be achieved by using just one **k** point in the **z** direction. As a result, it is a common practice in slab calculations to use a $M \times N \times 1$ mesh, where $M$ and $N$ have to be adequately chosen to sample the **k** space in the plane of interest.

A second aspect to consider in slab calculations the slab is *thickness*, i.e. the number of atomic layers that compose the slab representing the surface of interest. Of course, the thickness of material below a real surface is much larger than what one can afford in slab simulations. Normally, more layers are better, but using more layers also inevitably needs more computational effort. The thickness that is deemed sufficient in a slab calculation depends on the property of interest; for example, the surface energy. Once again, we have to converge the property of interest with thickness.

The final aspect to take into account in the slab model is *relaxation*. Typically, we allow to relax some of the top layers and keep the remaining bottom layers fixed at optimized bulk positions. This convention defines an *asymmetric* slab; layers on one side of the supercell are relaxed to mimic the surface and layers on the other side are kept fixed to mimic the bulk region of the material. However, an asymmetric slab model generates a dipole, which arises from the electrostatic interaction of the relaxed surfaces with the unrelaxed surfaces of other images. This is even more problematic if we wish to study the adsorption of atoms or molecules on a surface, because the dipole created by adsorption could be sizable. Although this electrostatic interaction is mathematically correct in system with periodic boundary conditions, it is physically spurious.[41] Many DFT codes implement a scheme for canceling this artificial electrostatic field such as the method proposed by Makov and Payne.[46] An alternative for avoiding this spurious dipole effect is to describe the surface using a *symmetric* model. In the symmetric model, the atoms in the middle layers are fixed at bulk geometries and the layers above and below are allowed to relax. The advantage of a symmetric model is that any dipole generated by relaxation will be automatically canceled. The drawback is the cost involved, because it is typically necessary to include more layers in a symmetric slab than in an asymmetric slab.

## 2.5 Core-level binding energy shifts within DFT

Finally, we describe how the core-level binding energy shifts, $\Delta \mathrm{BE}_{\mathrm{CL}}$, in Chapter 3 and 4 were calculated. Comparison of DFT results with experimental data is a desirable step either to validate simulations or to interpret experiments.

In the present investigation and in order to compare to XPS data, we calculated the core-level of atoms of interest in the so-called final-state approximation,[47] i.e. they were computed as total energy differences between two separate calculations.[48] The first one is a standard DFT calculation performed on the fully relaxed system. In the second calculation, one electron from the chosen core level of a specific atom is excited to the lowest conduction band state, allowing only the valence electronic structure to be relaxed at fixed atomic configuration. The total energy difference between the two calculations is an estimate of the core-level binding energy, without taking into account the effect of core-electron screening (although screening by valence electrons is included). The method is not able to yield absolute values for the core-level binding energies,[48] and in any case, the calculation of such absolute values from DFT is fundamentally problematic.[49] Therefore, one must consider core-level binding energy shifts, $\Delta \mathrm{BE}_{\mathrm{CL}}(\mathrm{A})$, instead. These can be defined as the difference in energy of specific core-electrons $\mathrm{BE}_{\mathrm{CL}}$ between an atom A and a reference atom $\mathrm{A}_{\mathrm{ref}}$:

$$\Delta \mathrm{BE}_{\mathrm{CL}}(\mathrm{A}) = \mathrm{BE}_{\mathrm{CL}}(\mathrm{A}) - \mathrm{BE}_{\mathrm{CL}}(\mathrm{A}_{\mathrm{ref}}) \tag{2.24}$$

In all cases the reference atom was the one yielding the lowest core-level binding energy. Finally, in order to allow a visual comparison between experimental and theoretical data, spectra were modelled by sums of Gaussians with equal width and height, centered at the respective experimental binding energy shifts (Chapter 2) or centered at the experimental binding energy (Chapter 3).

## 2.6 REFERENCES

1 F. Jensen, *Introduction to Computational Chemistry Computational Chemistry*, John Wiley & Sons, 2007.

2 M. Jammer, *The Conceptual Development of Quantum Mechanics*, Tomash Publishers, 2nd edn., 1989.

3 I. N. Levine, *Quantum Chemistry*, Pearson Education, 7th edn., 2013.

4 P. Hohenberg and W. Kohn, *Phys. Rev.*, 1964, **136**, B864–B871.

5 W. Kohn and L. J. Sham, *Phys. Rev.*, 1965, **140**, A1133–A1138.

6 E. . Lewars, *Computational Chemistry: Introduction to the Theory and Applications of Molecular and Quantum Mechanics*, Springer, 2011.

7 J. P. Perdew, in *AIP Conference Proceedings*, AIP, 2001, vol. 577, pp. 1–20.

8 J. P. Perdew, A. Ruzsinszky, J. Tao, V. N. Staroverov, G. E. Scuseria and G. I. Csonka, *J. Chem. Phys.*, 2005, **123**, 062201.

9 W. J. Carr, *Phys. Rev.*, 1961, **122**, 1437–1446.

10 S. H. Vosko, L. Wilk and M. Nusair, *Can. J. Phys.*, 1980, **58**, 1200–1211.

11 J. P. Perdew and Y. Wang, *Phys. Rev. B*, 1992, **45**, 13244–13249.

12 S. Kurth, J. P. Perdew and P. Blaha, *Int. J. Quantum Chem.*, 1999, **75**, 889–909.

13 A. Zupan, K. Burke, M. Ernzerhof and J. P. Perdew, *J. Chem. Phys.*, 1997, **106**, 10184–10193.

14 J. P. Perdew, J. A. Chevary, S. H. Vosko, K. A. Jackson, M. R. Pederson, D. J. Singh and C. Fiolhais, *Phys. Rev. B*, 1992, **46**, 6671–6687.

15 J. P. Perdew, K. Burke and M. Ernzerhof, *Phys. Rev. Lett.*, 1996, **77**, 3865–3868.

16 G. I. Csonka, J. P. Perdew, A. Ruzsinszky, P. H. T. Philipsen, S. Lebègue, J. Paier, O. A. Vydrov and J. G. Ángyán, *Phys. Rev. B - Condens. Matter Mater. Phys.*, 2009, **79**, 155107.

17 Y. Zhang and W. Yang, *Phys. Rev. Lett.*, 1998, **80**, 890–890.

18 J. P. Perdew, A. Ruzsinszky, G. I. Csonka, O. A. Vydrov, G. E. Scuseria, L. A. Constantin, X. Zhou and K. Burke, *Phys. Rev. Lett.*, 2008, **100**, 136406.

19 P. Haas, F. Tran and P. Blaha, *Phys. Rev. B*, 2009, **79**, 085104.

20 C. Adamo, M. Ernzerhof and G. E. Scuseria, *J. Chem. Phys.*, 2000, **112**, 2643–2649.

21 J. Tao, J. P. Perdew, V. N. Staroverov and G. E. Scuseria, *Phys. Rev. Lett.*, 2003, **91**, 146401.

22 J. Harris, *Phys. Rev. A*, 1984, **29**, 1648–1659.

23 A. D. Becke, *J. Chem. Phys.*, 1993, **98**, 5648–5652.

24 P. J. Stephens, F. J. Devlin, C. F. Chabalowski and M. J. Frisch, *J. Phys. Chem.*, 1994, **98**, 11623–11627.

25 M. Ernzerhof and G. E. Scuseria, *J. Chem. Phys.*, 1999, **110**, 5029–5036.

26 V. N. Staroverov, G. E. Scuseria, J. Tao and J. P. Perdew, *J. Chem. Phys.*, 2003, **119**, 12129–12137.

27 V. N. Staroverov, G. E. Scuseria, J. Tao and J. P. Perdew, *J. Chem. Phys.*, 2004, **121**, 11507.

28 L. Goerigk and S. Grimme, *Wiley Interdiscip. Rev. Comput. Mol. Sci.*, 2014, **4**, 576–600.

29 A. Görling and M. Levy, *Phys. Rev. B*, 1993, **47**, 13105–13113.

30 Y. Zhang, X. Xu and W. A. Goddard, *Proc. Natl. Acad. Sci. USA*, 2009, **106**, 4963–4968.

31 S. Grimme, *J. Chem. Phys.*, 2006, **124**, 034108.

32 J. Klimeš and A. Michaelides, *J. Chem. Phys.*, 2012, 137, 120901.

33 S. Grimme, *J. Comput. Chem.*, 2006, **27**, 1787–99.

34 S. Grimme, J. Antony, S. Ehrlich and H. Krieg, *J. Chem. Phys.*, 2010, **132**, 154104.

35 L. Goerigk and S. Grimme, *Phys. Chem. Chem. Phys.*, 2011, **13**, 6670–88.

36 M. Dion, H. Rydberg, E. Schröder, D. C. Langreth and B. I. Lundqvist, *Phys. Rev. Lett.*, 2004, **92**, 246401–1.

37 D. Nabok, P. Puschnig and C. Ambrosch-Draxl, *Comput. Phys. Commun.*, 2011, **182**, 1657–1662.

38 J. Klimeš, D. R. Bowler and A. Michaelides, *Phys. Rev. B*, 2011, **83**, 195131.

39 J. Klimeš, D. R. Bowler and A. Michaelides, *J. Phys. Condens. Matter*, 2010, **22**, 022201.

40 E. Kaxiras, *Atomic and Electronic Structure of Solids*, Cambridge University Press, New York, 2003.

41 D. S. Sholl and J. A. Steckel, *Density Functional Theory: A Practical Introduction*, John Wiley & Sons, Hoboken, New Jersey, 2009.

42 H. J. Monkhorst and J. D. Pack, *Phys. Rev. B*, 1976, **13**, 5188–5192.

43 D. R. Hamann, M. Schlüter and C. Chiang, *Phys. Rev. Lett.*, 1979, **43**, 1494–1497.

44 D. Vanderbilt, *Phys. Rev. B*, 1990, **41**, 7892–7895.

45 P. E. Blöchl, *Phys. Rev. B*, 1994, **50**, 17953–17979.

46 G. Makov and M. Payne, *Phys. Rev. B*, 1995, **51**, 4014–4022.

47 M. Birgersson, C.-O. Almbladh, M. Borg and J. Andersen, *Phys. Rev. B*, 2003, **67**, 045402.

48 L. Köhler and G. Kresse, *Phys. Rev. B*, 2004, **70**, 165405.

49 N. Pueyo Bellafont, P. S. Bagus and F. Illas, *J. Chem. Phys.*, 2015, **142**, 214102.

# 3 Adsorption of methyl acetoacetate on Ni{111} and Ni{100} surfaces

This Chapter presents a combined experimental and theoretical investigation of the geometry of adsorption of methyl acetoacetate on Ni{111} and Ni{100} surfaces. The results are discussed from a theoretical perspective, but we mention the results from our experimental collaborators where pertinent. The work discussed in this Chapter has been published in two combined theoretical-experimental papers in the *Journal of Physical Chemistry C*.[1,2]

## 3.1 INTRODUCTION

The hydrogenation of $\beta$-keto esters over modified Raney nickel opens up a pathway into enantioselective heterogeneous catalysis of bio-related molecules, with much of the characterization of this reaction in terms of kinetics, modifier and solvent dependence done by Izumi and coworkers in the 1960's.[3,4] The quantitative characterization at molecular scale and the understanding of chiral and chirally-modified surfaces of model catalysts experienced a rapid growth over the last two decades, driven by the refinement of experimental surface characterization techniques and theoretical modeling.[5–8] This progress has also been driven by the increasing demand for enantiopure chemicals in drug manufacturing, where homogeneous catalytic processes are predominantly used.[9] However, the subsequent phase separation necessary in homogeneous catalysis is difficult and generally expensive. The use of heterogeneous catalysts avoids this problem; therefore, viable heterogeneous routes would make the production of pharmaceuticals greener and more economical.

In the case of the simplest $\beta$-ketoester, methyl acetoacetate (MAA), the hydrogenation results in a racemic mixture of *R* and *S* methyl-3-hydroxybutyrate (M3HB) when performed with an unmodified Raney Ni catalyst. Modification of the catalyst with $\alpha$-amino or $\alpha$-hydroxy acids, however, can lead to results in high enantiomeric excess, up to 86%. The reaction is well characterized in terms of macroscopic quantities such as enantiomeric excess, temperature and solvent dependencies.[3,10–12] Izumi *et al.* suggested that the surface modification is due to a combination of modifier and solvent molecules since the solvent has a significant influence on the enantiomeric excess and corrosion of the catalyst. They also led to the conclusion that the enantioselective behavior depends on how the reactant MAA adsorbs on the Ni surface, and how it interacts with the modifier, rather than on the transition state of the hydrogenation reaction. Hence, determining the adsorption geometry of MAA at the molecular level and the influence modifiers have on it, is a key step to understand and optimize the enantioselective behavior of Ni-based catalysts.

On close-packed single crystal surfaces of many coinage and Pt-group metals, chiral modifiers and/or reactants often form ordered adsorbate layers with well-defined chemical environments under ultra-high vacuum (UHV) conditions. On Ni surfaces such ordered structures are rare. Therefore, little quantitative molecular-scale information is available on reactants and modifiers of enantioselective reactions on these surfaces. Raval and coworkers studied the adsorption of tartaric acid on Ni{110} and showed that the interaction with the modifier caused a chiral reconstruction of the surface.[13–15] Held's group has studied the adsorption of alanine on Ni{111} using X-ray photoemission spectroscopy (XPS) and near-edge X-ray absorption fine structure (NEXAFS) spectroscopy.[16] This and earlier studies have shown that the combination of these two techniques is very powerful in characterizing the adsorption complex in terms of chemical state, bond coordination, and molecular orientation.[16–20] These experimental and theoretical studies[12,13,15,16,21–23] show that the behavior of amino acid modifiers on Ni is very different from that on Cu surfaces.[24,25] On Cu, deprotonated anionic species are reported with adsorption geometries exhibiting a typical tridentate "OON" footprint. In the Ni case, anionic adsorption species are found to be coadsorbed with zwitterionic species, which is more comparable with the situation on Pd{111}surfaces.[26,27]

The adsorption of MAA and several modifiers on Ni{111} was studied by Baddeley's group using temperature-programmed desorption (TPD), infrared (IR) spectroscopy and scanning tunneling microscopy (STM). It has been reported that the spatial configuration between the modifiers and the substrate depends on the coverage and adsorption temperature. Evidence was found for a one-to-one interaction between the chiral modifiers and MAA. In addition, it was shown that the experimental conditions, temperature in particular, influence the keto-to-enol ratio of MAA.[12,22,23,28,29] To our knowledge, very little molecular-level information is available on the adsorption complex of the reactant. This chapter, therefore, provides a complete picture of the adsorption complex of the reactant on Ni{111} and Ni{100} surfaces.

## 3.2 COMPUTATIONAL METHODS

Periodic Density Functional theory (DFT) calculations were performed using planewave basis sets as implemented in VASP.[30,31] Following the approach of previous DFT investigations of molecular adsorption on Ni{111} and Ni{100} surfaces,[32–34] both structures were modeled with a periodic slab of 4 atomic layers (**Figure 3.1**). Only the two uppermost Ni layers were fully relaxed, while the two bottom layers were fixed in their bulk positions. A vacuum gap of 12 Å was included above the surfaces in order to avoid interactions between periodic cells. Laterally, both supercells consisted of (5×5) surface unit cells, which corresponds to a surface coverage Θ = 0.04 ML (one molecule per 25 surface Ni atoms). As nickel is a ferromagnetic metal, all calculations included spin polarization.

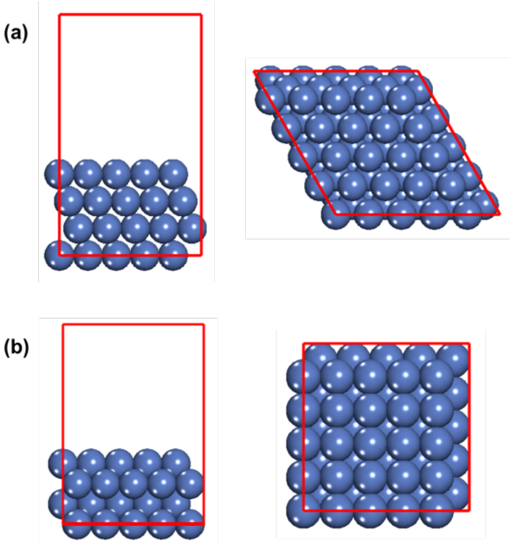

**Figure 3.1** Side and top view of the slab models used in the calculations for the adsorption of MAA on (a) Ni{111} and (b) Ni{100} surfaces.

The projector augmented wave (PAW) method[35,36] was used to describe the interaction between the valence and core electrons. The planewaves were limited by a kinetic energy cutoff of 400 eV, which is the recommended value for the employed PAW potentials. Monkhorst–Pack grids[37] with a maximum separation of 0.15 $Å^{-1}$ between **k**-points were used for sampling the Brillouin-zone; this grid density corresponds to a 4×4×1 grid for the reciprocal space of the slab model. The threshold for forces on the Ni ions was set to 0.02 eV $Å^{-1}$ and the positions of the MAA molecule were also allowed to fully relax. In order to compensate for the use of an asymmetric slab, all simulations included a dipole correction as implemented in VASP, based on a method proposed by Makov and Payne.[38]

The revised Perdew–Burke–Ernzerhof (revPBE) exchange-correlation functional[39] was used to perform the simulations. In order to account for van der Waals (vdW) interactions, the DFT-D3 method with Becke–Johnson (BJ) damping was used.[40,41] This combination of functional and dispersion correction has been shown to provide a very robust description of vdW effects in comparison with other GGA-based formulations.[42] For bulk Ni, the calculated lattice constant $a$ (3.458 Å) and magnetic moment (0.60 $\mu_{\mathrm{B}}$) agree well with experimental values (3.524 Å and 0.61 $\mu_{\mathrm{B}}$).

The exploration of the configurational space of adsorption was done by performing energy minimizations starting from all sensible initial positions of the MAA molecule with respect to the surface, and considering both tautomeric forms of the molecule as well as its deprotonated form. For each final stable adsorption configuration, the adsorption energy ($E_{\mathrm{ads}}$) was calculated as follows:

$$E_{\mathrm{ads}} = E_{\mathrm{slab+mol}} - (E_{\mathrm{slab}} + E_{\mathrm{mol}}) \tag{3.1}$$

where $E_{\mathrm{slab+mol}}$ represents the energy of the optimized substrate-adsorbate system, $E_{\mathrm{slab}}$ corresponds to the energy of the relaxed clean Ni surface, and $E_{\mathrm{mol}}$ denotes the energy of the MAA molecule in the gas phase, in the lowest-energy tautomeric configuration.

In the particular case of the Ni{100} system, the effect of zero-point energy (ZPE) on the adsorption energy was considered by calculating the vibrational frequencies of the adsorbed molecule (keeping frozen the atoms of the metal surface) and the frequencies of the gas phase molecule were estimated by using a finite-difference method. The ZPE values, i.e. half the sum of the vibrational frequencies in each case, were then added to the ground-state energies $E_{\mathrm{slab+mol}}$ and $E_{\mathrm{mol}}$, respectively, in **Equation 3.1**. This approach assumes that adsorption does not alter significantly the vibrational modes of the heavy metal atoms at the surface.

The theoretical core-level binding energy shifts $\Delta BE_{CL}$ of the O 1*s* levels of the oxygen atoms within the MAA were obtained in the so-called final-state approximation,[43] as described in Chapter 2. Simulated spectra were then modeled by sums of Gaussians with equal width and height, centered at the respective experimental binding energy (BE) shifts.

## 3.3 RESULTS

### 3.3.1 DFT simulation of gas-phase MAA

MAA belongs to the class of *β*–diketones of the type R–C(O)–$CH_2$–C(O)–R. The keto-enol tautomerism of these compounds depends strongly on the substituent R. Symmetrically substituted *β*-diketones exist in the enol form R–C(OH)=CH–C(O)–R when R is $CH_3$, and in the diketo form R–C(O)–$CH_2$–C(O)–R when R is $OCH_3$.[44] Both substituents are present in MAA, making its tautomeric behavior interesting: MAA vapor at 309 K exhibits a composition of 80% enol and 20% diketo form,[45] whereas liquid MAA at room temperature exists exclusively in the diketo form.[46] The crystal structure also exhibits only the diketo tautomer.[47]

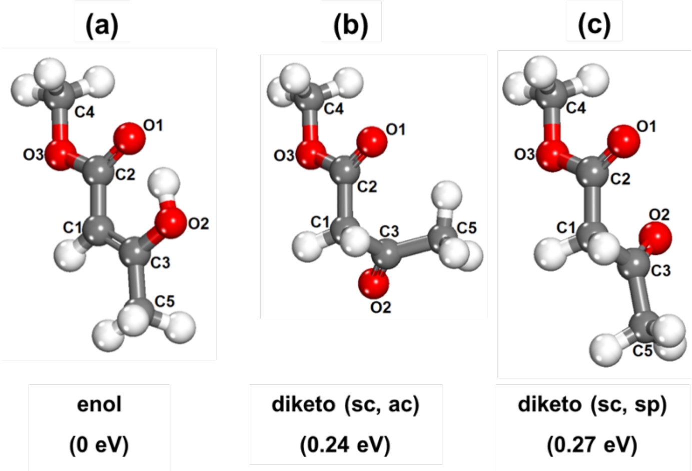

enol (0 eV)

diketo (sc, ac) (0.24 eV)

diketo (sc, sp) (0.27 eV)

**Figure 3.2** Molecular structures of the two MAA tautomers: (a) enol and (b, c) diketo. The terms "ac", "sc" and "sp" stand for anticlinal, synclinal and synperiplanar, respectively, which refer to the torsion angle (an important parameter in describing the conformation of many bio-related molecules).

**Table 3.1** Experimental and calculated geometric parameters of the enol tautomer of MAA. For numbering of the atoms refer to **Figure 3.2a**.

| Parameters (Å, degrees) | Exp.[45] | This work |
|---|---|---|
| *d*(C1–C2) | 1.449 | 1.445 |
| *d*(C1–C3) | 1.362 | 1.374 |
| *d*(C3–C5) | 1.493 | 1.497 |
| *d*(C2–O1) | 1.248 | 1.254 |
| *d*(C3–O2) | 1.339 | 1.344 |
| *d*(C2–O3) | 1.347 | 1.363 |
| *d*(O3–C4) | 1.437 | 1.450 |
| ∠C2C1C3 | 120.0 | 119.8 |
| ∠C1C2O1 | 121.6 | 124.5 |
| ∠C1C3O2 | 126.7 | 122.3 |
| ∠C1C2O3 | 115.1 | 113.6 |
| ∠C1C3C5 | 122.4 | 123.9 |
| ∠C2O3C4 | 113.3 | 115.3 |
| ∠(C3C1C2O1) | - | 0.0 |
| ∠(C2C1C3O2) | - | 0.0 |

The set of geometries in the present study included the two tautomeric forms of the isolated molecule, considering also different conformations. **Figure 3.2** shows the three most stable structures predicted by DFT. As expected from experiment, the most stable structure in the gas phase corresponds to the enol tautomer, with the hydroxyl adjacent to the methyl group (the other configuration, with the hydroxyl adjacent to the methoxy group, is considerably less stable by 1.2 eV). The geometry optimization of the enol tautomer leads to a “planar” structure, where all the oxygen atoms are contained in the plane defined by the three carbon atoms (**Figure 3.2a**). Previous theoretical work at B3LYP and MP2 level led to similar results.[45] The computed geometry of the enol tautomer, shown in **Table 3.1**, agrees well with available experiment data:[45] the discrepancies in interatomic distances are all within ~1%.

**Table 3.2** Calculated geometric parameters of the diketo tautomer of MAA in comparison to the available experimental data.[47] Two stable conformation of this tautomer are feasible, depending on the relative orientation of the C=O bonds. For numbering of the atoms refer to **Figure 3.2b,c**.

| **Parameters (Å, degrees)** | **Exp.**[47] | **diketo (sc, ac)** | **diketo (sc, sp)** |
|---|---|---|---|
| *d*(C1–C2) | 1.500 | 1.518 | 1.515 |
| *d*(C1–C3) | 1.519 | 1.547 | 1.539 |
| *d*(C3–C5) | 1.492 | 1.513 | 1.518 |
| *d*(C2–O1) | 1.200 | 1.224 | 1.222 |
| *d*(C3–O2) | 1.211 | 1.225 | 1.224 |
| *d*(C2–O3) | 1.333 | 1.363 | 1.362 |
| *d*(O3–C4) | 1.446 | 1.453 | 1.453 |
| ∠C2C1C3 | 112.3 | 111.4 | 112.4 |
| ∠C1C2O1 | 124.5 | 125.4 | 124.7 |
| ∠C1C3O2 | 121.2 | 120.3 | 122.2 |
| ∠C1C2O3 | 112.0 | 110.5 | 110.8 |
| ∠C1C3C5 | 115.3 | 116.7 | 115.0 |
| ∠C2O3C4 | 116.3 | 115.1 | 114.9 |
| ∠(C3C1C2O1) | - | -87.5 | -87.7 |
| ∠(C2C1C3O2) | - | -119.9 | -12.6 |

For the diketo tautomer the two most stable conformers (**Figure 3.2b,c**) have similar energies (0.24 eV and 0.27 eV above the enol groundstate). **Table 3.2** lists the geometrical parameters of these two MAA conformers, in comparison with the experimental values for the diketo molecule in the crystal structure.[47] The main difference between the two theoretical diketo structures is in the dihedral angle ∠(C2C1C3O2), which makes the *d*(C4–C5) distance in diketo (sc, ac) shorter than its counterpart by 0.95 Å. The crystal structure of MAA at 150 K contains discrete molecules,[47] whose geometrical configuration is very similar to diketo (sc, sp). Since our calculations predict that the diketo (sc, ac) conformer is only slightly more stable than the diketo (sc, sp) conformer (in the gas phase), our result is not in disagreement with the experimental observation for the solid: the intermolecular interactions apparently stabilize the diketo (sc, sp) over the diketo (sc, ac) form. Because the enol form is the most stable tautomer, we use it as the reference for the calculation of adsorption energies (**Equation 3.1**) regardless of the mode of adsorption.

### 3.3.2 Adsorption of MAA on Ni{111} surfaces

Various local minima resulted from simulations when testing adsorption geometries on Ni{111} surfaces, which include a flat surface and a surface with adatoms. The four most stable configurations are shown in **Figure 3.3.** In the case of MAA adsorbed on a flat Ni{111} surface, the global minimum corresponds to the *bidentate deprotonated* configuration shown in **Figure 3.3a**, where the MAA molecular plane is tilted with respect to the surface, to which it is bonded via two carbonyl groups: one (adjacent to methyl group) on a hollow-*fcc* site and the other (adjacent to methoxy group) on an atop site. The dissociated hydrogen atom is adsorbed elsewhere on the surface, preferentially on an *fcc* site; the same adsorption mode, but with the hydrogen adsorbed on an *hcp* site, is 9 meV higher in energy.

**Figure 3.3b** shows the second lowest-energy geometry of MAA (in its enol tautomeric form) adsorbed on the flat Ni{111} surface. In this case, the molecular plane is parallel to the surface with all three oxygen atoms above atop sites. This adsorption geometry (*flat enol*) involves significant vdW interactions between the molecule and the surface. Configurations that involve diketo-MAA adsorption on flat Ni{111} surfaces are less stable by at least 0.5 eV compared with the flat enol geometry; therefore, they can be safely disregarded as potential candidates.

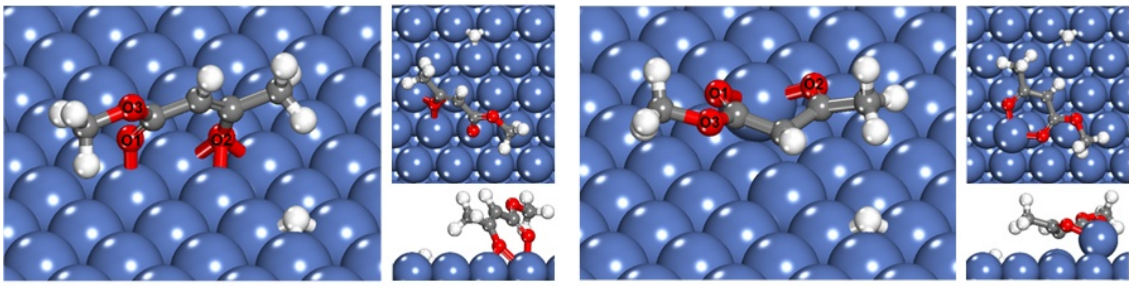

(a) bidentate deprotonated (-1.51 eV)

(c) bidentate deprotonated on adatom (-2.45 eV)

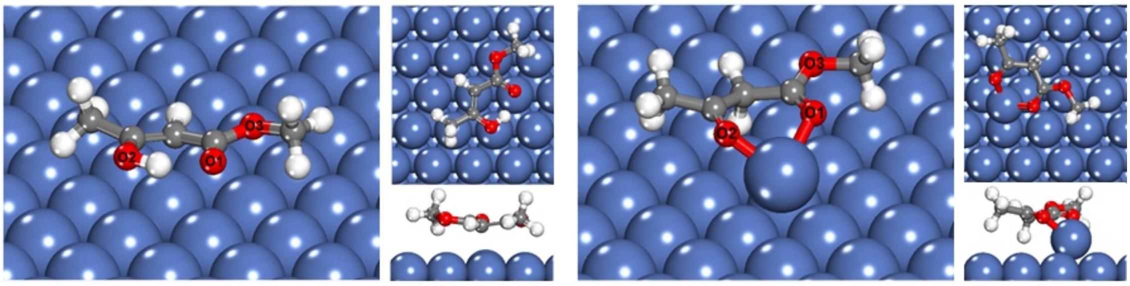

(b) flat enol (-1.44 eV)

(d) bidentate diketo on adatom (-1.84 eV)

**Figure 3.3** The four lowest-energy configurations of adsorption of MAA at the Ni{111} surfaces. Red atoms correspond to oxygen atoms, grey to carbon atoms and white to hydrogens. Oxygen atoms are numbered in line with **Figure 3.2** and with the discussion of core-level shifts below. Key: red = O, gray = C, white = H, and blue = Ni.

Early theoretical work using the classical embedded-atom method (EAM) calculated a low activation energy (56 meV) for migration of Ni adatom at the Ni{111} surface,[48] which suggests that adatoms which formed, for example, by detachment from surface edges will be very mobile and readily available for the adsorption of molecules. The potentially important role of metal adatoms on molecular adsorption at metal surfaces has been highlighted in more recent studies.[49] Therefore, the investigation includes candidates of MAA adsorbed at Ni adatoms on Ni{111}. To simulate this type of defect, an adatom was added on one side of the perfect slab, giving a ~4% coverage of Ni adatoms. Due to the stacking of the planes of Ni atoms in the {111} direction, there are two types of hollow sites on the {111} terrace for the adatom to be located, each threefold coordinated by three close-packed Ni atoms in the surface: the *fcc* site and the *hcp* site. We did not consider other sites for the adatom, i.e., on *top* of the Ni surface atoms and in a *bridge* site, between and *fcc* and *hcp* site. In a similar case, adatoms on Cu{111} surface placed on these latter positions always moved toward either the *fcc* or *hcp* hollow sites.[50] We have found that the hollow *fcc* site is more favorable than the hollow *hcp* site by 8 meV. A previous work based on GGA-PW91 reported that the *fcc* site is 30 meV more stable than the *hcp* site.[51] Thus, the calculations were carried out with the *fcc*-adatom Ni{111} surfaces, which is almost identical to the *hcp*-adatom for the adatom/adsorbate interaction.

Two different stable configurations for the MAA molecule on the adatom were found, in which MAA interacts with the Ni adatom via the carboxylic groups. In both cases, the molecular plane is almost parallel to the Ni{111} surface (see **Figure 3.3c,d**). In the first "*bidentate deprotonated on adatom*" configuration (**Figure 3.3c**), with an adsorption energy of -2.45 eV, MAA is deprotonated with the dissociated hydrogen atom adsorbed at an *fcc* site. This is 18 meV lower in energy than hydrogen adsorption on the *hcp* site with the same MAA-Ni adsorption complex. The second more stable adatom complex "*bidentate diketo on adatom*", shown in **Figure 3.3d,** is less stable than the previous one by more than 0.6 eV. This is the only diketo adsorption configuration found in our calculations that can be considered as a potential candidate, and is unlikely to compete with the stronger adsorption mode in the presence of adatoms. This is interesting, since previous experimental work on co-adsorption of glutamate and MAA on Ni{111} suggested that the MAA was adsorbed in a parallel geometry in the diketo form at 300K.[23]

To compare rationally the adsorption energies on the flat surface with those on an adatom, the latter should take into account the energy cost of creating the adatom in the first place. The formation energy ($E_f$) of the adatom was evaluated in two scenarios (**Figure 3.4**): (a) formation from a step edge, leaving an edge vacancy behind (b) formation from the flat terrace, leaving a terrace vacancy. As expected, scenario (a) leads to much lower formation energy ($E_\mathrm{f}^{(\mathrm{a})}$ = 0.19 eV) than scenario (b) ($E_\mathrm{f}^{(\mathrm{b})}$ = 2.26 eV).

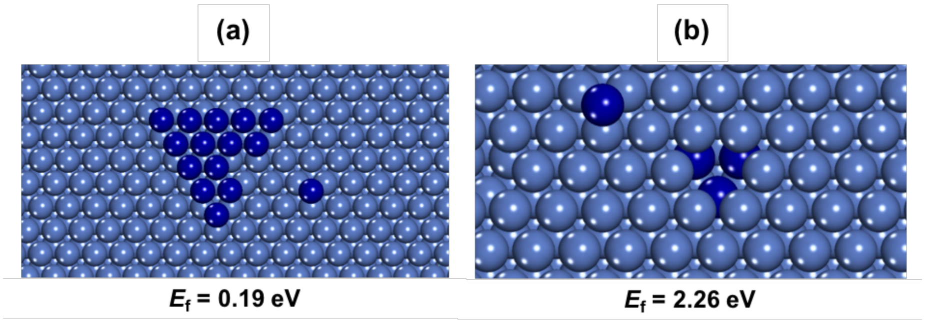

**Figure 3.4** Representation of adatoms coming from (a) steps and (b) surface. The formation energy of adatoms ($E_\mathrm{f}$) in each case was calculated using a bigger supercell, which consisted of (7×7) surface unit cells – ensuring isolated species. The triangular island model was used to simulate the step. The adatoms, the step and the atoms underneath the vacancy left by the formed-adatom are shaded darker.

Clearly, adding the adatom formation energy from the terrace sites, makes both adatom adsorption configurations unfavorable compared to adsorption directly on the flat terrace. However, if the adatom is formed from a step edge, the overall adsorption energy for the *bidentate deprotonated on adatom* is -2.45 eV + 0.19 eV = -2.26 eV. This means that MAA adsorption can in principle stabilize the adatom formation from a step edge, in a process that is energetically more favorable than direct adsorption at the terrace site with no adatoms involved. Of course, these results only refer to the thermodynamic preference; it is possible that there are kinetic limitations for the edge-to-adatom mechanism, especially at the high MAA coverages of interest here. It is therefore difficult to predict, from energy calculations only, what the predominant mode of adsorption is, and whether or not it involves Ni adatoms. We need to resort to the comparison of the experimental XPS spectra with the simulated spectra for the different adsorption configurations.

#### 3.3.2.1 Comparison of modeling and XPS data

In order to compare the above candidate structures with experimental XPS data,[1] theoretical core-level binding energy shifts of the O 1*s* levels were obtained according to **Equation 2.24**. The results are summarized in **Table 3.3** together with some key geometrical data. In all four cases the binding energy shifts split into two groups around $\Delta \mathrm{BE}_{\mathrm{O}1s}$ = 0.00 – 0.60 eV and $\Delta \mathrm{BE}_{\mathrm{O}1s}$ = 1.44 – 2.55 eV. With the exception of the "flat enol" configuration, the two oxygen atoms from the carboxylic groups (O1 and O2) are characterized by the lower BE. The oxygen atom of the $OCH_3$ group (O3) always leads to a high BE.

**Table 3.3** Key geometrical and spectroscopic parameters of the candidate structures with the lowest adsorption energies found by DFT for the case of Ni{111} surface. The parameter Δz (C) is the maximum difference in height of the molecule's carbon atoms with respect to the surface. Only relative shifts of O 1*s* are given according to **Equation 3.2**. For numbering refer to **Figure 3.2**.

| | **Bidentate deprotonated** | **Flat enol** | **Bidentate deprotonated on adatom** | **Bidentate diketo on adatom** |
|---|---|---|---|---|
| $E_{\mathrm{ads}}$ | -1.51 eV | -1.44 eV | -2.45 eV | -1.84 eV |
| $E_{\mathrm{ads}} + E_{\mathrm{f}}^{(\mathrm{a})}$ | - | - | -2.26 eV | -1.65 eV |
| d(C2–O1) | 1.262 Å | 1.256 Å | 1.258 Å | 1.243 Å |
| d(C3–O2) | 1.343 Å | 1.336 Å | 1.279 Å | 1.251 Å |
| ∠C2–O1–surface | 47.8° | 11.2° | 6.4° | 7.4° |
| ∠C3–O2–surface | 61.5° | 5.0° | 2.7° | 10.1° |
| Δz (C) | 0.733 Å | 0.621 Å | 1.057 Å | 0.482 Å |
| $\Delta \mathrm{BE}_{\mathrm{O}1s}$O1 | 0.00 eV | 0.00 eV | 0.33 eV | 0.60 eV |
| $\Delta \mathrm{BE}_{\mathrm{O}1s}$O2 | 0.38 eV | 1.44 eV | 0.00 eV | 0.00 eV |
| $\Delta \mathrm{BE}_{\mathrm{O}1s}$O3 | 1.96 eV | 1.96 eV | 2.16 eV | 2.55 eV |

A better comparison of the calculated chemical shifts with the experimental O 1*s* XPS data is achieved by simulating XPS spectra. For each Gaussian a width of 1.4 eV was used, which is the smallest width measured for the experimental O 1*s* peaks.[1] These model spectra are plotted in **Figure 3.5** together with the experimental O 1*s* spectrum of MAA at 53 % of saturation coverage (1 MAA per 15 Ni atoms) dosed at 180 K.[1] This spectrum has been chosen for comparison as the coverage is the closest to the coverage used in the model calculations (1 MAA per 25 Ni atoms). The BE scale of the experimental spectrum has been shifted such that it coincides with the model spectra.

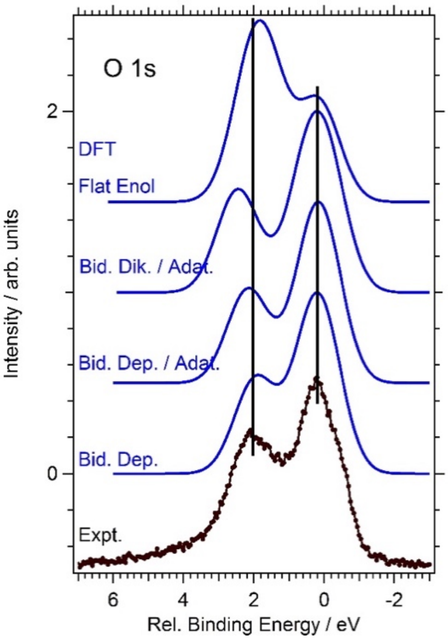

**Figure 3.5** Model O 1*s* spectra for the MAA geometries that lead to the lowest adsorption energies in the DFT calculations: (top down) flat enol, bidentate diketo on Ni adatom, bidentate deprotonated on Ni adatom, bidentate deprotonated on flat surface. Dots: experimental O 1*s* spectrum for 0.07 ML MAA dosed at 180 K.

None of the model spectra perfectly matches the peak height ratio of 1.56:1 (low BE : high BE), which is to be expected, as attenuation and photoelectron diffraction effects are not incorporated in the model spectra. However, except for that of the flat enol spectrum, all the simulated spectra are in qualitative agreement with the experimental relative peak heights. The energy separation of the two peaks is best reproduced by the two bidentate deprotonated models: $\Delta BE_{O1s}$ = 1.8 eV/2.0 eV for adsorption on the flat surface/Ni adatom while the experimental value is 1.94 eV. Thus, on the ground of the core-level shifts, we can only exclude the *flat enol* configuration with reasonable confidence.

#### 3.3.2.1 Comparison of modeling and NEXAFS data

A much clearer discrimination can be achieved from an analysis based on the NEXAFS[1] results and the DFT geometries. The experimental data suggested the presence of C-O bond angles of 49° and 62.5° with respect to the surface plane. These angles are almost exactly reproduced in the DFT simulations by the *bidentate deprotonated* configuration without adatom, with values of 47.8° and 61.5°, while all other geometries are characterized by angles of 11.2° or less. We therefore concluded that the molecular adsorption geometry observed in the experiments is in fact "bidentate deprotonated". The fact that the adatom geometries are not observed despite their lower adsorption energies as found by DFT modeling can be explained by the low temperatures of 250 K or less that the experiments were conducted. Significant adatom generation from step edges of Ni surfaces, however, takes place well above room temperature.[52] Therefore the formation of adatoms complexes appears to be kinetically hindered at low temperatures.

### 3.3.3 Adsorption of MAA on Ni{100} surface

As before, the simulations of the adsorption complex onto a Ni{100} surface included both tautomeric configurations of MAA. The candidates with the MAA in its diketo form were less stable by at least 0.8 eV compared to the two most stable enol species shown in **Figure 3.6**, therefore they were discarded. It is important also to mention that the simulation of the adsorption of MAA on Ni{100} was performed on *flat* surfaces only, given the results seen in the case of Ni{111} surfaces when adatoms are considered.

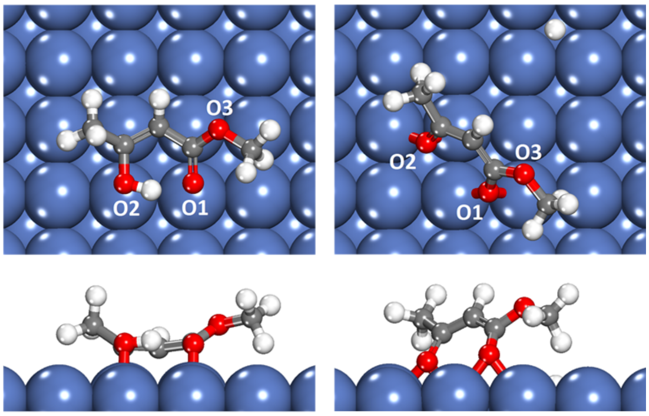

(a) flat enol (b) bidentate deprotonated

**Figure 3.6** Top and side view of the two lowest-energy configurations predicted by DFT for the adsorption of MAA on the Ni{100} surface.

In the Ni{100} surface, two potential candidates were found. The first local minimum corresponds to the *flat enol* configuration as shown in **Figure 3.6a**. The main molecular plane formed by the three carbons C2-C1-C3 (see **Figure 3.2** for numbering) is parallel to the surface with both oxygen atoms from the carbonyl and hydroxyl groups (O1 and O2) above atop sites. Unlike in the gas phase, the methyl and methoxy groups are not within this plane but bent away from the surface. The second global minimum (**Figure 3.6b**) corresponds to the *bidentate deprotonated* configuration, where the hydrogen in the O2 is missing and the molecular plane is tilted with respect to the Ni surface. The surface bond is formed via the carbonyl groups sited on bridge sites of non-adjacent rows. The dissociated hydrogen atom is adsorbed elsewhere on the surface on a four-hollow site. In this case, the methyl and methoxy groups remain aligned to the plane of the molecule. The calculated adsorption energies without vibrational contributions are -1.91 eV for the *flat enol* and -1.82 eV for the *bidentate deprotonated* configuration. When vibrational contributions are included, the change in ZPE between gas phase and the adsorbed species stabilizes the *bidentate deprotonated* by -0.20 eV but the *flat enol* only by -0.06 eV. This result is expected as the number of intramolecular bonds in the latter is the same as in the gas-phase molecule, whereas with the former deprotonation occurs and the adsorbed species has one bond less and the vibrations of the dissociated hydrogen atom bound to Ni are much softer. This extra stabilization yields a total adsorption energy (including electronic and vibrational contributions) of -2.02 eV for the "bidentate deprotonated" configuration compared to -1.97 eV for the "flat enol", hence rendering the former more stable.

#### 3.3.3.1 Comparison of modeling and XPS data

Comparison of simulated spectra for the two candidate adsorption and experimental XPS data[2] is now discussed. The $\Delta\mathrm{BE}_{O1s}$values, according to **Equation 2.24**, are listed in **Table 3.4**. For both adsorption geometries, the BE shifts split into two groups, around $\Delta\mathrm{BE}_{O1s}$= 0.00 – 0.29 eV and $\Delta\mathrm{BE}_{O1s}$ = 1.29 – 1.86 eV. For the *flat enol* conformation, the oxygen of the carboxylic group (O1) falls into the lower BE group and the oxygen atoms of the hydroxyl and methoxy groups (O2 and O3) into the higher BE group. In the *bidentate deprotonated* configuration, the two oxygen atoms of the carboxylic groups (O1 and O2) have low BE and the methoxy oxygen (O3) features a high BE.

In the modeling of XPS spectra, each Gaussian has a width of 1.5 eV, which was determined by the experimental data fitting.[2] **Figure 3.7** shows the individual Gaussians and their superposition alongside the experimental O 1*s* spectrum of MAA. Clearly, the simulated spectrum of the *bidentate deprotonated* geometry is in much better quantitative agreement with the experimental data than the one of the *flat enol*. Both the energy separation, 1.6 eV, and the relative heights of the two peaks fit the XPS data very well.

**Table 3.4** Key geometrical and spectroscopic parameters of the two candidate structures predicted by DFT for the case of Ni{100} surface. For numbering refer to **Figure 3.2**.

| | **Bidentate deprotonated** | **Flat enol** |
|---|---|---|
| $E_{\mathrm{ads}}^{\mathrm{DFT}}$ | -1.82 eV | -1.91 eV |
| $E_{\mathrm{ads}}^{\mathrm{DFT+ZPE}}$ | -2.02 eV | -1.97 eV |
| *d*(C2–O1) | 1.284 Å | 1.322 Å |
| *d*(C3–O2) | 1.331 Å | 1.423 Å |
| ∠C2–O1–surface | 49.1° | 0.0° |
| ∠C3–O2–surface | 53.2° | 0.7° |
| ∠C2–C1–C3–surface | 54.3° | 8.9° |
| Δz (C) | 0.640 Å | 1.118 Å |
| $\Delta\mathrm{BE}_{\mathrm{O1s}}$O1 (eV) | 0.29 eV | 0.00 eV |
| $\Delta\mathrm{BE}_{\mathrm{O1s}}$O2 (eV) | 0.00 eV | 1.29 eV |
| $\Delta\mathrm{BE}_{\mathrm{O1s}}$O3 (eV) | 1.86 eV | 1.63 eV |

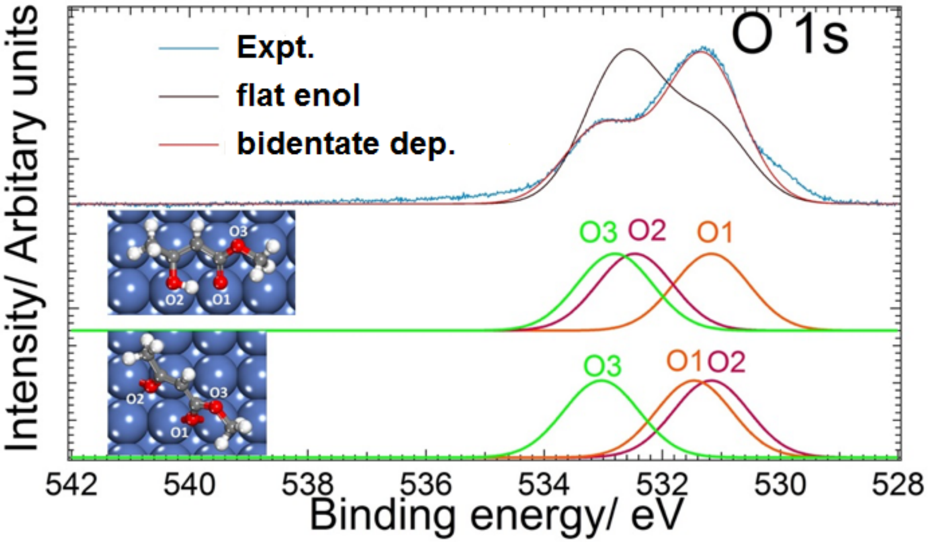

**Figure 3.7** Comparison of experimental XPS data and modeled XPS spectra of the *flat enol* and *bidentate deprotonated* configurations. Top: direct comparison of experimental and modeled spectra; middle: individual Gaussian peaks centered at the calculated core-level shifts for the *flat enol*; bottom: individual Gaussian peaks centered at the calculated core-level shifts for the *bidentate deprotonated*.

#### 3.3.3.2 Comparison of modeling and NEXAFS data

Additional confirmation for the *bidentate deprotonated* adsorption geometry comes from the NEXAFS data.[2] The DFT-optimized geometry predicts the molecular plane being tilted with respect to the surface plane. The calculated inclination angles for the C-O bonds are $\angle$C3–O2 = 53.2° and $\angle$C2–O1 = 49.1°; the plane of the carbon backbone has an angle of $\angle$C2–C1–C3 = 54.3° with respect to the surface (**Table 3.2**).

The NEXAFS spectra consist of three peaks in the $\pi^*$-resonance region, at 532.5 eV, 533.5 eV, and 535.3 eV (marked by arrows in **Figure 3.8a**), which are most likely associated with these bonds, as they all are expected to be part of a resonant $\pi$-system. In order to make the correlation between the molecular geometry and these resonances, the density of states (DOS) near the Fermi energy was calculated for the *bidentate deprotonated* adsorption complex. **Figure 3.8b** shows the total DOS (black line), the DOS associated with the molecule (green), and the projections onto the Ni 3*d*, O 2*p*, and C 2*p* states (blue, red, and grey, respectively).

**Figure 3.8b** clearly shows a high density of empty states in the vicinity of C and O atoms around 1.7 eV and 4.8 eV above the Fermi level, which are associated with resonant $\pi$-like orbitals extending over most of the molecule. The main contribution to the states at 1.7 eV above the Fermi level are near the C3-O2 and C2-O1 bonds pointing towards the surface (see top panel of **Figure 3.8b**), while the empty states at 4.8 eV are located near the plane formed by C2, C1, and C3 (bottom panel of **Figure 3.8b**). The energy difference between the two DOS maxima (~3.1 eV) is very close to the energy difference between peak 1 (532.5 eV) and peak 3 (535.3 eV) in the NEXAFS spectra; therefore the NEXAFS peaks 1 and 2 were assigned at 532.5 eV and 533.5 eV, respectively, to $\pi$-like orbital states associated with C-O bonds, while the peak at 535.33 eV is linked to the (C2C1C3) plane. A closer look at the top and bottom panel of **Figure 3.8b** shows that the respective orbitals are not exclusively associated with only one bond. Therefore, the angular dependence of the NEXAFS resonances, which is determined by the orientation of orbitals rather than bonds, must be expected to deviate somewhat from the bond orientation. However, the experimental values are clearly not compatible with the *flat enol* adsorption complex where the molecular plane is essentially parallel to the surface (tilt angles between 0.0° and 8.9°, see **Table 3.2**).

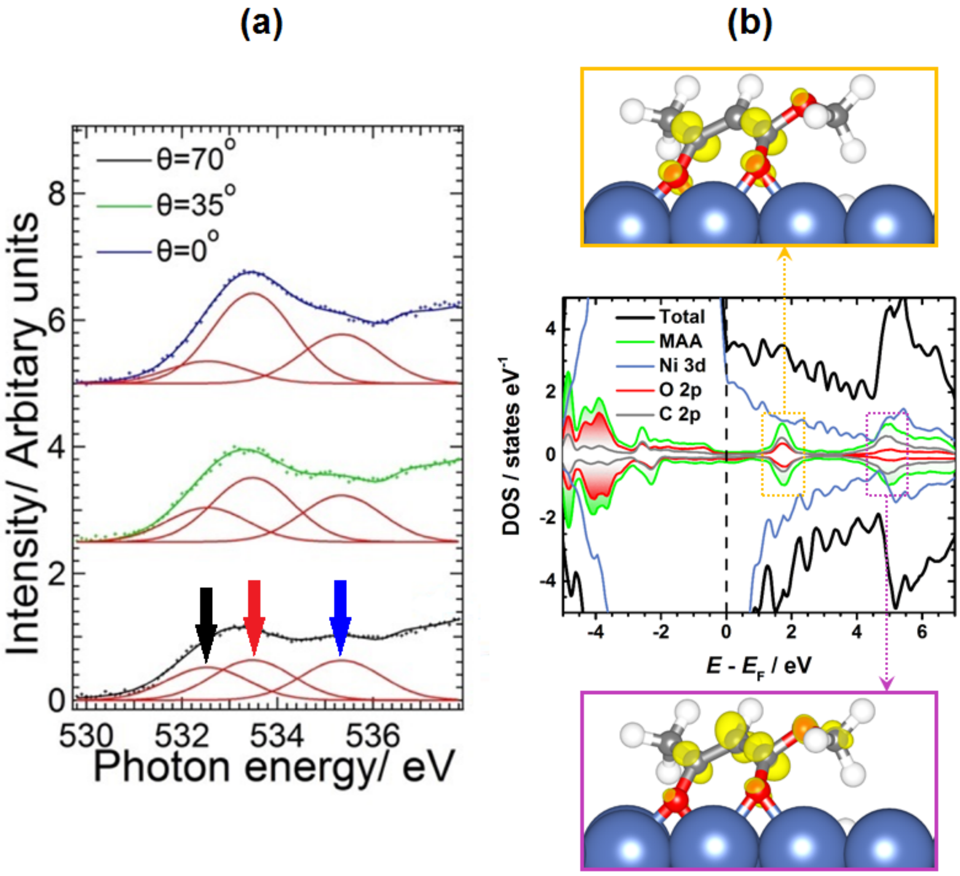

**Figure 3.8** (a) Angle resolved O K-edge NEXAFS spectra at energy range of $\pi^*$ resonances. The black, red and blue arrows mark the three peaks at 532.5 eV (peak 1), 533.5 eV (peak 2), and 535.3 eV (peak 3); respectively. (b) Density of states (DOS) of the *bidentate deprotonated* geometry (center). The charge density isosurfaces, corresponding to electronic states with energies between 1.28 and 2.22 eV (top) and 4.38 and 5.32 eV (bottom) above the Fermi level, are highlighted with dotted rectangles.

Based on the above comparison of experimental and computational results it can be confidently stated that MAA adsorbs on Ni{100} in a *bidentate deprotonated* geometry. It should be stressed that the small energy difference between the deprotonated and the enol adsorption species would not allow an unambiguous discrimination on the basis of DFT alone. Only the comparison with experimentally determined parameters, such as tilt angles and chemical shifts in XPS, makes a reliable determination of the adsorption complex possible.

## 3.4 IMPLICATIONS FOR HETEROGENEOUS CATALYSIS

The tilted adsorption geometry of the bidentate deprotonated species in both Ni surfaces offers a clear mechanism for enantioselective hydrogenation. If it is assumed that the dissociation of $H_2$ takes place on the Ni surface, it will be more likely for the dissociated hydrogen atom to attach to the molecule on the side that is tilted towards the surface. On unmodified Ni surfaces, the tilt can be in both directions; especially for the case of Ni{100} surface, which has a mirror symmetry. The role of a modifier is, therefore, to break the mirror symmetry and stabilize only one of two possible tilt directions. A similar mechanism would also explain enantioselectivity for the *flat enol* geometry or diketo structures that break the mirror symmetry of the surface in a similar way. Indeed, enol and diketo conformers of MAA lead to enantioselective products, as a series of IR absorption studies of MAA on glutamic-acid-modified Ni{111} in solution has shown.[12,23]

Further studies with co-adsorbed reactants and modifier molecules (alanine, for example) will be necessary to determine the exact geometry of the modifier-MAA complex at the molecular level and establish the reaction mechanism that leads to the formation of the chiral products.

## 3.5 CONCLUSIONS

In summary, this Chapter provides detailed information on the adsorption complex of MAA on Ni{111} and Ni{100} surfaces. DFT modeling predicts that the MAA enol tautomer is more stable than the diketo tautomer in the gas phase.

Deprotonated species with bidentate coordination is the preferred adsorption mode of MAA at the flat Ni{111} surface. The adsorption of the non-dissociated enol tautomer is less stable by 77 meV. The presence of adatoms leads to stronger MAA adsorption in comparison with the flat surface, whereby the stabilization energy is high enough for MAA to drive the formation of adatom defects at Ni{111} (assuming the adatoms come from surface steps). Calculation of oxygen core-level shifts for the theoretical adsorption geometries and comparison with the XPS together with the tilt angles derived from NEXAFS unambiguously identify the bidentate deprotonated enol on the flat Ni{111} surface as the dominant species, indicating that the formation of adatom adsorption complexes is kinetically hindered at low temperatures.

In a similar way, DFT calculations predict MAA-deprotonated species on Ni{100} surface, which are tilted with respect to the metallic surface and bonded through two oxygen atoms. Such conformers and the tilt angle between 49.1° and 54.3° with respect to the surface plane is confirmed by comparison with spectroscopic data. A non-deprotonated enol tautomer is less stable by 50 meV, when vibrational zero-point energy contributions are taken into account.

## 3.6 REFERENCES

1 J. Ontaneda, R. E. J. Nicklin, A. Cornish, A. Roldan, R. Grau-Crespo and G. Held, *J. Phys. Chem. C*, 2016, **120**, 27490–27499.

2 P. Tsaousis, J. Ontaneda, L. Bignardi, R. A. Bennett, R. Grau-Crespo and G. Held, *J. Phys. Chem. C*, 2018, **122**, 6186–6194.

3 Y. Izumi, *Adv. Catal.*, 1983, **32**, 215–271.

4 G. Webb and P. B. Wells, *Catal. Today*, 1992, **12**, 319–337.

5 A. Baiker, *J. Mol. Catal. A Chem.*, 1997, **115**, 473–493.

6 A. Baiker, *J. Mol. Catal. A Chem.*, 2000, **163**, 205–220.

7 C. J. Baddeley and G. Held, in *Comprehensive Nanoscience and Technology*, eds. D. Andrews, G. Scholes and G. Wiederrecht, Elsevier, Amsterdam, 2010, pp. 105–133.

8 C. J. Baddeley, T. E. Jones, A. G. Trant and K. E. Wilson, *Top. Catal.*, 2011, **54**, 1348–1356.

9 K. B. Sharpless, *Angew. Chemie Int. Ed.*, 2002, **41**, 2024–2032.

10 M. A. Keane, *Langmuir*, 1994, **10**, 4560–4565.

11 M. A. Keane, *Langmuir*, 1997, **13**, 41–50.

12 T. E. Jones, A. E. Rekatas and C. J. Baddeley, *J. Phys. Chem. C*, 2007, **111**, 5500–5505.

13 V. Humblot, S. Haq, C. Muryn, W. A. Hofer and R. Raval, *J. Am. Chem. Soc.*, 2002, **124**, 503–510.

14 V. Humblot, S. Haq, C. Muryn and R. Raval, *J. Catal.*, 2004, **228**, 130–140.

15 W. A. Hofer, V. Humblot and R. Raval, *Surf. Sci.*, 2004, **554**, 141–149.

16 R. E. J. Nicklin, A. Cornish, A. Shavorskiy, S. Baldanza, K. Schulte, Z. Liu, R. A. Bennett and G. Held, *J. Phys. Chem. C*, 2015, **119**, 26566–26574.

17 A. Shavorskiy, T. Eralp, K. Schulte, H. Bluhm and G. Held, *Surf. Sci.*, 2013, **607**, 10–19.

18 T. Eralp, A. Shavorskiy and G. Held, *Surf. Sci.*, 2011, **605**, 468–472.

19 T. Eralp, A. Ievins, A. Shavorskiy, S. J. Jenkins and G. Held, *J. Am. Chem. Soc.*, 2012, **134**, 9615–9621.

20 S. Baldanza, A. Cornish, R. E. J. Nicklin, Z. V. Zheleva and G. Held, *Surf. Sci.*, 2014, **629**, 114–122.

21 L. M. Ghiringhelli, P. Schravendijk and L. Delle Site, *Phys. Rev. B*, 2006, **74**, 035437.

22 T. E. Jones, M. E. Urquhart and C. J. Baddeley, *Surf. Sci.*, 2005, **587**, 69–77.

23 T. E. Jones and C. J. Baddeley, *Langmuir*, 2006, **22**, 148–52.

24 S. M. Barlow and R. Raval, *Surf. Sci. Rep.*, 2003, **50**, 201–341.

25 G. Held and M. J. Gladys, *Top. Catal.*, 2008, **48**, 128–136.

26 M. Mahapatra and W. T. Tysoe, *Surf. Sci.*, 2014, **629**, 132–138.

27 M. Mahapatra, L. Burkholder, S. P. Devarajan, A. Boscoboinik, M. Garvey, Y. Bai and W. T. Tysoe, *J. Phys. Chem. C*, 2015, **119**, 3556–3563.

28 T. E. Jones and C. J. Baddeley, *Surf. Sci.*, 2002, **519**, 237–249.

29 T. E. Jones and C. J. Baddeley, *Surf. Sci.*, 2002, **513**, 453–467.

30 G. Kresse and J. Furthmüller, *Comput. Mater. Sci.*, 1996, **6**, 15–50.

31 G. Kresse and J. Furthmüller, *Phys. Rev. B*, 1996, **54**, 11169–11186.

32 I. N. Remediakis, F. Abild-Pedersen and J. K. Nørskov, *J. Phys. Chem. B*, 2004, **108**, 14535–14540.

33 A. Mohsenzadeh, K. Bolton and T. Richards, *Surf. Sci.*, 2014, **627**, 1–10.

34 A. Mohsenzadeh, T. Richards and K. Bolton, *Surf. Sci.*, 2016, **644**, 53–63.

35 P. E. Blöchl, *Phys. Rev. B*, 1994, **50**, 17953–17979.

36 G. Kresse and D. Joubert, *Phys. Rev. B*, 1999, **59**, 1758–1775.

37 H. J. Monkhorst and J. D. Pack, *Phys. Rev. B*, 1976, **13**, 5188–5192.

38 G. Makov and M. Payne, *Phys. Rev. B*, 1995, **51**, 4014–4022.

39 Y. Zhang and W. Yang, *Phys. Rev. Lett.*, 1998, **80**, 890–890.

40 S. Grimme, J. Antony, S. Ehrlich and H. Krieg, *J. Chem. Phys.*, 2010, **132**, 154104.

41 S. Grimme, S. Ehrlich and L. Goerigk, *J. Comput. Chem.*, 2011, **32**, 1456–65.

42 L. Goerigk and S. Grimme, *Phys. Chem. Chem. Phys.*, 2011, **13**, 6670–88.

43 M. Birgersson, C.-O. Almbladh, M. Borg and J. Andersen, *Phys. Rev. B*, 2003, **67**, 045402.

44 N. V. Belova, V. V. Sliznev, H. Oberhammer and G. V. Girichev, *J. Mol. Struct.*, 2010, **978**, 282–293.

45 N. V. Belova, H. Oberhammer and G. V. Girichev, *J. Phys. Chem. A*, 2004, **108**, 3593–3597.

46 M. M. Schiavoni, H. E. Di Loreto, A. Hermann, H. G. Mack, S. E. Ulic and C. O. Della Vdova, *J. Raman Spectrosc.*, 2001, **32**, 319–329.

47 H. A. Shallard-Brown, D. J. Watkin and A. R. Cowley, *Acta Crystallogr. Sect. E*, 2005, **61**, o2422–o2423.

48 C.-L. Liu and J. B. Adams, *Surf. Sci.*, 1992, **265**, 262–272.

49 K.-H. Ernst, *Phys. Status Solidi*, 2012, **249**, 2057–2088.

50 S. S. Tafreshi, A. Roldan, N. Y. Dzade and N. H. de Leeuw, *Surf. Sci.*, 2014, **622**, 1–8.

51 M. F. Haroun, P. S. Moussounda and P. Légaré, *Catal. Today*, 2008, **138**, 77–83.

52 T. P. Pearl and S. J. Sibener, *J. Phys. Chem. B*, 2001, **105**, 6300–6306.

# 4 Electronic structure of Pd multi-layers deposited on Re(0001) surface

This Chapter describes the structure and electronic behavior of few-layer palladium films on the rhenium (0001) surface; a heteroepitaxial system that exhibits negligible strain and, therefore, the so-called *ligand effects* can be isolated. Based on the comparison of experimental and simulated X-ray photoelectron spectra, and the calculation of the valence electron structure, we establish a general analogy between charge transfer and strain effects in bimetallic interfaces. Most of the work presented in this Chapter is part of a paper published in *Journal Physical Chemistry C*.[1] The final part about interaction with oxygen is still unpublished.

## 4.1 INTRODUCTION

The heterogeneous catalytic activity of multi-metallic systems continues to provide a rich landscape of opportunity in tuning catalytic reaction pathways. By mixing metals to form alloys or composites, new material properties can evolve that can significantly impact performance. A typical case is the synthesis of core-shell nanoparticles in which a reactive outer skin (often a precious metal) is supported on a core metal (often a cheaper base metal), or as a model system, in the form of a thin metal film supported on another metal. With only a few atomic layers of precious metal, it is commonly found that the surface chemical properties are different to that of the bulk metal surface.[2,3] The prediction and rational design of these properties has required the development of models of adsorption and reactivity whereby intimate knowledge of the surface electronic structure becomes essential. Thus, a great deal of theoretical and computational work has been devoted to the understanding of these interfaces.[4,5]

The modification of the electronic behavior of metal thin films by the support is produced via a combination of *strain* and *ligand effects*. The former arise because, in a supported heterogeneous overlayer system, the nearest-neighbor spacing of atoms in the epitaxial layer are unlikely to match those of the bulk of the metal, hence the change in interatomic distances modifies the intra-layer interactions. On the other hand, "ligand effects" are those arising due to the direct interactions between heteroatoms in the system, modifying the electronic structure near the interface. Both types of effects for metal adlayers have been discussed in the context of the very successful *d*-band model proposed by Hammer, Nørskov and collaborators.[6] It has been theoretically shown that, for a wide variety of heteroepitaxial systems, the presence of the support leads to a modification of the *d*-band width of the adlayer, and in turn influences the average energy of the *d*-band, which rigidly shifts to maintain a constant filling.[7]

The effect of strain on the bandwidth is simple to understand: when the lattice expands parallel to the surface (tensile strain) the overlap between the *d* orbitals on neighboring atoms within the adlayer becomes smaller, which leads to less band dispersion and narrower bandwidth. Conversely, lattice contraction due to lateral compressive strain leads to wider bands. There has been abundant discussion of the strain effect in the theoretical literature since density functional theory (DFT) calculations by Mavrikakis *et al*. showed that the adsorption energies of atomic oxygen and molecular CO correlated with the shift of the *d*-band center produced by strain on the Ru(0001) surface, and successfully explained it by the bandwidth mechanism.[8] Experimentally, it has been observed that the adsorption behavior and the catalytic activity for formic acid electro-oxidation of a palladium monolayer supported on various other metal surfaces, vary systematically with lateral compression or expansion as predicted by the *d*-band width/shift model.[9]

On the other hand, the precise nature of ligand effects for metal adlayers is slightly more elusive, probably because strain and ligand effects are very difficult to separate in practice. In order to isolate the ligand effects, Kitchin *et al*. performed a DFT study of unstrained Pt adlayers on (strained) metallic supports, and found that the *d*-band width/shift model can still be used to explain the modification of the electronic structure of the adlayer by the support.[10] The proposed mechanism is that the electronic interactions between the Pt adatoms and the subsurface metal atoms modify the matrix elements between the corresponding *d*-orbitals, leading to a change in the bandwidth. They pointed out that, within a tight-binding formalism, the bandwidth is proportional to the matrix elements between the *d*-orbitals, which depend both on the nature of the two metals and the interatomic separations. In the context of metal adlayers on metal supports, these matrix elements are expected to characterize the "strength" of the interaction between the adlayer and the support.

We will argue here that, at least for the particular system under study, the direct interaction between the adlayers and the support can be more simply described as charge transfer. Surprisingly, the role of charge transfer has been widely neglected in the literature on bimetallic systems, despite the fact that charge transfer should always be expected at the interface of metals with different workfunctions. The surface with the higher workfunction should receive electrons at the interface, which can be explained from the alignment of the band structure of the two separate metals with respect to the vacuum reference level: the Fermi level of the higher-workfunction metal will lie lower than that of the other, and therefore electronic equilibrium requires electron transfer to the metal with the higher workfunction, until the created interface dipole prevents further charge transfer.[11] The main reason why the role of charge transfer has been overlooked in this context is probably the success of the *d*-band model in explaining the electronic properties of metal adlayers, since the model assumes a constant filling of (and therefore no charge transfer to or from) the adlayer *d*-band. Another reason is some conflicting predictions made by simple charge transfer models about the core-level shifts observed in experiment, as discussed further below.

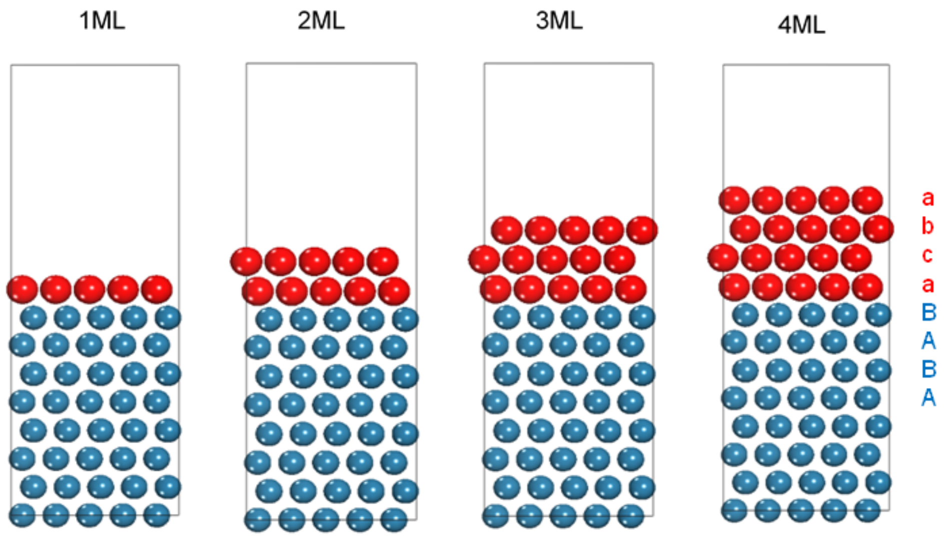

**Figure 4.1** Schematic representation of stacked Pd/Re(0001) system. The stacking sequence shown here corresponds to the lowest-energy configuration in each case. Key: red = Pd, and blue = Re.

In order to focus on the direct support-adlayer interactions and exclude strain, we have studied an heteroepitaxial system where the lattice parameter of the adlayer is practically the same as that of the support: the Pd/Re(0001) system. Furthermore, by considering Pd adsorption beyond the single monolayer (ML), one can also investigate as a reference the electronic properties of consecutive layers where there is no direct interaction with the support at all. In recent experimental work from our group, Etman *et al.*[12] fully characterized the systems formed by 1-4 ML of Pd on Re(0001), using quantitative low energy electron diffraction (LEED-IV), scanning tunneling microscopy (STM) and X-Ray photoelectron spectroscopy (XPS). The LEED experiment identified the stacking sequence of the Pd layers. If the Re stacking of (0001) planes is denoted as ABAB (the *hcp* sequence), then the first layer of Pd continues the *hcp* sequence, so the deposited monolayer (1ML) can be denoted as ABABa. However, consecutive layers of Pd follow the *fcc* sequence, leading to the ABABac structure for 2ML, ABABacb for 3ML, and ABABacba for 4ML (**Figure 4.1**). The XPS spectrum in that study was measured using an unmonochromated X-ray source, which offered low resolution compared with synchrotron radiation. Therefore only one broad peak was found, which shifted systematically to lower binding energies as more Pd was deposited, until a point (between 2 and 3 ML deposition) from where the position of the peak remained constant. A previous study of the same system by Mun *et al.*[13] reported high-resolution XPS spectra using synchrotron radiation, where a separate peak with higher core-level binding energy could be resolved and assigned to the interface Pd layer, on the basis of its attenuation upon increasing Pd deposition. In order to resolve the apparent contradiction between higher binding energies of Pd core levels at the interface (which would be typically interpreted as electron charge depletion) and a measured lowering of the valence band center of these atoms away from the Fermi level (which indicates electron gain), these authors invoked a charge redistribution picture from the theoretical work by Wu and Freeman,[14] according to which, the interaction between Pd and Re atoms at the interface results in *i*) charge accumulation in the interfacial region on top of the Re atoms and *ii*) charge depletion from both Pd and Re atoms. Our investigation provides a different picture that disputes both the charge transfer model presented in Ref. 14 and its interpretation in Ref. 13. A simple charge transfer model can actually explain the experimental observations of the behavior of the core and valence levels in the Pd/Re(0001) system.

## 4.2 COMPUTATIONAL METHODS

Periodic DFT calculations were performed with the VASP program[15,16] using the Perdew-Burke-Ernzerhof (PBE) exchange-correlation functional.[17] The projected augmented wave (PAW)[18,19] method was used to describe the interaction between the valence electrons and the core. The number of planewaves was determined by a kinetic energy cutoff of 327 eV (set at 30% above the default value from PAW potentials in order to minimize Pulay errors).[20] The Re(0001) surface was modeled with a periodic slab consisting of 8 layers, and a vacuum space of 20 Å. Only the four uppermost Re layers were fully relaxed, while the four bottom layers were fixed in the bulk positions. Of course, the positions of the deposited Pd-layers were also allowed to fully relax. In order to compensate for the use of an asymmetric slab, all simulations included a dipole correction as implemented in VASP, based on a method proposed by Makov and Payne.[21] Monkhorst-Pack grids[22] with a maximum separation of 0.15 $Å^{-1}$ between **k**-points were used for sampling the Brillouin-zone. This grid density, which was checked with respect to convergence of the Re bulk total energy, corresponds to a 18×18×1 grid for the reciprocal space of the slab model. Ionic positions were relaxed using a conjugate gradient algorithm until the forces on atoms were all less than 0.01 $eVÅ^{-1}$.

For bulk Re, the calculated unit cell parameters are $a$ = 2.770 Å and $c$ = 4.475 Å, which compare well with experimental values $a_{\mathrm{exp}}$ = 2.761 Å and $c_{\mathrm{exp}}$ = 4.458 Å (deviations of +0.3% and +0.4%). For bulk Pd, the calculated unit cell parameter is $a$ = 3.935 Å, which is reasonable compared to the experimental value $a_{\mathrm{exp}}$ = 3.890 Å (deviation of +1.2%).[23] In both cases, the positive deviations are as expected from the well-known overestimation of metal lattice parameters by generalized gradient approximation (GGA) methods.[24] The corresponding surface lattice parameters for Re(0001) (2.770 Å) and Pd(111) (2.782 Å) are thus very similar, giving only a very small compressive strain (-0.4%). Using experimental surface cell parameters (2.761 Å for Re(0001) and 2.751 Å for Pd(111)), the strain is actually positive (tensile) but also very small: +0.4%. As showed below, this small discrepancy with experiment does not affect the agreement between theory and experiment in terms of the electronic structure of the films, confirming that the effect of strain is negligible for this interface.

The formation energy (per surface site) of the interface with *n* Pd layers was calculated as:

$$\Delta E_{\mathrm{f}} = E_{\mathrm{Pd/Re}} - (E_{\mathrm{Re}} + nE_{\mathrm{Pd}}) \tag{4.1}$$

where $E_{\mathrm{Pd/Re}}$ represents the energy of the optimized Pd-Re system, $E_{\mathrm{Re}}$ corresponds to the energy of the relaxed clean Re surface, and $E_{\mathrm{Pd}}$ denotes the energy per atom of Pd bulk. The transferred charge density $\Delta\rho$ was calculated by subtracting, from the charge density of the Pd-Re system, the sum of the charge densities of the clean Re surface and Pd layers (calculated at the same geometry which they have at the interface):

$$\Delta\rho = \rho_{\mathrm{Pd/Re}} - (\rho_{\mathrm{Re}} + \rho_{\mathrm{Pd}}) \tag{4.2}$$

Effective atomic charges were computed using the Bader methodology,[25] where the three-dimensional space is partitioned into basins, (typically) belonging to individual atoms, delimited by surfaces through which the flux of the density gradient is zero. For the Bader analysis we used the implementation by Henkelman *et al.*[26–28]

Core-level binding energy shifts $\Delta\mathrm{BE}_{\mathrm{CL}}$ of the Pd 3*d* levels were obtained in the so-called final-state approximation,[29] as described in Chapter 2. Such values were then used to simulate XPS spectra to allow visual comparison with experimental data.

The valence *d*-band properties were calculated as follows: the position of the band center ($E_d$) is obtained from the first moment of the *d*-projected density of states ($g_d(E)$) with respect to the Fermi level ($E_F$):

$$E_{\mathrm{d}} - E_{\mathrm{F}} = \frac{\int_{-\infty}^{\infty} g_{\mathrm{d}}(E)(E - E_{\mathrm{F}})dE}{\int_{-\infty}^{\infty} g_{\mathrm{d}}(E)dE} \tag{4.3}$$

the root-mean-squared width $W_{\mathrm{d}}$ of the *d*-band is obtained from the second moment of the density of states (DOS) with respect to the band center:

$$W_{\mathrm{d}}^2 = \frac{\int_{-\infty}^{\infty} g_{\mathrm{d}}(E)(E - E_{\mathrm{d}})^2 \mathrm{d}E}{\int_{-\infty}^{\infty} g_{\mathrm{d}}(E)\mathrm{d}E} \tag{4.4}$$

and the *d*-band filling is calculated as:

$$f_{\mathrm{d}} = \frac{\int_{-\infty}^{E_{\mathrm{F}}} g_{\mathrm{d}}(E)\mathrm{d}E}{\int_{-\infty}^{\infty} g_{\mathrm{d}}(E)\mathrm{d}E} \times 100\% \tag{4.5}$$

Finally, the dissociative adsorption energy $E_{\mathrm{ads}}$ of oxygen was calculated as:

$$E_{\mathrm{ads}} = E_{\mathrm{slab+O}} - E_{\mathrm{slab}} - \frac{1}{2} E_{\mathrm{O_2}} \tag{4.6}$$

where $E_{\mathrm{slab+O}}$ is the energy of the optimized substrate–adsorbate system, $E_{\mathrm{slab}}$ corresponds to the energy of the relaxed clean surfaces, and $E_{\mathrm{O_2}}$ is the energy of oxygen in the gas phase.

## 4.3 RESULTS AND DISCUSSION

### 4.3.1 Interface geometry and stability

The calculated formation energies for the different possible stacking sequences, as reported by Etman *et al.*,[12] are summarized in **Table 4.1**. There is a perfect match between the lowest-energy stacking configuration and the one with the lowest Pendry factor ($R_{\mathrm{p}}$), which corresponds to the best structural fit to the LEED data in Ref. 12. Therefore, DFT simulations confirm the preferred growth suggested by experiment, in which the first layer adopts an *hcp* pseudomorphic structure ABABa; the second layer introduces a stacking fault to give a *fcc*-like termination ABABac, with subsequent layers growing in an *fcc* pattern. The fact that the experimental configuration corresponds in each case to the one with the lowest energy suggests that the stacking sequence of the Pd films is thermodynamically controlled during growth.

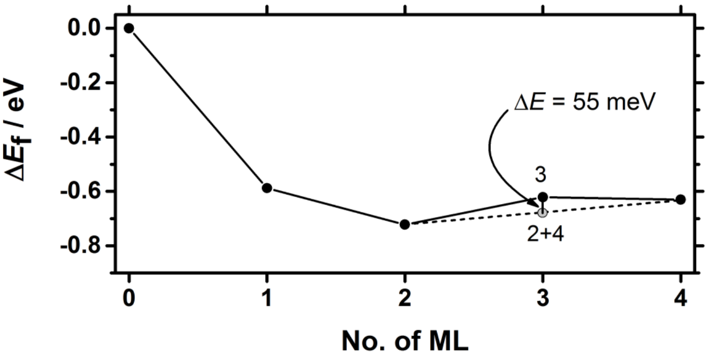

**Figure 4.2** Interface formation energy (energy is relative to free Re surface and Pd bulk) as a function of Pd coverage. Straight lines joining the points are a guide to the eye.

The plot in **Figure 4.2** displays the formation energy of the preferred stacking configurations at each composition against the number of deposited layers. The negative values indicate that the deposition is an energetically favorable process with respect to Pd atoms in the bulk and the free Re surface. DFT calculations predict a shallow minimum of the interface formation energy at 2ML Pd. From the shape (convex hull) of the variation of the formation energy with the number of deposited layers, the homogeneous 3ML composition is thermodynamically unstable (by 55 meV per surface unit cell) with respect to separation into islands of 2ML and 4ML, ignoring border contributions. However such separation is not observed in the experiment, where the 3ML system was found to be homogeneous and fit well a model with ABABacb sequence. Therefore, DFT modeling suggest that the separation of the homogeneous system into a heterogeneous system with islands of different thicknesses might be kinetically limited under the conditions of these experiments, even when the stacking follows the thermodynamically preferred sequence.

**Table 4.1** Formation energies for the different possible stacking sequences. ABAB represents the *hcp* sequence of Re layers. Lowercase letters indicate the relative stacking of the Pd layers. LEED results are from Ref. 12. Underlined/bold entries represent the lowest DFT energy or best experimental fit.

| No. of ML | Stacking | $\Delta E_f$ (eV) | LEED $R_p$ factor |
|---|---|---|---|
| 1 | **ABABa** | **-0.588** | **0.218** |
| | ABABc | -0.527 | 0.465 |
| 2 | ABABab | -0.698 | 0.351 |
| | **ABABac** | **-0.722** | **0.211** |
| | ABABca | -0.593 | 0.268 |
| | ABABcb | -0.570 | 0.386 |
| 3 | ABABaba | -0.597 | 0.419 |
| | ABABabc | -0.617 | 0.284 |
| | ABABaca | -0.603 | 0.404 |
| | **ABABacb** | **-0.621** | **0.248** |
| | ABABcab | -0.521 | 0.275 |
| | ABABcac | -0.509 | 0.396 |
| | ABABcba | -0.496 | 0.303 |
| | ABABcbc | -0.479 | 0.420 |
| 4 | ABABacab | -0.607 | 0.288 |
| | ABABacac | -0.587 | 0.475 |
| | **ABABacba** | **-0.630** | **0.209** |
| | ABABacbc | -0.612 | 0.446 |

The optimized interlayer distances for the slabs are summarized in **Table 4.2**. The DFT values of the interlayer distances are also consistent with LEED measurements, with good quantitative agreement within the experimental error in most cases. The small contraction of the Pd-Re interface, with respect to Pd-Pd distances, could be a consequence of charge transfer at the interface, which will be discussed later.

**Table 4.2** Calculated interlayer distances in comparison with experiment.[12] The italicized/bold entries correspond to the Re-Pd interface.

| **Interlayer separation** | **1ML** | | **2ML** | | **3ML** | | **4ML** | |
|---|---|---|---|---|---|---|---|---|
| | DFT | Exp. | DFT | Exp. | DFT | Exp. | DFT | Exp. |
| **$d_{12}$ (Å)** | ***2.23*** | ***2.20±0.05*** | 2.32 | 2.30±0.04 | 2.31 | 2.34±0.04 | 2.31 | 2.30±0.03 |
| **$d_{23}$ (Å)** | 2.16 | 2.18±0.03 | ***2.20*** | ***2.23±0.03*** | 2.33 | 2.29±0.04 | 2.30 | 2.28±0.03 |
| **$d_{34}$ (Å)** | 2.29 | 2.25±0.04 | 2.17 | 2.19±0.07 | ***2.22*** | ***2.28±0.07*** | 2.34 | 2.30±0.05 |
| **$d_{45}$ (Å)** | 2.21 | 2.23±0.06 | 2.29 | 2.30±0.07 | 2.17 | 2.17±0.13 | ***2.22*** | ***2.30±0.06*** |

### 4.3.2 Charge transfer at the interface

In order to understand the nature of the interaction between the substrate and the Pd thin-films, as well as the electronic structure presented below, we now discuss the occurrence and magnitude of the charge transfer at the interface. **Figure 4.3** shows a cross-section plot of the transferred charge density $\Delta\rho$, as given by **Equation 4.2**, for the case of 1 ML Pd on Re(0001). There is a clear charge transfer of electrons from Re to Pd. The transferred charge is polarized in such a way that it is mostly located “below”, i.e. at the side pointing towards the Re support. We checked that this asymmetry of the transferred charge distribution is not a consequence of the choice of the projection plane.

Therefore, we disagree here with the conclusion from the theoretical work of Wu and Freeman[14] on the 1ML Pd/Re(0001) system, where they state that the interaction between Pd and Re results in charge accumulation in the interfacial region, with electron depletion from *both* Pd and Re atoms. Our conclusion that Pd is instead a net receiver of negative charge is supported by the Bader analysis of the DFT charge density depicted in **Table 4.3**, which shows that in the case of 1 ML deposition, the Pd atoms adopt an effective charge of -0.18 *e*, while the top Re atoms adopt a positive charge of +0.15 *e*, with an additional small amount of positive charge (+0.03 *e*) in the second Re layer. In the case of multi-layer Pd deposition, Pd layer at the interface always contains most of the negative charge, although in the case of 2ML deposition the negative charge at the second Pd layer is also significant (-0.07 *e*). The top Re layer accounts for most of the positive charge in all cases, and the total amount of transferred charge is practically independent on the number of Pd layers deposited.

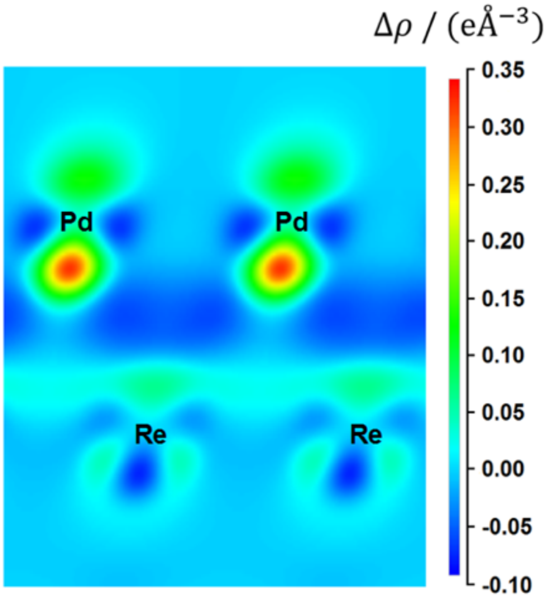

**Figure 4.3** Contour plot of the transferred charge density for the system with 1 ML Pd on Re(0001). The plane of the figure was chosen in such a way that the cross-section contains both Pd atoms and Re atoms at the interface.

The charge transfer direction from Re to Pd at the interface is as expected on the basis of the relative workfunction of Re compared to Pd: the computed workfunction values for the Re(0001) and Pd(111) surfaces are 4.91 eV and 5.27 eV, respectively (values of 4.72 eV and 5.22 eV are reported from experiment for polycrystalline Re and Pd).[30] As explained above, the surface with the higher workfunction is expected to receive electrons at the interface, which can be explained from the alignment of the electron bands of the two separate metals with respect to the vacuum reference level.[11]

**Table 4.3** Bader analysis for the clean Re(0001) and the interfaces with Pd thin films of different thicknesses.

| Atoms | clean | 1ML | 2ML | 3ML | 4ML |
|---|---|---|---|---|---|
| Pd | - | - | - | - | -0.03 |
| Pd | - | - | - | -0.03 | 0.03 |
| Pd | - | - | -0.07 | -0.01 | -0.04 |
| Pd | - | -0.18 | -0.10 | -0.12 | -0.12 |
| Re | -0.07 | 0.15 | 0.14 | 0.14 | 0.14 |
| Re | 0.06 | 0.03 | 0.03 | 0.03 | 0.03 |
| Re | 0.00 | 0.00 | 0.00 | 0.00 | 0.00 |
| Re | 0.01 | 0.00 | 0.00 | 0.00 | 0.00 |

### 4.3.3 Core-level shifts and simulated XPS spectra

The simulated XPS spectra was obtained by calculating final-state Pd 3*d* core-level shifts using DFT. Gaussian curves were used for broadening the contribution from each layer; their intensities are given by an exponential attenuation with the distance to the surface afforded for the inelastic mean free paths, while their widths are determined by the resolution of the experiment being simulated (**Figure 4.4a**). The solid curves in **Figure 4.4a** correspond to the simulation of laboratory-based XPS data such as that shown in **Figure 4.4b**, which is reproduced here from Ref. 12. The dashed curves correspond to the simulation of high-resolution synchrotron XPS, where separate peaks are resolved; this can be compared with the experimental results presented in Ref. 13.

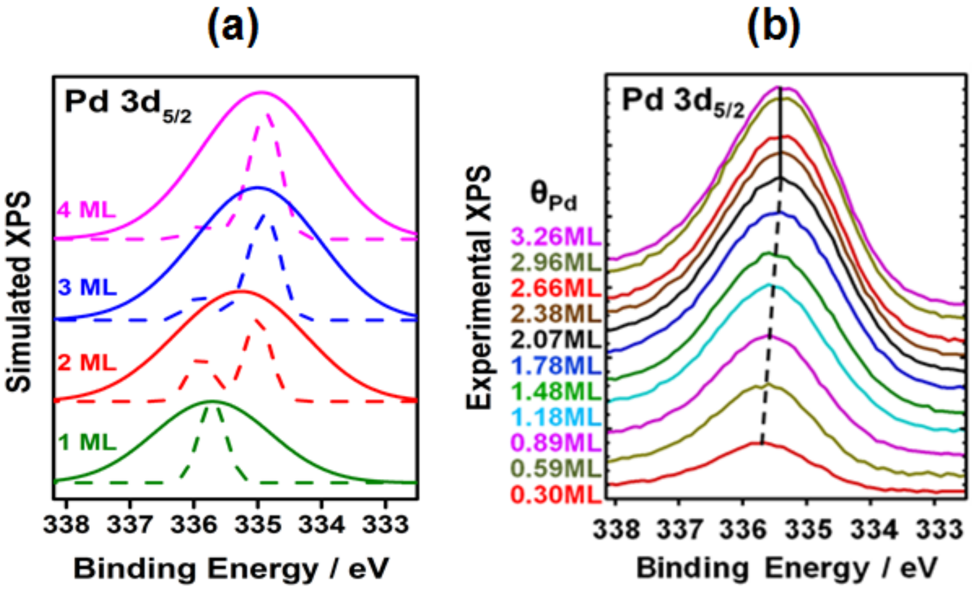

**Figure 4.4** XPS spectra as a function of Pd coverage on the Re (0001) surface: (a) DFT simulation, where solid and dashed lines represent low-resolution and high-resolution spectra, respectively; (b) Low-resolution XPS obtained with photon energy of 1486.6 eV, reproduced from Ref. 12. The high resolution simulation is based upon the experimental conditions of Ref. 13 where a photon energy of 450 eV was employed.

The basic features of both low-resolution and high-resolution XPS experiments are well reproduced by the DFT-simulated XPS spectra. The low-resolution peaks initially shift to lower binding energies (BE) with increasing Pd coverage, and then remain constant after 2-3 ML deposition. High-resolution signals split into two peaks; the one with the higher BE decreases its relative intensity with increasing Pd coverage.

The XPS simulation permits to unambiguously determine the origin of the different contributions to the spectrum. In the high-resolution spectrum, we confirm the assignment of the higher BE peak to the contribution from Pd atoms at the interface, as originally proposed by Mun *et al.*[13] The lowest BE contributions arise from the surface Pd atoms, which are similar to the BE from the bulk-like layers in between. Even the synchrotron-radiation XPS cannot clearly resolve these two types of contributions (surface and "bulk" of the film), and therefore they visually appear as a single peak (figure 1 in Ref. 13), although the authors mention that fitting the spectrum does indicate the presence of a "surface" peak shifted by 0.3 eV with respect to bulk peaks. In the calculations for the 4ML system, we found that the binding energy difference between the surface layer and the average of the two bulk-like layers is 0.26 eV, in good agreement with their fitting result.

The higher BE of the core levels of the interface Pd atoms has to be reconciled with our previous conclusion about the transferred charge localization on these atoms. In the analysis of core-level shifts, a higher BE is often associated with a more positive ion, which is rationalized by the stronger Coulomb attraction between a more positive ion and the electron being ejected. However, spectroscopic analysis clearly shows a shift to higher BE for the more negative Pd ion at the interface. In fact, the commonly used association between shift to higher BE and electron depletion, which our results contravene, is now known to be generally inadequate, in particular for interpreting core level shift in surface adlayers.[31] The correct explanation for the sign of the core level shifts will be discussed below, on the basis of the behavior of the valence electronic structure of this system.

### 4.3.4 Valence electron density of states and *d*-band centers

We have calculated the electronic density of states (DOS) projected on the 4*d* valence orbitals of Pd atoms, layer by layer. The results for the surface and interface layers are shown in **Figure 4.5a**. It is clear that the *d*-band center for the interface Pd atoms (dashed lines) is shifting to lower values, away from the Fermi level, compared to the *d*-band center of surface Pd atoms. On the other hand, **Figure 4.5b** shows that for all Pd atoms in the films, a shift in the 4*d* valence level corresponds to a shift in the same direction and of similar value as that of the 3*d* core level. This remains true regardless of whether we use initial-state or final-state core-level shifts (correlation $R^2 > 0.95$ in both cases). The gradients of the linear fit lines are 1.09 (initial-state shifts) and 1.16 (final-state shifts); the proximity to 1 indicates that there are nearly rigid shifts of the core and valence levels with respect to the Fermi level.

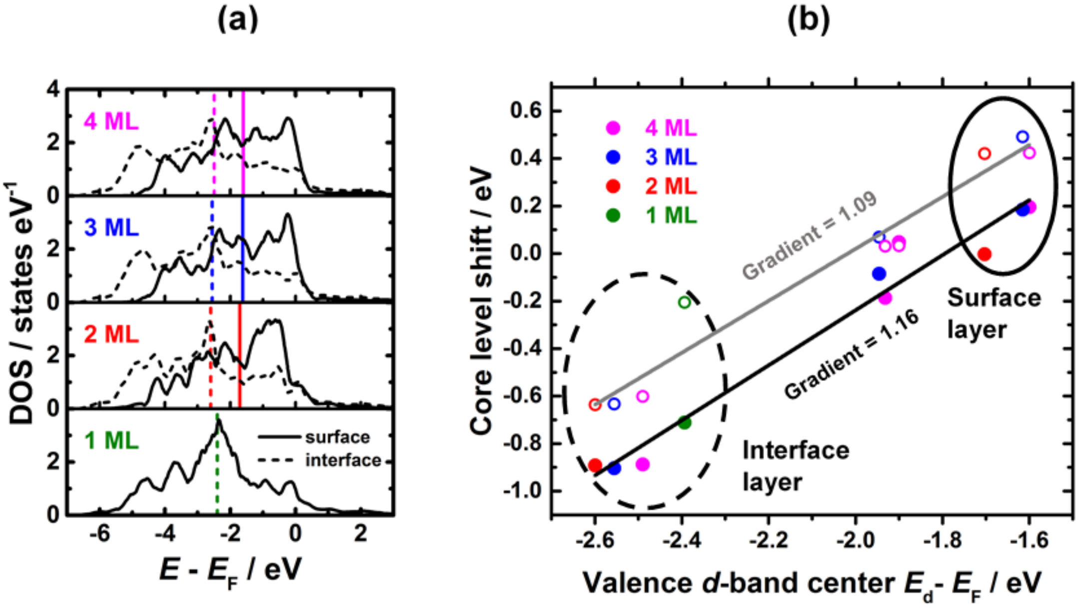

**Figure 4.5** (a) Electronic density of states (DOS) projected on the Pd 4*d* orbitals of the surface (solid lines) and interface (dashed lines) atoms, with the corresponding *d*-band centers marked by vertical bars. (b) Correlation between Pd 3*d* core-level shifts and Pd 4*d* band centers. The initial-state and final-state shifts are shown with empty and filled circles, while the corresponding best-fit lines and their gradients are shown in gray and black, respectively.

The similarity between the results using initial-state and final-state shifts in **Figure 4.5b** implies that initial state effects dominate the binding energies. The shift of the core levels should be seen as a consequence of a change in the electronic structure of the valence, and therefore as an initial-state effect arising through the shift in the entire local potential at the sites. The correlation between core and valence level shifts of metal surfaces and adlayers has been discussed before by several authors.[31–34] This correlation is important from a practical point of view because it implies that XPS measurements of core level shifts carry value as experimental predictors of surface adsorption and reactivity behavior, in the same way as the *d*-band shifts are useful theoretical predictors of these properties. The XPS technique is well established and commonly used to characterize catalyst materials and hence this experimental descriptor constitutes a very practical choice, as was noted in an early study by Rodriguez and Goodman.[35]

**Table 4.4** Layer by layer *d*-band filling and electron population of the *s*, *p* and *d* valence bands as obtained from the integration of the projected densities (within PAW spheres) of states up to the Fermi level. The values corresponding to the interface Pd layer are highlighted with italics/bold font.

| **System** | **Pd layer (from top)** | ***d*-band filling $f_d$** | **Electron population** | | |
|---|---|---|---|---|---|
| | | | ***s*** | ***p*** | ***d*** |
| **1ML** | 1 | ***93%*** | ***0.51*** | ***0.40*** | ***8.52*** |
| **2ML** | 1 | 93% | 0.47 | 0.32 | 8.49 |
| | 2 | ***91%*** | ***0.51*** | ***0.54*** | ***8.45*** |
| **3ML** | 1 | 92% | 0.45 | 0.32 | 8.49 |
| | 2 | 91% | 0.47 | 0.43 | 8.46 |
| | 3 | ***90%*** | ***0.52*** | ***0.53*** | ***8.45*** |
| **4ML** | 1 | 91% | 0.45 | 0.33 | 8.48 |
| | 2 | 90% | 0.46 | 0.44 | 8.44 |
| | 3 | 90% | 0.47 | 0.43 | 8.46 |
| | 4 | ***90%*** | ***0.52*** | ***0.53*** | ***8.45*** |

However, what is more interesting from our results, and in contrast to previous work, is the discussion of the mechanism causing the valence *d*-band shift in the first place. In strained metallic adlayers, it is customary to explain this behavior via the "bandwidth mechanism", which is illustrated in **Figure 4.6a**. In the presence of tensile strain, the metal atoms are laterally more separated in the adlayer, which leads to a decrease in the *d*-band width. If one assumes no charge transfer to the *d*-band, the narrowing of the (more than half-filled) band is necessarily accompanied by a shift upward of its center, towards the Fermi level, in order to preserve band filling. Conversely, in the presence of compressive strain, the width of *d*-band will increase and its center will shift down, away from the Fermi level.[5] Clearly, in our case this mechanism has to be rethought because a) the strain in the Pd adlayers on Re(0001) is negligible, and b) it has been shown that there is significant charge transfer at the interface.

**Table 4.4** shows that, for any given composition, all Pd layers have a similar degree of *d*-band filling ($f_d$), despite the differences in charge identified above using Bader analysis. Even for different compositions, the degree of band filling is very similar in all cases (between 90 and 93%), decreasing only slightly with the thickness of the layer. The reason why the charge transferred to the Pd layer at the interface is not going to states of *d* character is that the polarization of the transferred charge, which is illustrated in **Figure 4.3**, is not compatible with the symmetry of the *d* orbitals. Instead, a hybrid of valence *s* and *p* orbitals is a more appropriate description, due to constructive interference between the mixing orbitals on one of the *p* lobes (the one pointing towards the interface) and destructive interference in the opposite one. The electron population decomposition analysis (integration of *s, p, d* - projected charges within PAW spheres) in **Table 4.4** shows that, indeed, there is always significant increase in the *s-p* population of the interface Pd compared to the other layers. It should be noted here that the total charge differences obtained from integration within atomic spheres are similar to those identified using Bader analysis (defined for non-spherical atomic basins), which confirms that our conclusions about the presence and magnitude of charge transfer are valid regardless of the definition of the atomic regions.

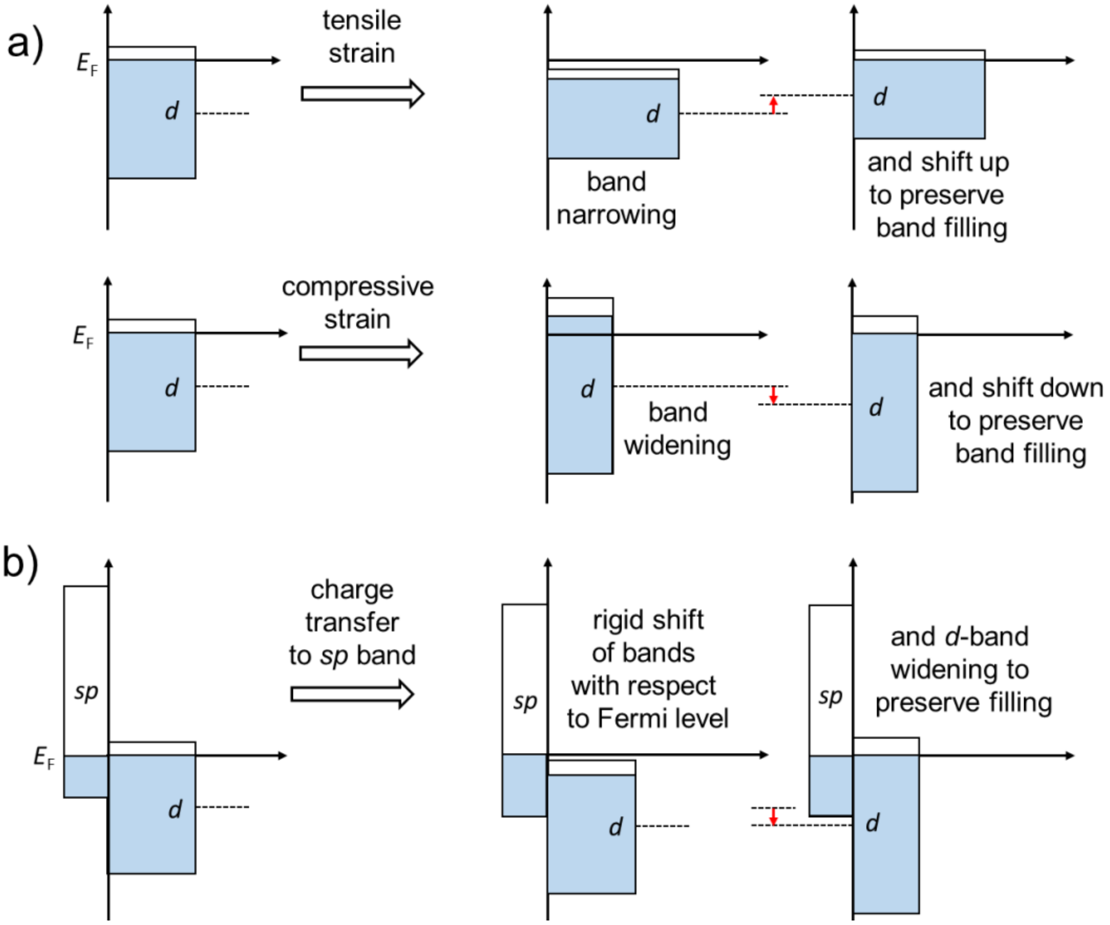

**Figure 4.6** Origin of the valence *d*-band shift (a) in the presence of tensile or compressive strain but absence of charge transfer, and (b) when there is no strain but instead there is charge transfer to the adlayer *sp* valence levels, as in the case of Pd/Re(0001).

Since the filling of the *d*-band is roughly constant for each composition, the inverse correlation between the valence *d*-band width and the *d*-band center shift, which is expected for strained systems, is also observed in this system (**Figure 4.7**). The relative displacement of the lines for different compositions is reflecting the slightly different band filling degrees. The inverse correlation between bandwidth and band center shift simply indicates a constant degree of *d*-band filling, regardless of whether the shift is induced by strain or by charge transfer to the *s-p* band. But whereas in the strain case the bandwidth change is a direct consequence of strain, and the center shift results from the bandwidth change, in our charge-transfer picture the bandwidth change is not driving the band center shift, but it is a consequence of it.

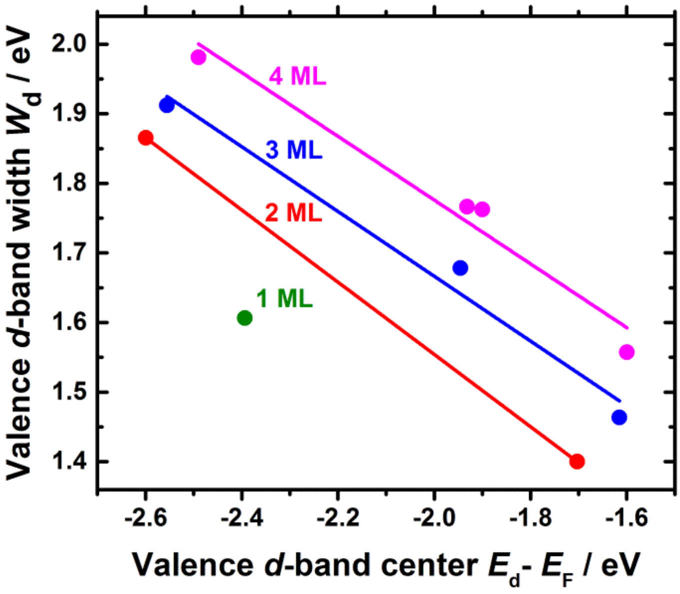

**Figure 4.7** Correlation between the width of the Pd valence *d*-band and the position of its center with respect to the Fermi level.

To illustrate the above point, the simplified scheme in **Figure 4.6b** shows the effect of charge transfer to *s-p* levels on the position and width of the *d*-band. The key here is that all valence (and also core) levels shift almost rigidly with changes of the site potential. Thus, the filling of the *s-p* band due to interfacial charge transfer is accompanied by a down shift of the *d*-band center with respect to the Fermi level. But since the filling of *d*-band center should remain constant, its width must increase to preserve the degree of filling.

Thus, our analysis shows that the behavior of the *d*-band in the Pd unstrained adlayer can be simply explained by charge transfer from the Re support, which can be seen as analogous to the application of support-induced compressive strain (which does not exist in this case). One could also expect that charge transfer in the opposite direction, i.e. electrons moving from the adlayer to the support (the obvious case to study here to exclude strain effects would be Re deposited on Pd(111)), is analogous to support-induced tensile strain.

It is likely that even in the case of strained interfaces, small amounts of charge transfer will contribute to the behavior of the metal *d*-band through the mechanism proposed here, which calls for a reexamination of the role of charge transfer in other (strained or not) metallic films on metal supports. For example, consider the case of only 1ML of Pd on Ru(0001), where a down-shift of core and valence levels has recently been reported experimentally and theoretically.[34] In this situation, there is significant compressive strain (-1.6% using experimental cell parameters). While the effect of strain can explain the direction of the shift, it is likely that its magnitude is also affected by charge transfer, as these two metals exhibit different workfunctions (the calculated value is 4.96 eV for Ru(0001), which is similar to that of Re(0001) and well below the value of 5.27 eV computed for Pd(111)). The Bader analysis in this case confirms that there is charge transfer to the Pd adlayer, of ~0.11 electrons per atom. Therefore, the shift in the valence and core levels in that case probably has contributions from both strain and charge transfer.

### 4.3.5 Energetics of dissociative adsorption of oxygen

The simplest surface process to characterize reactivity of these substrates is the dissociative adsorption of a homonuclear diatomic molecule. In this section, the adsorption of oxygen on clean Re(0001) and Pd/Re(0001) surfaces has been investigated. To account for the unpaired spins associated with oxygen species, spin-polarized calculations were performed. The plane wave kinetic energy cutoff was increased to 400 eV as required by the oxygen's PAW potential.

#### 4.3.5.1 Dissociative adsorption of oxygen on Re(0001) surface

Our exploration of sites for the dissociative adsorption of oxygen considered different coverages, down to $\Theta = 0.25$ ML (one oxygen atom per four heavy atoms). We only considered high-symmetry adsorption sites: *hcp* sites (an atom in the layer beneath the site) and *fcc* sites (no atom in the layer beneath), which are generally the preferable sites for oxygen adsorption in similar surfaces, e.g. *hcp* for Ru(0001)[36,37] and *fcc* for Pd(111)[38,39].

We first consider the results for the clean Re(0001) surface. The adsorption energies at different coverages are listed in **Table 4.5**. The adsorption energies range from -2.86 eV to -3.68 eV, indicating a highly exothermic process. Adsorption energies for *hcp* sites are more negative by around half an eV, meaning that the preferred site for the dissociative adsorption of $O_2$ in a Re(0001) surface is the *hcp* position, at any given coverage. We do not expect to find a mixed site occupation at finite temperatures since the difference in adsorption energy between both adsorption modes is significant. The preference found for the *hcp* sites on Re(0001) surface is consistent with theoretical results for other transition metals (TMs): oxygen is always found to occupy the sites that continue the bulk layer sequence (i.e., *fcc* on *fcc* Rh(111) and Ag(111), *hcp* on *hcp* Ru(0001)).[36,40,41] The preferential occupation of *hcp* sites over *fcc* sites can be attributed to the influence of the underlying layer beneath the *hcp* site. This influence remains the same at coverages below $\Theta = 0.5$ ML. However, at full coverage ($\Theta = 1$ ML), it is reduced by ~0.1 eV, still not enough to alter the site preference. Such a reduction at high coverages is possibly due to O-O interactions: even if the O-O distance is only a function of the coverage (and not of the adsorption site), the electronic structure of the O atoms might be affected differently by the adsorption at *hcp* and *fcc* sites, which in turn would change the nature of the O-O interactions.

**Table 4.5** Energetics of the oxygen adsorption on Re(0001) surface at different coverages (down to 0.25 ML). The adsorption energy difference, $\Delta E_{\text{ads}}$, is relative to the value for the respective *hcp* sites.

| Coverage | $E_{\text{ads}}$ (eV) | | |
|---|---|---|---|
| | *fcc* | *hcp* | $\Delta E_{\text{ads}}$ |
| 1 | -2.86 | -3.35 | -0.49 |
| 0.5 | -3.02 | -3.61 | -0.59 |
| 0.25 | -3.10 | -3.68 | -0.58 |

Indeed, the role of coverage is significant for adsorption at both sites in the range of coverages considered here. From the adsorption energy dependence as a function of coverages showed in **Figure 4.8**, it can be seen that the adsorption energy becomes less favorable with increasing coverage. The adsorption energy of oxygen on Re(0001) surface should become independent of coverage for very low coverage values. We did not consider that limit of isolated adsorption as it would require the use of very large supercells.

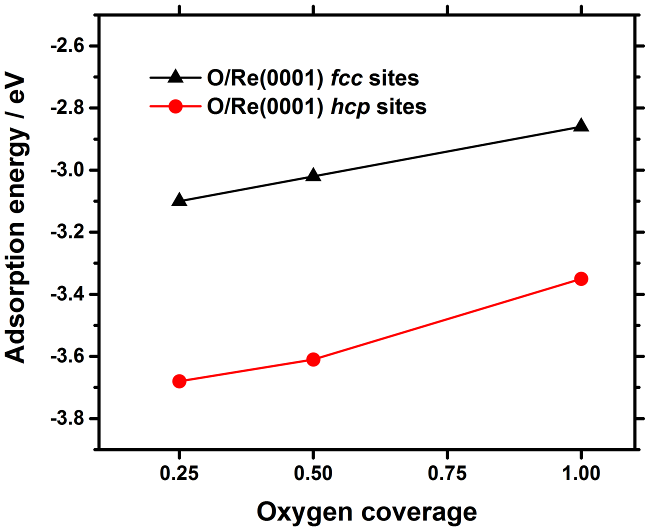

**Figure 4.8** Calculated adsorption energy as a function of oxygen coverage for the Re(0001) surface.

Note, however, that the dissociative adsorption of O in a clean Re(0001) surface in *hcp* sites is a highly exothermic process, regardless of the coverage. Thus, the high-coverage O adlayer structures are highly stable and may be able to form. In a similar system, O/Ru(0001), there is experimental evidence of a high-coverage (1×1) phase.[37] However, kinetic hindering of the dissociation of $O_2$ by an energy barrier is not discarded, at least for the high-coverage regime. Experimental evidence is required to corroborate this set of DFT simulations.

#### 4.3.5.2 Dissociative adsorption of oxygen on Pd/Re(0001) structures

For these systems, the simulations were performed at $\Theta = 0.5$ ML and $\Theta = 0.25$ ML coverages. Oxygen adsorption on Pd(111) is a well-studied system, both experimentally[38] and theoretically.[39] Experimentally, the process is dissociative and for a coverage of $\Theta = 0.25$ ML a (2×2) phase is formed, where the oxygen atoms occupy *fcc* hollow sites. It is reasonable then to consider only these two coverages.

**Table 4.6** Energetics of the oxygen adsorption on Pd/Re(0001) structures at two coverages and two different thickness of Pd. The adsorption energy difference, $\Delta E_{\text{ads}}$, is relative to the value for the respective *fcc* sites in this case.

| **Coverage** | **Pd Stacking** | $E_{\text{ads}}$ **(eV)** | | |
|---|---|---|---|---|
| | | *fcc* | *hcp* | $\Delta E_{\text{ads}}$ |
| 0.5 | ABABa | -0.52 | -0.49 | -0.03 |
| | ABABac | -0.83 | -0.64 | -0.19 |
| 0.25 | ABABa | -0.99 | -0.96 | -0.02 |
| | ABABac | -1.11 | -0.91 | -0.20 |

**Table 4.6** list the results obtained through simulations. At the coverage $\Theta = 0.5$ ML, the adsorption energies range from -0.49 to -0.83 eV, whereas at coverage $\Theta = 0.25$ ML they go from -0.91 to -1.11 eV. As reference, the difference in adsorption energy at the

same range of coverage is ~0.4 eV/atom in Pd(111) surfaces.[39] This reflects the repulsive adsorbate-adsorbate interactions with decreasing O-O distance in the adsorption of O on Pd atoms. At higher coverages, the O-O interactions should weaken the adsorption even more.

According to **Table 4.6**, the dissociative adsorption of O on monolayer Pd is only slightly more favorable on *fcc* sites than *hcp* sites, by ~0.02 eV. The preference for *fcc* sites is consistent with the trend observed for O adsorption on Pd(111) surfaces, where *fcc* sites were preferred over *hcp* sites, although by a larger energy margin, 0.2 eV.[39] The different behavior of the Pd monolayer on Re(0001) and the Pd(111) surface is likely to be connected with the significant charge transfer that takes place at the Pd/Re interface, which was discussed above: the Pd monolayer is more electron-rich than the top layer in Pd(111). The implication of this result is that in the 1ML Pd/Re(0001) system, a mix of oxygen adsorption sites can be expected. **Table 4.6** also shows that in the case of Pd bilayers supported on Re(0001), the *fcc* adsorption site is more stable than the *hcp* adsorption site, by ~0.2 eV (similar to the behavior in Pd(111)). In this case, the effect of the Re/Pd charge transfer on adsorption is small because most of the transferred electrons are localized at the Pd layer at the interface, while the top Pd layer, where O adsorption occurs, is now electronically similar to the top Pd layer in Pd(111).

#### 4.3.5.3 Comparison between clean Re(0001) and Pd/Re(0001) surfaces

Experimentally, the adsorption of oxygen on atomically-thin layers of Pd supported on Re(0001) leads to the “peeling off” of the Pd monolayers. **Figure 4.9** displays an STM image of the Pd/Re(0001) system after annealing, obtained by Bennett’s group at Reading. The bright spots indicate the presence of Pd islands, whereas the brown spots denote the Re support. After annealing, there is an increase of the areas where Re atoms are exposed.

Somehow the strength of adhesion between the Re support and the Pd adlayers is weakened.

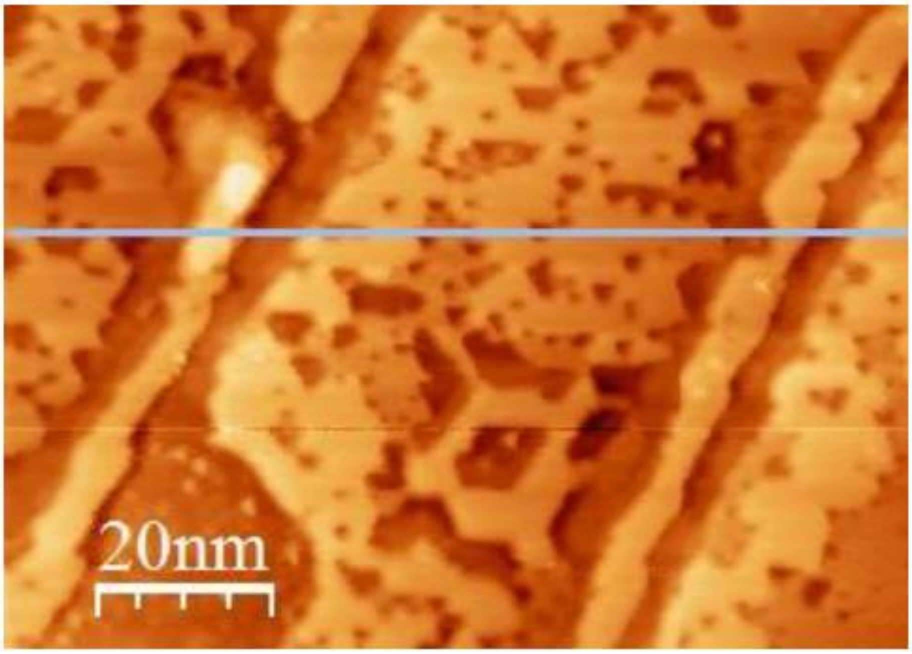

**Figure 4.9** STM image of few-layers Pd on Re(0001) annealed in oxygen surface (unpublished work by L. Richards and R.A. Bennett).

The DFT calculations provide a reasonable explanation of this feature in terms of thermodynamic preference. The interaction of O with Re support is very strong, featuring an adsorption energy of around -3.6 eV. In the other hand, the adsorption of oxygen in the Pd/Re(0001) systems has been estimated as -1 eV in average. The dissociative adsorption of oxygen in Pd/Re(0001) systems is by far less stable than in clean Re(0001) surfaces. From **Table 4.1**, the formation energy values for the stacking of Pd on Re support are also well below the strength of O adsorption on Re.

It is possible then that the O atoms tends to move inwards to approach the Re atoms. There is a clear thermodynamic driving force for O adsorption on Re(0001), as compared to O adsorption on the Pd monolayer, even if the cost of separating the Pd/Re interface is included. Provided that the kinetic barriers are not too high, this thermodynamic preference will eventually lead to the peeling off of the Pd adlayers, in agreement with the experimental observation.

## 4.4 CONCLUSIONS

The present DFT study of few-layer Pd films deposited on the Re(0001) surface has led to the following conclusions:

a) The stacking sequence observed experimentally, whereby the first layer of palladium continues the *hcp* sequence of the rhenium stacking, while consecutive layers adopt the *fcc* sequence expected for palladium, is the lowest-energy one, implying that the layer-by-layer growth is mainly thermodynamically controlled. However, in the case of deposition of 3ML Pd, the thermodynamically preferred separation into islands of 2ML- and 4ML-depth predicted by calculations has not been observed in experiment, suggesting that this rearrangement process might be kinetically limited.

b) There is a significant amount of charge transfer from Re to Pd, mainly localized at the interface layers. The charge transferred to Pd is polarized in such a way that it is “pointing” towards the Re support. That means that the transferred charge cannot be projected onto Pd *d* states, and its better described as being transferred to hybrid *sp* states in the valence.

c) The charge transfer from Re to the interface Pd adlayer produces a rigid shift to more negative energies of the electronic band centers on this Pd layer, compared to those at the next layers. But because the valence *d*-band preserves its degree of filling in all cases, its width for the interface Pd layer has to increase. In general, an inverse correlation is then observed between *d*-band center shifts and bandwidths.

d) The shift in the valence states is accompanied by an almost rigid shift in the core states. Therefore the Pd 3*d* states at the interface layer have higher binding energies than those from consecutive layers. The change in the experimental XPS as a function of the number of deposited layers is well explained by a theoretical simulation of the XPS signal: there is a gradual shift to lower binding energies as the interface layer is "buried" by further Pd deposition.

e) The charge transfer model can therefore explain in a simple way the effect of the support on the electronic structure of core and valence levels in this unstrained system. It has been shown that it is possible to establish an analogy between the application of a support-induced compressive (tensile) strain and the charge transfer to (from) the adlayer. While in the present case of Pd/Re(0001) the strain is very small and the electronic structure changes are determined by charge transfer effects, in general cases both strain and charge-transfer could contribute to the observed behavior. These results and analysis therefore call for a reexamination of the role of charge transfer in the electronic behavior of metal adlayers on metal supports.

f) Oxygen adsorption on Re(0001) is much stronger than on the 1ML Pd/Re(0001) surface. The difference is enough to overcome the Pd/Re attraction and therefore constitutes a thermodynamic driving force for a process of peeling off of the Pd adlayer and direct absorption of oxygen on Re. This conclusion is in agreement with observations in recent STM experiments.

## 4.5 REFERENCES

1 J. Ontaneda, R. A. Bennett and R. Grau-Crespo, *J. Phys. Chem. C*, 2015, **119**, 23436–23444.

2 J. A. Rodriguez, R. A. Campbell and D. W. Goodman, *J. Phys. Chem.*, 1991, **95**, 2477–2483.

3 E. Kampshoff, E. Hahn and K. Kern, *Phys. Rev. Lett.*, 1994, **73**, 704–707.

4 J. K. Nørskov, T. Bligaard, J. Rossmeisl and C. H. Christensen, *Nat. Chem.*, 2009, **1**, 37–46.

5 B. Hammer and J. K. Nørskov, *Theoretical Surface Science and Catalysis — Calculations and Concepts*, Elsevier, 2000, vol. 45.

6 B. Hammer and J. K. Norskov, *Nature*, 1995, **376**, 238–240.

7 J. R. Kitchin, J. K. Nørskov, M. A. Barteau and J. G. Chen, *Phys. Rev. Lett.*, 2004, **93**, 156801.

8 M. Mavrikakis, B. Hammer and J. K. Nørskov, *Phys. Rev. Lett.*, 1998, **81**, 2819–2822.

9 L. a Kibler, A. M. El-Aziz, R. Hoyer and D. M. Kolb, *Angew. Chemie Int. Ed.*, 2005, **44**, 2080–4.

10 J. R. Kitchin, J. K. Nørskov, M. A. Barteau and J. G. Chen, *J. Chem. Phys.*, 2004, **120**, 10240–10246.

11 H. Lüth, *Solid Surfaces, Interfaces and Thin Films*, Springer, Germany, Fifth Edit.,

2010.

12 H. A. Etman, Z. V. Zheleva, G. Held and R. A. Bennett, *J. Phys. Chem. C*, 2011, **115**, 4191–4199.

13 B. Mun, C. Lee, V. Stamenkovic, N. Markovic and P. Ross, *Phys. Rev. B*, 2005, **71**, 115420.

14 R. Wu and A. Freeman, *Phys. Rev. B*, 1995, **52**, 12419–12425.

15 G. Kresse and J. Furthmüller, *Comput. Mater. Sci.*, 1996, **6**, 15–50.

16 G. Kresse and J. Furthmüller, *Phys. Rev. B*, 1996, **54**, 11169–11186.

17 J. P. Perdew, K. Burke and M. Ernzerhof, *Phys. Rev. Lett.*, 1996, **77**, 3865–3868.

18 P. E. Blöchl, *Phys. Rev. B*, 1994, **50**, 17953–17979.

19 G. Kresse and D. Joubert, *Phys. Rev. B*, 1999, **59**, 1758–1775.

20 G. P. Francis and M. C. Payne, *J. Phys. Condens. Matter*, 1990, **2**, 4395–4404.

21 G. Makov and M. Payne, *Phys. Rev. B*, 1995, **51**, 4014–4022.

22 H. J. Monkhorst and J. D. Pack, *Phys. Rev. B*, 1976, **13**, 5188–5192.

23 R. W. G. Wyckoff, *Crystal Structures, Volume 1*, Interscience Publishers, New York, Second., 1963.

24 P. Haas, F. Tran and P. Blaha, *Phys. Rev. B*, 2009, **79**, 085104.

25 R. F. W. Bader, *Atoms in Molecules: A Quantum Theory*, Oxford University Press, Oxford (UK), 1990.

26 G. Henkelman, A. Arnaldsson and H. Jónsson, *Comput. Mater. Sci.*, 2006, **36**, 354–360.

27 E. Sanville, S. D. Kenny, R. Smith and G. Henkelman, *J. Comput. Chem.*, 2007, **28**, 899–908.

28 W. Tang, E. Sanville and G. Henkelman, *J. Phys. Condens. Matter*, 2009, **21**, 084204.

29 M. Birgersson, C.-O. Almbladh, M. Borg and J. Andersen, *Phys. Rev. B*, 2003, **67**, 045402.

30 D. R. Lide, *CRC Handbook of Chemistry and Physics*, CRC Press, Boca Raton, 85th edn., 2004.

31 M. Weinert and R. E. Watson, *Phys. Rev. B*, 1995, **51**, 17168–17180.

32 D. Hennig, M. Ganduglia-Pirovano and M. Scheffler, *Phys. Rev. B*, 1996, **53**, 10344–10347.

33 M. Ganduglia-Pirovano, V. Natoli, M. Cohen and J. Kudrnovský, *Phys. Rev. B*, 1996, **54**, 8892–8898.

34 E. Golfetto, A. Baraldi, M. Pozzo, D. Alfè, A. Sala, P. Lacovig, E. Vesselli, S. Lizzit, G. Comelli and R. Rosei, *J. Phys. Chem. C*, 2010, **114**, 436–441.

35 J. A. Rodriguez and D. W. Goodman, *J. Phys. Chem.*, 1991, **95**, 4196–4206.

36 C. Stampfl and M. Scheffler, *Phys. Rev. B - Condens. Matter Mater. Phys.*, 1996, **54**, 2868–2872.

37 P. Stampfl, S. Schwegmann, H. Over, M. Scheffler and G. Ertl, *Phys. Rev. Lett.*,

1996, **77**, 3371–3374.

38 E. Lundgren, G. Kresse, C. Klein, M. Borg, J. N. Andersen, M. De Santis, Y. Gauthier, C. Konvicka, M. Schmid and P. Varga, *Phys. Rev. Lett.*, 2002, **88**, 2461031–2461034.

39 M. Todorova, K. Reuter and M. Scheffler, *J. Phys. Chem. B*, 2004, **108**, 14477–14483.

40 M. V. Ganduglia-Pirovano and M. Scheffler, *Phys. Rev. B - Condens. Matter Mater. Phys.*, 1999, **59**, 15533–15543.

41 W.-X. Li, C. Stampfl and M. Scheffler, *Phys. Rev. B*, 2002, **65**, 075407.

# 5 Isolated and metal-supported hexagonal boron nitride layers

This Chapter presents a theoretical investigation of free-standing and metal-supported hexagonal boron nitride (*h*-BN) layers. We present a detailed analysis of the origin of the so-called monolayer Raman signature, consisting of an upshift in the frequency of the $E_{2g}$ vibrational mode with respect to the bulk value. Our analysis is based on the comparison of different density functionals, including those that feature non-local correlation for an accurate description of van der Waals (dispersion) interactions. We also discuss the interaction of *h*-BN with a metal surface, Ni{111}, and discuss the effect of that interaction on the Raman spectrum of monolayer *h*-BN. This Chapter contains material of our recent paper published in *Journal of Physics: Condensed Matter*.[1] The final part about the interaction of *h*-BN with Ni{111} is still unpublished.

## 5.1 INTRODUCTION

Hexagonal boron nitride (*h*-BN) is a layered material with a structure similar to that of graphite, but with alternating B and N atoms, instead of C atoms, forming honeycomb-like networks.[2] Its properties have been attracting a great deal of interest over the last years[3] since the availability of *h*-BN samples with an atomically flat surface[4] facilitates studies of thin films applications. For instance, flakes of *h*-BN have been used as a thin dielectric to top-gate graphene in electronic devices,[5] as well as an inert substrate for graphene.[6] Song *et al.*[7] demonstrated that *h*-BN films consisting of two to five atomic layers can be synthetized via epitaxial growth on copper and then transferred onto a chosen substrate, opening up new opportunities to exploit its properties and potential applications in electronics, especially as an interesting two-dimensional defect-free dielectric material when sandwiched between conducting materials.[8]

In the case of graphene, the identification of the number of layers in mono-, bi- and few- layers is often done via either optical contrast[9] or Raman signatures.[10] The same two strategies have been discussed by Gorbachev and co-workers to identify mono- and few-layers *h*-BN.[11] However, because of its large bandgap (above 5 eV),[11–13] *h*-BN has zero opacity, i.e. it exhibits very weak optical contrast.[11] Raman spectroscopy seems to be a better route, particularly to avoid misidentification of mono- and bi-layers of *h*-BN as they look very similar under the microscope. Experimentally, bulk *h*-BN exhibits a characteristic Raman peak occurring at 1366 cm$^{-1}$ corresponding to an $E_{2g}$ phonon mode. Gorbachev *et al.*[11] observed that mono- and bilayers *h*-BN exhibited maximum upshifts of 4 cm$^{-1}$ and 1 cm$^{-1}$, respectively, which could serve as Raman signatures of these systems.

A previous theoretical study[14] based on density functional theory (DFT) calculations with the local density approximation (LDA), suggested that the difference between frequencies of Raman peaks in bulk *h*-BN and a single sheet is due to slightly elongated B-N bonds in the former, causing a softening of the $E_{2g}$ phonon mode. However, as we will discuss in more detail below, the LDA functional employed in that work is unable to account correctly for the interlayer interactions in *h*-BN, in particular the dominant dispersion component, so a more sophisticated theoretical analysis is needed.

Recent experiments by Cai *et al.*[15] on suspended *h*-BN samples revealed much smaller upshifts (up to ~1 cm$^{-1}$) in the Raman frequency from bulk to monolayer. The authors suggested that the larger upshifts of ~4 cm$^{-1}$ observed in supported samples are actually due to the interaction with the support. According to this interpretation, the higher flexibility of the monolayer allows it to follow the uneven surface of the substrate more closely and gain more compressive strain; the intrinsic shift may be very small or non-existent.

Here we present a complete theoretical analysis, using DFT functionals that are able to describe correctly the dispersion interactions between layers, in an attempt to clarify whether there is an intrinsic upshift in the Raman frequency of the *h*-BN monolayer. We discuss the role of interlayer dispersion interactions in determining the relative cell parameters and Raman frequencies of the bulk and monolayer, and calculate the effect of thermal expansion on the Raman signature of the BN-monolayer. We will also discuss the interaction of *h*-BN with the Ni{111} surface and the effect of this interaction on the Raman frequency.

## 5.2 COMPUTATIONAL METHODS

Density functional theory (DFT) calculations were preformed using planewave basis sets as implemented in VASP.[16,17] The projector augmented wave (PAW)[18,19] method was used to describe the interaction between the valence electrons and the core, keeping the 1*s* orbitals of both B and N frozen in the atomic reference configurations. As we will discuss below, the change in lattice parameter from bulk to monolayer is in the order of a fraction of picometer; therefore, the simulations required high precision parameters to capture these subtle effects. In particular, the "hard" frozen-core potentials provided in VASP code were used. Using the "normal" potential leads to the same trends described here, but introduces an error (in the order of 0.1 pm, which is small but significant for this study) in the relative values of the cell parameters of bulk vs. single-layer, compared to the results obtained with the hard potentials. Planewave basis set was truncated at a kinetic energy cutoff of 1050 eV (set at 50% above the default value for the potentials, in order to minimize Pulay errors).[20] In order to reduce the noise in the calculated forces, simulations employed an additional support grid with 8 times more points than the standard fine grid, for the evaluation of the augmentation charges. The maximum force on ions for geometry relaxations was set up to a very low threshold of $10^{-4}$ eV/Å (reducing this value even more to $10^{-5}$ eV/Å has no effect on the calculated geometries to the precisions reported here).

Monkhorst-Pack grids[21] with a maximum separation of 0.35 $Å^{-1}$ between **k**-points were used in sampling the Brillouin-zone for integrations. This grid density corresponds to a 9×9×3 grid of **k**-points in the bulk *h*-BN. The calculations of bulk *h*-BN were performed using the experimentally observed AA′ stacking sequence where B and N are placed on top of each other,[22] as illustrated in **Figure 5.1**. In the simulations of the layered structures, a relatively large vacuum space of 15 Å was placed perpendicular to the layers in order to keep interactions between periodic images small. Vibrational frequencies were obtained using a finite-differences method, where symmetry was employed to reduce the number of displacements.

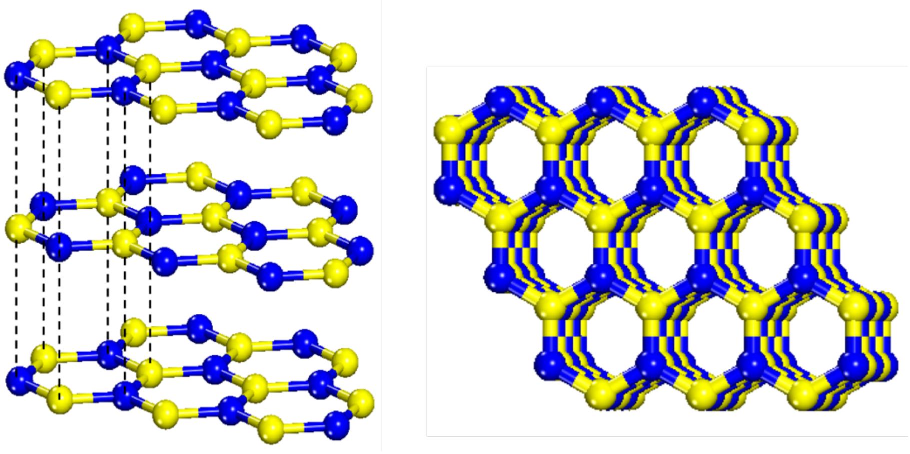

**Figure 5.1** Schematic representation of bulk *h*-BN with the AA′ stacking mode where B and N are placed on top of each other. Yellow and blue spheres correspond to B and N atoms, respectively.

We compared results obtained from calculations with various functionals including those based on the local density approximation (LDA)[23] and on the generalized gradient approximation (GGA) in the formulation by Perdew-Burke-Ernzerhof (PBE)[24], as well as their empirical corrections by Grimme's method (D2 and D3).[25,26] We also consider a set of functionals where dispersion is treated with explicit non-local correlation: the original vdW-DF method[27] (referred to as revPBE-vdW herein), the modified version vdW-DF2[28] (referred to as rPW86-vdW2 herein) and three of the "opt" series (optB88-vdW, optB86b-vdW and optPBE-vdW) where the exchange functionals were optimized for the correlation part,[29] as developed and implemented in VASP by Klimeš *et al.*[30]

Interlayer binding energies $E_\mathrm{b}$ for bulk *h*-BN were calculated as the energy difference (per atom) between bound and separated layers:

$$E_\mathrm{b} = \frac{E_\mathrm{bulk} - 2E_\mathrm{ML}}{4} \tag{5.1}$$

where $E_\mathrm{ML}$ and $E_\mathrm{bulk}$ are the energies of the monolayer cell (containing 2 atoms) and of the bulk cell (containing 2 layers and 4 atoms).

Calculation of the equilibrium structure of *h*-BN at finite temperatures were carried out by minimizing the vibrational free energy:

$$\begin{aligned} F(\{a_i\},T) &= E(\{a_i\}) + F_\mathrm{vib}\big(\omega_{\mathbf{q},j}(\{a_i\}),T\big) \\ &= E(\{a_i\}) + \sum_{\mathbf{q},j} \frac{hc\omega_{\mathbf{q},j}(\{a_i\})}{2} + k_\mathrm{B}T \sum_{\mathbf{q},j} \ln\left[1 - \exp\left(-\frac{hc\omega_{\mathbf{q},j}(\{a_i\})}{k_\mathrm{B}T}\right)\right] \end{aligned} \tag{5.2}$$

with respect to the cell parameters $\{a_i\}$. In this equation, $E(\{a_i\})$ corresponds to the ground-state energy of the structure at a given set of lattice parameters, $\omega_{\mathbf{q},j}(\{a_i\})$ is the frequency in cm$^{-1}$ of the $j^\mathrm{th}$ phonon band at the point $\mathbf{q}$ in the Brillouin zone, $h$ is Planck's constant, $c$ is the speed of light, $k_\mathrm{B}$ is Boltzmann's constant, and $T$ is the absolute temperature. This is called the quasiharmonic approximation (QHA), because the dependence of the phonon frequencies on the structural parameters introduces anharmonic effects in the calculation and permits the prediction of thermal expansion. Since the frequency of each mode in the Brillouin zone varies linearly with the cell parameters to a good approximation within the region of interest, we performed phonon calculations at a small grid of cell parameters and fit linear equations for all modes, as previously done by Mounet and Marzari in the simulation of the thermal behavior of graphene and graphite.[31] Combined with a polynomial expansion of the energies around the equilibrium point, this procedure allows to define an analytical expression for the free energy, which can be then minimized at any given temperature.

To account for the effect of Ni{111} support on the Raman signature of *h*-BN monolayer, the computational setup was modified. As it was stated before, the "normal" pseudopotentials lead to the same trends described below, so they can be employed safely here to compensate for the higher computational cost of including the metal surface in the calculation. The number of planewaves in the calculations was limited by a kinetic energy cutoff of 410 eV, which is still slightly above the recommended value for the "normal" PAW potentials. To sample the Brillouin zone, a **k**-point grid of 7×7×1 was used. The threshold for forces acting on ions was set to 0.005 eV $Å^{-1}$. The Ni substrate was modeled with a periodic slab of six atomic layers. Only the three uppermost Ni layers were fully relaxed, while the three bottom layers were fixed in their bulk positions. A vacuum gap of 20 Å was included above the surfaces to avoid interactions between periodic cells. As nickel is a ferromagnetic metal, all calculations included spin polarization.

The interaction energy $E_{\text{int}}$ between $n$ layers of *h*-BN (per unit cell) and the Ni{111} surface was estimated as:

$$E_{\mathrm{int}} = E_{\mathrm{interf}} - (nE_{h-\mathrm{BN}} + E_{\mathrm{subst}}) \tag{5.3}$$

where $E_{\mathrm{interf}}$ is the total energy of the $h$-BN/Ni$\{111\}$ system, $E_{h-\mathrm{BN}}$ is the total energy of a free-standing (unstrained) $h$-BN sheet, and $E_{\mathrm{subst}}$ is the energy of the clean Ni$\{111\}$ slab. All these energies are taken per unit cell.

# 5.3 RESULTS AND DISCUSSION

## 5.3.1 Variation of Raman frequency with in-plane cell parameter

The $E_{2g}$ is a doubly-degenerate Raman-active mode which involves the in-plane vibration of B and N atoms in opposite directions, as illustrated in the inset of **Figure 5.2**. As a starting point, the $E_{2g}$ Raman frequencies of a single layer were calculated as a function of cell parameter, with each of the functionals. The results are summarized in **Figure 5.2**. The absolute value of the frequency predicted at a given cell parameter (say at the experimental room temperature cell parameter of the bulk $a$=2.5047 Å),[32] varies with the functional. However, results from all functionals are quite similar in the magnitude of the rate of frequency change with lattice parameter, which is approximately 22 cm$^{-1}$/pm. The Raman frequencies increase with the decrease in cell parameter, which is expected since a lattice contraction means shortening and stiffening of the B–N bond, producing a hardening of the $E_{2g}$ mode.

We now present results of analogous calculations for the bulk, keeping the $c$ parameter initially fixed (we used here the experimental value extrapolated to zero temperature, $c$=6.60002 Å, in Ref. 32; the results of full geometry relaxations will be discussed next). For any of the functionals used here, there is very little variation of frequency between the bulk and the single layer at a given cell parameter. In fact, the frequency vs. cell parameter lines calculated for the bulk cannot be distinguished in a plot from those calculated for the single layer, and we have not plotted them separately. There is only a small shift from single layer to bulk (values given in brackets in **Figure 5.2**), which is negative for all functionals (except for LDA), and below 1 cm$^{-1}$ for most functionals (except the original vdW-DF functionals, for which the shifts are only slightly larger). This result, which is not surprising as $E_{2g}$ is an in-plane mode, makes it clear that the experimental frequency difference between single layer and bulk cannot be attributed *directly* to the interlayer interactions: it must be the result of the difference in cell parameter between the two systems.

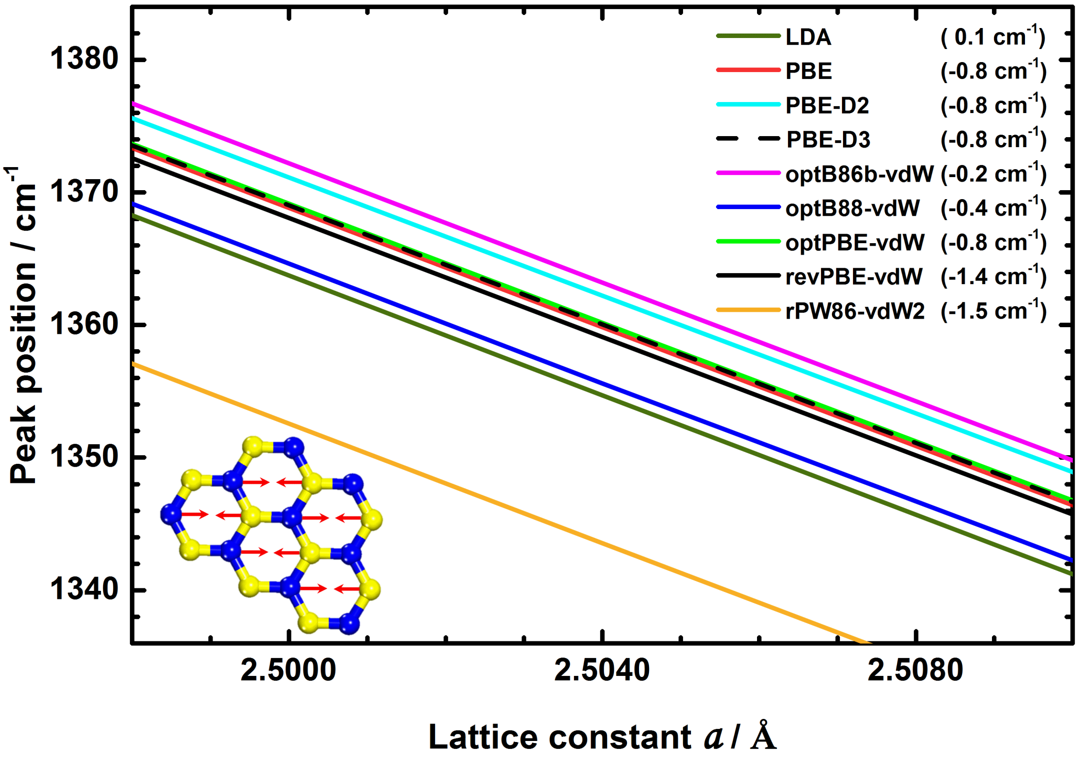

**Figure 5.2** Relationship between Raman frequencies and cell parameters of single-layer boron nitride, as calculated with different density functionals. The behavior of the bulk is identical, except for small constant shifts (given in brackets in the legend).

The frequency of $E_{2g}$ mode of the bulk calculated at the experimental cell parameter is slightly below its experimental value for the bulk (1366 cm$^{-1}$)[11] for all functionals (only the rPW86-vdW2 exhibits a relative large deviation of 24 cm$^{-1}$). However, we are not interested here in predicting the absolute values (which in any case are very sensitive to cell parameter variations due to thermal effects not included in our calculations), but on understanding the relative values between the bulk and the few-layer systems.

### 5.3.2 Variation of equilibrium lattice parameter from monolayer to bulk

The analysis above suggests that the experimentally observed upshifts in the Raman frequency from bulk to monolayer could be due to a small contraction of the lattice parameter of the latter with respect to the former, which would be in agreement with the conclusion reached in Ref. 11 and 14. However, the contraction required to explain even the largest experimental signature reported for the *h*-BN monolayer (4 cm$^{-1}$) is quite small, of 0.2 pm. We will now consider whether DFT simulations reproduce this small lattice contraction based on equilibrium geometry calculations via energy minimizations.

The comparison between the equilibrium geometries of bulk and a single layer obviously requires the correct description of the bulk interlayer attraction, which, like in graphite, has two main components: 1) the dispersion interaction, and 2) the electronic kinetic energy reduction due to an increased delocalization of the 2$p_z$ orbitals between adjacent layers.[33] In the case of *h*-BN the atoms are slightly charged due to the polarity of the B-N bond, so there is also a small contribution from direct Coulombic interactions between layers. It is well known for graphite that GGA functionals like PBE cannot account for the interlayer attraction, whereas the LDA does give a reasonable interlayer potential with a minimum close to the experimental value.[33,34] **Figure 5.3** shows the comparison between the LDA, PBE and optB88-vdW interlayer potentials at constant lateral cell parameter for *h*-BN. As for graphite, the LDA interlayer potential for *h*-BN exhibits a well-defined minimum close to the experimental value of the interlayer distance. This "success" of the LDA masks its actual inability to properly describe the physics of the interlayer interaction. In fact, neither the GGA nor the LDA are able to account for long-range dispersion interactions, which are non-local correlation effects. In the LDA, however, the kinetic energy reduction effect is exaggerated by the tendency of this functional to overdelocalize the charge density. Because of the cancellation of these errors, the LDA interlayer potential mimics the correct one, albeit with a smaller binding energy and a too fast falloff at long distances, compared to functionals including non-local correlations.

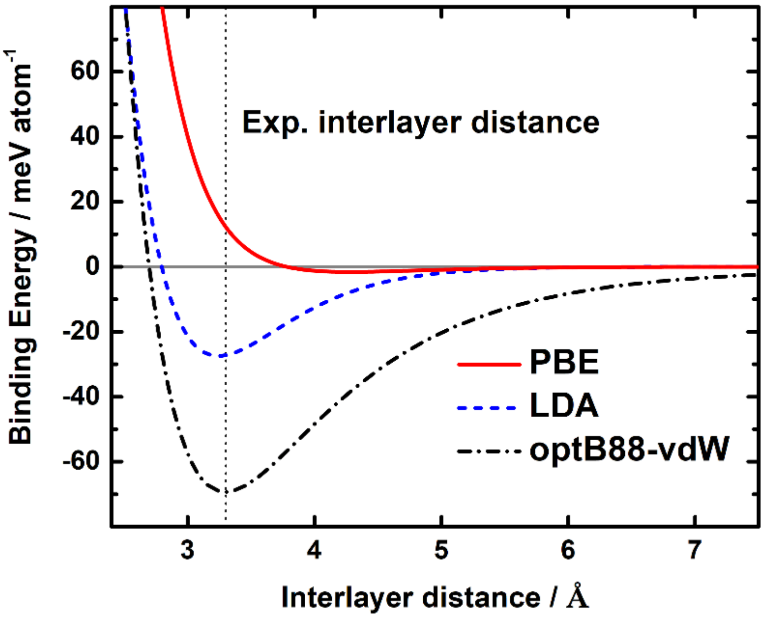

**Figure 5.3** Interlayer binding energy (per atom) of bulk *h*-BN as a function of interlayer distance ($c/2$) calculated by LDA, PBE and optB88-vdW. In all these calculations, the lattice constant $a$ was fixed to the bulk experimental value (2.5059 Å).

**Table 5.1** summarizes the relaxed cell parameters of bulk *h*-BN as obtained from several functionals considered here. In all cases, the $a$ lattice parameter is reasonably well described. However, the performances of these functionals in predicting the $c$ lattice parameter are quite different. In the case of GGA-PBE, the very weak interlayer interaction leads to too large *c* value. The empirically-corrected versions show an interesting behavior: PBE-D2 underestimates the interlayer distance by 7.3% whereas its redefined version, PBE-D3, overestimates it by only 1.8% which marks a significant improvement in the description of interlayer interactions. Among the non-local-correlation (NLC) functionals, the optB88-vdW functional gives the most accurate value of the *c* lattice parameter, which corresponds to a deviation of -1.1%.

**Table 5.1** Calculated equilibrium lattice parameters (ignoring vibrational effects), Raman-active ($E_{2g}$) frequencies, and interlayer binding energies of bulk *h*-BN using different functionals, and comparison with room-temperature experimental values.

| Functional | $a$ (Å) | $c$ (Å) | Deviation from experiment $\Delta a/a_{exp}$ (%) | Deviation from experiment $\Delta c/c_{exp}$ (%) | $\omega[E_{2g}]$ (cm$^{-1}$) | $E_b$ (meV/atom) |
|---|---|---|---|---|---|---|
| **Experiment** | 2.5059[32] | 6.6000[32] | - | - | 1366[11] | |
| **LDA** | 2.4911 | 6.4886 | -0.6 | -1.7 | 1383.8 | -27.1 |
| **PBE** | 2.5119 | 8.5022 | 0.2 | 28.8 | 1342.2 | -1.6 |
| **PBE-D2** | 2.5082 | 6.1716 | 0.1 | -6.5 | 1350.5 | -76.9 |
| **PBE-D3** | 2.5086 | 6.7793 | 0.1 | 2.7 | 1349.0 | -49.0 |
| **optB86b-vdW** | 2.5120 | 6.5170 | 0.2 | -1.3 | 1344.8 | -69.8 |
| **optB88-vdW** | 2.5108 | 6.5896 | 0.2 | -0.2 | 1339.8 | -69.5 |
| **optPBE-vdW** | 2.5168 | 6.7884 | 0.4 | 2.9 | 1331.0 | -63.4 |
| **revPBE-vdW** | 2.5235 | 7.1011 | 0.7 | 7.6 | 1315.2 | -52.4 |
| **rPW86-vdW2** | 2.5217 | 6.9814 | 0.6 | 5.8 | 1303.6 | -50.4 |

**Table 5.1** also displays the interlayer binding energies calculated with each functional at the corresponding equilibrium geometries. There are no experimental values for the binding energy of *h*-BN. Our calculations are in good agreement with those previously

reported by Graziano *et al.* using a similar list of functionals.[35] Based on the comparison with graphite calculations, these authors concluded that the interlayer binding energy from non-local-correlation functionals were the most sensible, whereas other empirically corrected functionals, like PBE-D2 and also the Tkatchenko-Scheffler-corrected PBE, slightly overestimated the binding energies.

**Table 5.2** Calculated equilibrium lattice parameter (ignoring vibrational effects) and Raman active ($E_{2g}$) frequencies of single-layer *h*-BN using different functionals, and comparison with corresponding values for the bulk.

| | **Lattice parameter** | | **$\omega[E_{2g}]$ (cm$^{-1}$)** | |
|---|---|---|---|---|
| **Functional** | **$a$ (Å)** | **Change from bulk (pm)** | **1L** | **Change from bulk** |
| **Experiment**[11] | - | - | 1370 | 4 |
| **LDA** | 2.4897 | -0.14 | 1387.1 | 3.3 |
| **PBE** | 2.5119 | -0.01 | 1342.3 | 0.1 |
| **PBE-D2** | 2.5121 | 0.39 | 1344.2 | -6.4 |
| **PBE-D3** | 2.5108 | 0.22 | 1344.8 | -4.2 |
| **optB86b-vdW** | 2.5102 | -0.18 | 1349.3 | 4.5 |
| **optB88-vdW** | 2.5091 | -0.17 | 1344.2 | 4.4 |
| **optPBE-vdW** | 2.5154 | -0.14 | 1334.7 | 3.7 |
| **revPBE-vdW** | 2.5225 | -0.10 | 1318.1 | 2.9 |
| **rPW86-vdW2** | 2.5207 | -0.10 | 1306.4 | 2.8 |

We now analyze the geometry of an isolated layer after relaxation, in comparison with the bulk. **Table 5.2** lists the *a* lattice parameters obtained from calculations with each functional, and the relative values with respect to the bulk. All the NLC functionals (and the LDA) predict small contractions (between 0.1 and 0.2 pm) with respect to the bulk, which is the expected trend if the experimental Raman signature is interpreted as resulting from a lattice contraction. Interestingly, the Grimme functionals PBE-D2 and PBE-D3 predict instead a small expansion with respect to bulk values. The GGA-PBE frequencies are almost identical for bulk and single layer, since the optimization of the bulk geometry with this functional leads to a very large (unrealistic) interlayer separation. **Table 5.2** also shows the absolute values of the Raman frequencies calculated at the equilibrium geometries in both bulk and single-layer *h*-BN. The small contractions from bulk to single layer predicted by the non-local-correlation functionals can in principle account for the experimental upshift in Raman frequency. The magnitude of the variations in Raman frequencies predicted by the "opt" series of functionals, from 3.7 to 4.5 $\text{cm}^{-1}$, is in agreement with the values obtained from experiments in supported samples, although significantly higher than the experimental upshifts in suspended samples (up to ~1 $\text{cm}^{-1}$).[15] In contrast, PBE-D2 and PBE-D3 predict a downshift in frequency from bulk to single layer, in disagreement will all experiments.

### 5.3.3 Role of non-local correlation in the lattice expansion from monolayer to bulk

In order to understand the different predictions of the monolayer-to-bulk cell variation from Grimme-corrected and NLC functionals, we have analyzed the variation in the energy of the bulk, calculated with either the PBE-D3 or the optPB88-vdW functional, upon contraction/expansion of the layer plane, at a fixed $c$ parameter. It is possible to decompose that energy variation into monolayer contributions (i.e. twice the energy variation obtained in the calculation of the isolated layer) and interlayer interaction effects (i.e. contributions to the binding energy $E_\text{b}$). An energy decomposition analysis reveals that, in the PBE-D3 calculations, the dispersion component (given by the Grimme term) is the dominant contribution to the inter-layer energy variation (the magnitude of the contributions from the other, non-dispersive interactions is only ~10% of the dominant contribution). On the other hand, in the optB88-vdW calculations, the dominant contribution to the inter-layer energy variation is the non-local correlation term (in this case the other contributions represent ~30% of the dominant one).

**Figure 5.4** shows the energy variation with *a* for bulk and monolayer, as well as the contribution of the dispersion or NLC terms to the interlayer interactions. The difference in behavior between the inter-layer dispersion interaction term in the Grimme-corrected functional and the inter-layer non-local correlation term in the NLC functionals can explain the different output from the two types of functional.

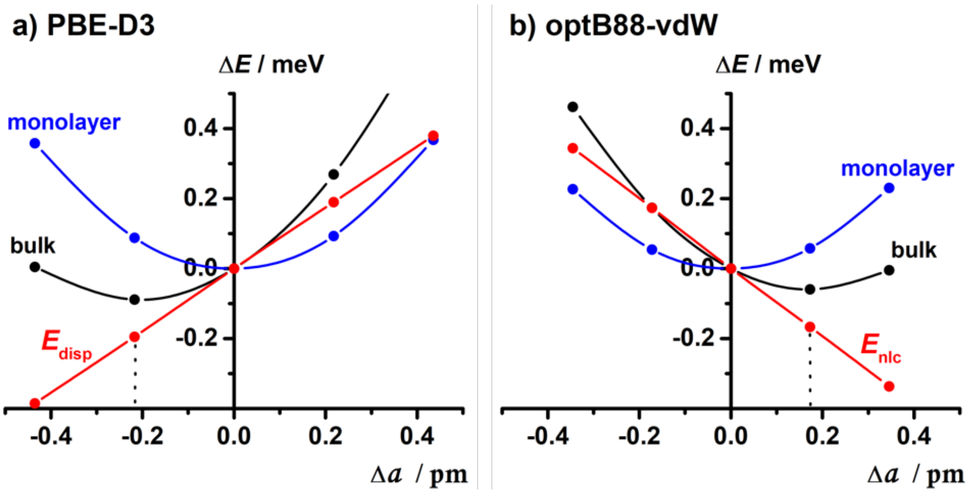

**Figure 5.4** Variation of the monolayer and bulk energies around the equilibrium in-plane lattice parameter. The reference for the energies are the values of the given energy component at the cell parameter at which the monolayer is in equilibrium (for each functional).

In the PBE-D3 case, one can expect that the inter-layer dispersion interaction, given the simple mathematical definition of the Grimme correction as an attractive force, will tend to contract the layers, and this is indeed our observation. However, in the optB88-vdW, the non-local correlation does not behave in the same way, and it tends to expand the layers. The fact that the description of the bulk-to-monolayer contraction requires a proper treatment of non-local electron correlation is interesting. This analysis indicates that the contraction cannot be accounted for by invoking a simple picture of intra-plane bond weakening due to the interaction of $p_z$ electrons. The effect is more complex and requires the consideration of non-local correlation effects.

Considering that the calculation of the relevant interactions is more sophisticated and accurate in the NLC functionals than in the Grimme-corrected GGA ones, we believe that the small lattice expansion of the bulk (in comparison with the monolayer) predicted by the former type of functional is reliable, at least in the low-temperature limit (the effect of finite temperatures will be discussed below). The LDA is able to mimic the correct behavior, but based on the wrong physics as explained above.

### 5.3.4 Variation of Raman frequency with the number of layers

Using the optB88-vdW functional, we now consider the behavior of *N*-layer *h*-BN structures, with *N* up to 5. **Figure 5.5** shows the calculated frequency shifts with respect to the bulk, in comparison with the experimental data by Cai *et al.*[15] on both supported and suspended samples. In bilayers, optB88-vdW method predicts an upshift of 2.4 cm$^{-1}$ in the Raman frequency because of the contraction in the *a* parameter by 0.10 pm with respect to bulk. That value is in the middle of the range measured by Cai *et al.* on supported samples (between 1.8 and 3.2 cm$^{-1}$), but significantly above the values measured for suspended samples (~0.5 cm$^{-1}$). In an earlier experiment, Gorbachev *et al.* had measured a range of downshifts and upshifts for supported bilayers with respect to bulk,[11] but interpreted the maximum upshift of ~1 cm$^{-1}$ as the intrinsic value for the bilayer, with the other values arising from downshifts due to the interaction with the support. The calculated upshift for the trilayer 1.4 cm$^{-1}$ (contraction of 0.06 pm with respect to bulk) is close to the maximum value obtained for supported samples in Ref. 15, but again above the values measured in suspended samples. In the case of 4L and 5L, we have found upshifts of 1.1 cm$^{-1}$ (0.05 pm) and 1.0 cm$^{-1}$ (0.04 pm), respectively, i.e. the differences with respect to the bulk decrease with the increase in the number of layers $N$, as expected. The relative peak position $\Delta\omega$ is found to be proportional to $1/N$ (correlation $R^2 = 0.997$), with a proportionality constant of 4.5 cm$^{-1}$ (**Figure 5.5** inset).

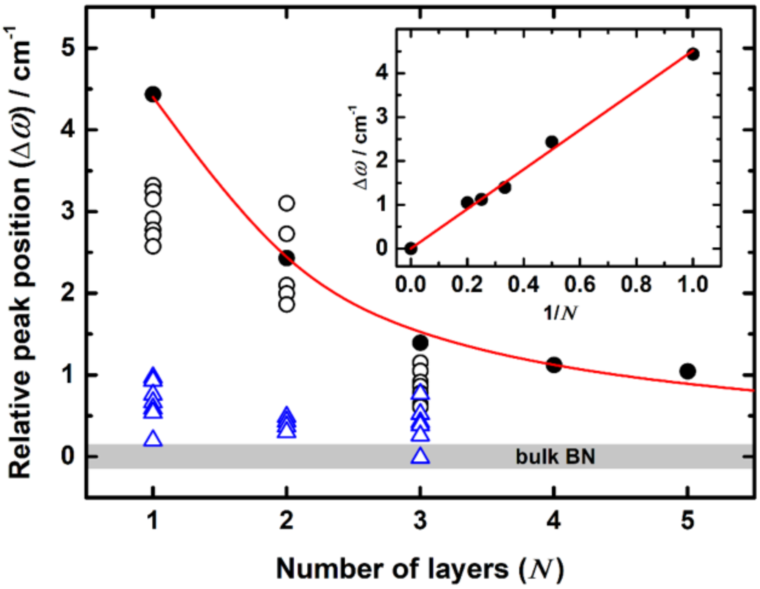

**Figure 5.5** Relative positions of the Raman peaks for few-layer *h*-BN, with respect to the bulk, as obtained from optB88-vdW calculations ignoring vibrational normal modes contributions (solid circles). The red line is the fitting of a $1/N$ law (see inset); the open circles and open blue triangles are the experimental values reported in Ref. 15 for supported and suspended samples, respectively.

### 5.3.5 Vibrational effects: finite-temperature calculations

All the results presented above were obtained ignoring vibrational contributions and therefore any thermal expansion effects. However, due to the small magnitude of the changes in cell parameters between bulk and monolayer involved in the present discussion, thermal effects are likely to be important. To account for these, temperature-dependent optimizations were performed for the cell parameters of bulk and monolayer, using the quasiharmonic approximation.

The results are displayed in **Figure 5.6**. Similarly to what was reported for graphite in Ref. 31, in *h*-BN the out-of-plane parameter (*c*) expands significantly with temperature (~5.60 pm from zero to room temperature), while the in-plane parameter *a* contracts, but only a little (~0.16 pm from zero to room temperature). Our results agree very well with the experimentally measured variation of bulk *h*-BN cell parameters with temperatures between 0 and 300 K as reported by Paszkowicz *et al.* in Ref. 32 (discounting the discrepancies in absolute values). The in-plane lattice contraction of bulk *h*-BN with temperature was first reported by Pease in Ref. 22. The physics of the in-plane lattice contraction in *h*-BN (bulk and monolayer) at low temperature can be expected to be the same as in graphite/graphene, i.e. to be caused primarily by low-frequency flexural phonons (acoustic out-of-plane modes).[36] However, the contraction of monolayer *h*-BN between 0 and 300 K is less than half of that in graphene over the same temperature range, which can be explained by the more negative Grüneisen parameters of the flexural modes of the latter[31] compared to the former.[15]

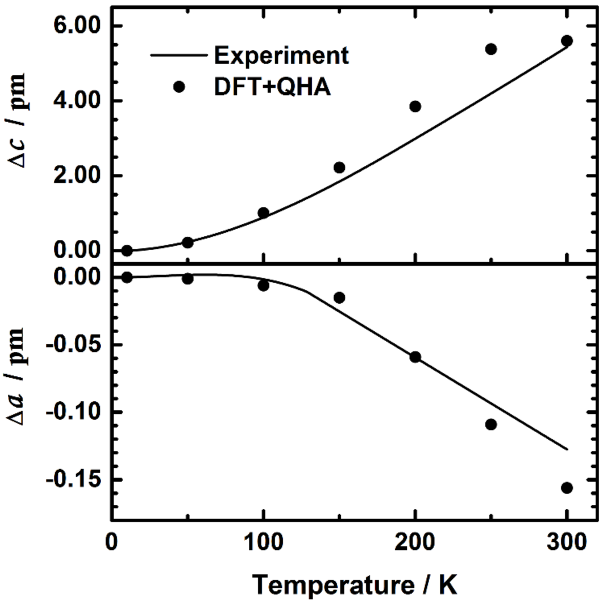

**Figure 5.6** Relative dependence of bulk *h*-BN lattice parameters on temperature. The solid lines represent polynomial fittings to the experimental data as given in Ref. 32.

There is a noticeable difference between the variation of the cell parameter with temperature for the bulk and the monolayer of *h*-BN. The thermal contraction in the monolayer is smaller, less than 0.1 pm from zero to 300 K. In the bulk, most of the in-plane contraction from zero to 300 K happens above 100 K, when the negative rate of variation in cell parameter with temperature increases. This effect can be interpreted as resulting from the expansion of the *c* parameter in the bulk: as *c* expands, the atomic layers in the bulk become more like the isolated layers (in terms of electrostatic/vdW environment), so the pace of in-plane contraction in the bulk has to increase to tend towards the *a* parameter value in the isolated layer.

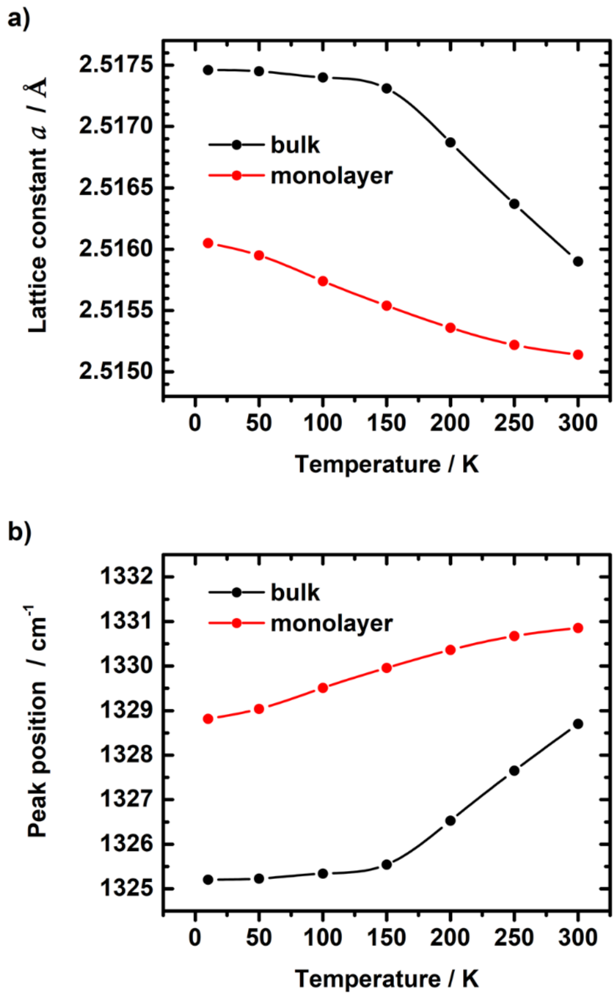

**Figure 5.7** Predicted temperature variation of (a) the in-plane lattice parameter and (b) the Raman peak position of both bulk and monolayer *h*-BN, from DFT+QHA calculations.

This observation is important to our understanding of the experimentally observed Raman signatures of the BN monolayer. **Figure 5.7a** shows that at room temperature, a significant part of the difference in *a* cell parameter (and therefore the difference in Raman frequency, as shown in **Figure 5.7b**) between bulk and single layer disappears as the results of thermal effects. This could be a possible explanation for the small difference in Raman frequency between bulk and monolayer (i.e. weak monolayer Raman signature) in the experiment with suspended samples by Cai *et al.*[15] Although our prediction for the intrinsic Raman signature of the monolayer at 300 K (~2 cm$^{-1}$) is still higher than the values of up to 1cm$^{-1}$ measured in suspended samples, our calculations that include thermal effects do tend to support the conclusion by these authors of a weak intrinsic Raman signature. This interpretation also implies that the stronger Raman signature (4 cm$^{-1}$) observed previously in supported samples is not intrinsic and is probably due to support effects. Thus, the agreement between our calculations without thermal expansion and the experimental measurements on the supported samples (shown in **Figure 5.5**) is likely to be fortuitous: the absence of finite-temperature effects in that model made the Raman signature stronger, bringing it into agreement with the support-induced value.

### 5.3.6 The effect of Ni support on the Raman signature in *h*-BN

The Ni{111} surface is an interesting substrate for atomically-thin layers of *h*-BN since the lattice constant of the former (249 pm)[37] almost perfectly fits that of the latter (251 pm)[32]. In fact, a *h*-BN monolayer overcomes the small lattice mismatch problem by introducing a slightly rumpled structure, allowing the formation of a commensurate 1×1 system.[38] In this commensurate system, N and B should occupy high-symmetry points on top of the Ni{111} surface unit cell. Early experiments[39,40] and recent theoretical work[41–43] considered three high-symmetry sites (*top*, *fcc* and *hcp*) at the Ni{111} surface for the exploration of the equilibrium interface geometries of the *h*-BN/Ni{111} structure. In a similar system, graphene on Ni{111} surfaces, high-resolution X-ray photoelectron spectroscopy (HR-XPS) have detected the coexistence of *bridge* and *top-fcc* structures.[44] Hence, we have also considered *bridge* geometries, where the B-N bond sits on *top*, *fcc* and *hcp* sites; generating three additional arrangements. Due to the presence of two atomic species in the monolayer, two inequivalent interfaces can be formed, which we call *Interface A* and *Interface B.* These interfaces cannot convert into one another by a simple translation. As a result, twelve high-symmetry configurations/interfaces were simulated, six for each interface (**Figure 5.8**).

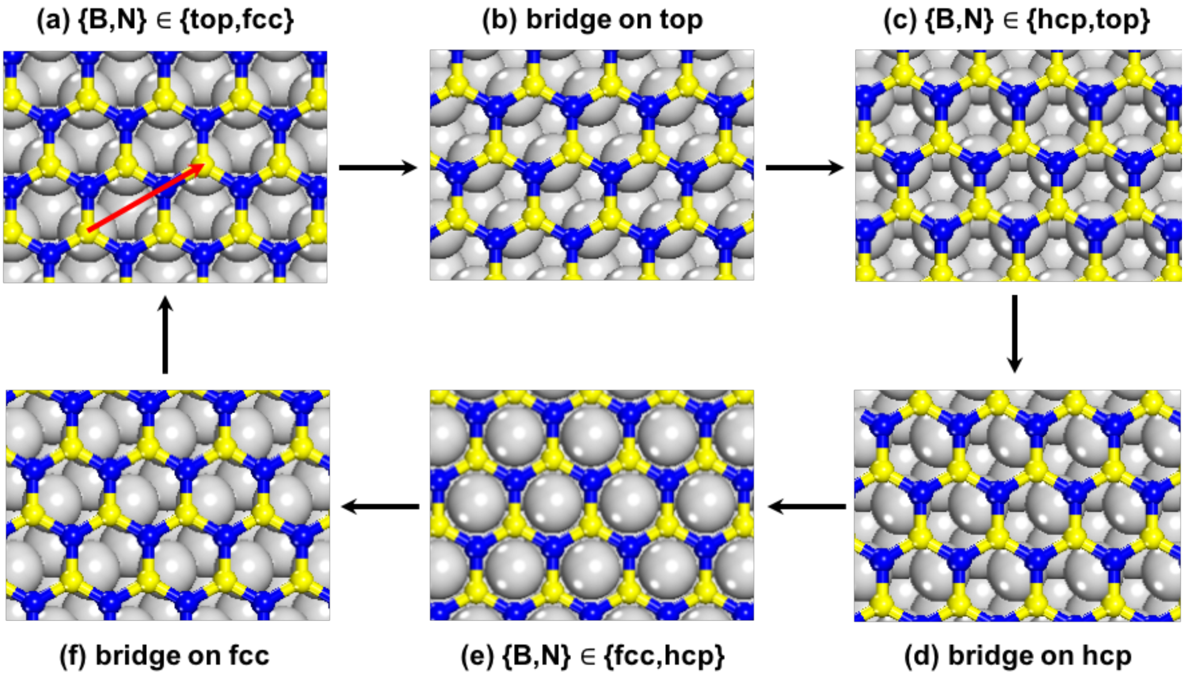

**Figure 5.8** Six different arrangements for the *h*-BN monolayer on a Ni{111} surface. The geometries evolve from each other by a small displacement of the *h*-BN monolayer relative to the Ni{111} surface in the direction along the red arrow, e.g. the B-N bond. The magnitude of a full displacement is 429.5 pm (red arrow). The scheme showed here corresponds to the *Interface A*; by swapping position of the atomic species in the *h*-BN monolayer, the *Interface B* is obtained. Key: light grey = Ni, yellow = B, and blue = N.

For each system, the potential energy surface in **Figure 5.9** was explored by fixing the lateral position of the *h*-BN atoms while letting the vertical distance from the Ni{111} plane to relax. Nevertheless, final simulations of the most stable configurations were carried out removing such constrains.

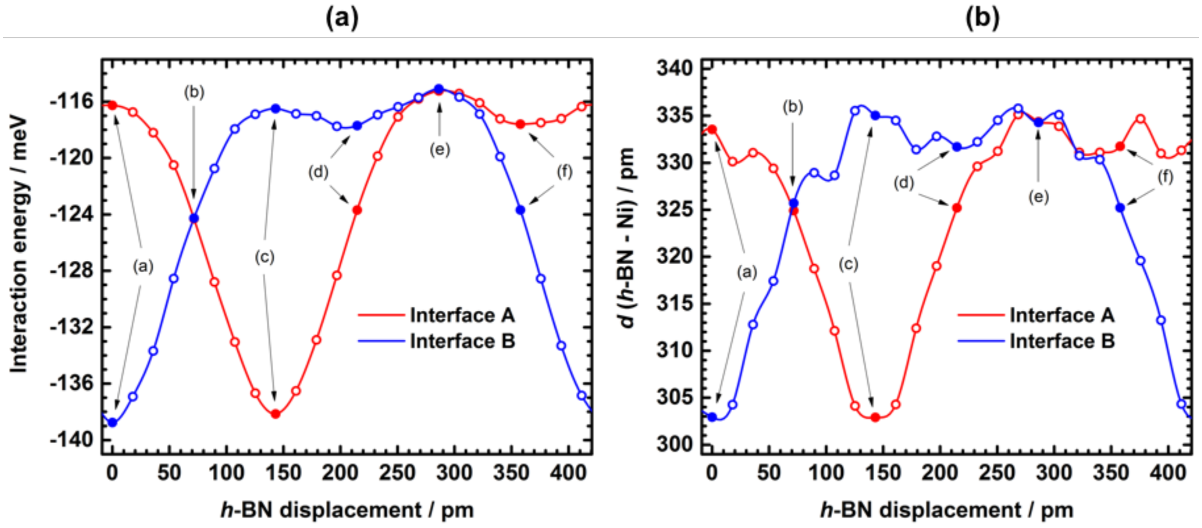

**Figure 5.9** (a) Potential energy surface given per BN formula unit and (b) change in the average distance *d* between the *h*-BN monolayer and the Ni{111} as the *h*-BN monolayer moves against the Ni{111} surface, along the B-N bond. The filled circles represent the high-symmetry configurations whereas the empty circles those configurations when the *h*-BN is shifted from one high-symmetry configuration to the next by a displacement of ~17.9 pm. The structures are depicted in **Figure 5.8**.

The potential surface energy plot (**Figure 5.9a**) reveals two global minima for the equilibrium interface geometry between the *h*-BN monolayer and Ni{111} surface. According to **Figure 5.9a**, the most stable structures are formed when N atoms are on *top* position. The B atoms, in the other hand, have two possible locations on the Ni surface: on *hcp* (found in the set of *Interface A* geometries) and on *fcc* (*Interface B*). Both conformations are energetically equivalent and equally accessible to DFT calculations according to the optB88-vdW method: B on *hcp* position is marginally less stable than B on *fcc* by 0.31 meV/atom. The remaining configurations are not minima of the potential energy surface, although they are less stable by ~12 meV/atom. Note also that those configurations where the B-N bond is in a bridge on *top*, on *hcp*, and on *fcc* site, spontaneously evolved into either *top-hcp* or *top-fcc* when lateral constraints were not imposed.

From the most stable configuration, the calculated average distance between the *h*-BN monolayer and Ni{111} is ~303 pm (see **Figure 5.9b**). Another feature to discuss is the corrugation of the *h*-BN monolayer. N- and B- atoms are practically equally separated from the Ni surface: the maximum difference in height between N and B was found to be 0.9 pm, with B atoms slightly closer to the substrate. Last but not least, the binding energy predicted by the optB88-vdW functional is small (~69 meV/atom) and thus can be interpreted as a physisorption situation mainly due to vdW interactions.

In order to validate the methods employed here, a brief review of both experimental and theoretical studies reporting this system is given now. Early LEED measurements by Gamou *et al.*[39] determined an interface structure with the nitrogen atoms on *top* sites, and boron atoms are at the *fcc* sites. In this study, the perpendicular spacing between B (N) and the topmost Ni was 204 pm (222 pm), giving a corrugation value of 18 pm for the supported *h*-BN monolayer. Later X-ray photoelectron diffraction (XPD) studies by Auwärter and co-workers[40] reported the same interface geometry but with a lower corrugation value, 7±6 pm. In recent transmission electron microscopy (TEM) measurements by Tonkikh *et al.*[43] reported a *h*-BN monolayer-Ni separation of 187±12 pm. Previous theoretical work employing the PBE-D2 approach to account for the vdW interactions is consistent with these findings.[41–43] Although no binding energies has been reported experimentally, the interaction features can be interpreted as a chemisorption situation on the basis of the corrugation values in Ref. 40 and 43.

The optB88-vdW method, however, reports physisorption situations only (**Figure 5.9**). By “manually” placing the monolayer close to the Ni substrate and by using a quasi-Newton algorithm to relax the ions, optB88-vdW functional is able to capture a chemisorption minimum. In this local minimum, the corrugation value is estimated as 7.2 pm with the B atom closer to Ni substrate, in good agreement with the XPD measurments.[40] Moreover, the calculated interlayer separation *h*-BN monolayer-Ni is 221 pm, in line with and LEED[39] and TEM[43] reports. In order to corroborate this interface configuration is in fact a stable local minimum, the nudged band elastic (NEB) method was used. Such results are showed in **Figure 5.10**. The two minima differ by ~10.0 meV/atom with a small energy barrier of ~1.6 meV/atom.

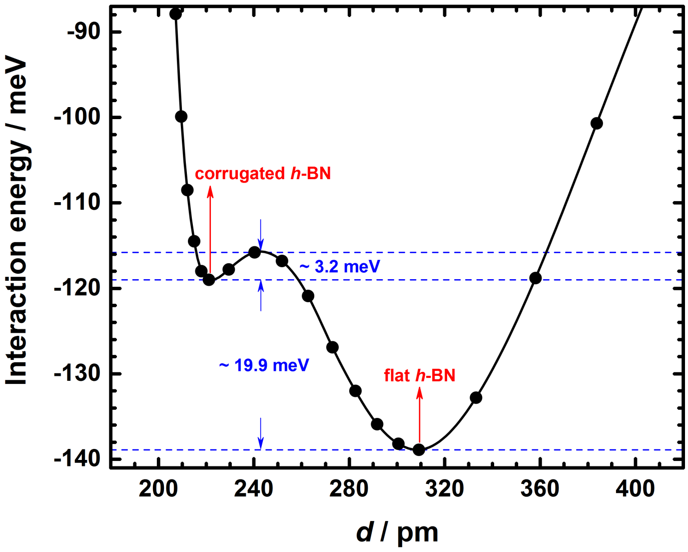

**Figure 5.10** Interaction energy (per BN formula unit) as a function of the average separation *d* between the Ni substrate and the monolayer *h*-BN, as calculated for the N(*top*)-B(*fcc*) configuration, using the optB88-vdW functional. The saddle points were located by means of NEB calculations.

The presence of the two minima in the simulations might be due to two types of interactions happening in here. On the one hand, there is the dispersion (vdW) interaction, which is responsible for the “flat *h*-BN” minimum (on the right in **Figure 5.10**). On the other hand, as the separation between the *h*-BN and the Ni substrate becomes short, chemical bonding begins to play an important role in the interaction, leading to a "corrugated *h*-BN" monolayer. Interestingly, although most recent experimental work has identified the state of *h*-BN on Ni{111} as chemisorbed (Gamou *et al.*, Auwärter *et al.*, and Tonkikh *et al.*)[39,40,43], an earlier study argued that the adsorption state was physisorbed (Nagashima and coworkers).[45]

However, the sign of the relative energy by optB88-vdW method regarding a "corrugated *h*-BN" structure (chemisorption situation) and a "flat *h*-BN" conformation (physisorption) is incorrect, as one should expect the chemisorbed state to have a lower energy. In fact, Janthon *et al.*[46] have reported the same implausible behavior of the optB88-vdW functional in the description of the graphene/Ni{111} interface. These authors also found that the optB86b-vdW functional does lead to the expected behavior, clearly favoring chemisorption over physisorption on Ni{111}, and also providing a correct description of geometries and adsorption energies of chemisorbed and physisorbed states.

We have therefore investigated the relative adsorption strength at the chemisorbed and physisorbed states for the *h*-BN/Ni{111} system with the optB86b-vdW functional, as well as with the empirically-corrected (Grimme's) functionals PBE-D2 and PBE-D3, and the results are listed in **Table 5.3**. Interestingly, all of the functionals predict the existence of both local minima. The formation of the interface, in either the physisorbed or chemisorbed state, is energetically favorable (negative formation energy) for all functionals except for PBE (which cannot account for the stabilizing dispersion interactions, letting the strain effect to dominate). Moreover, the only functional that correctly identifies the chemisorbed state as more stable than the physisorbed one is the optB86b-vdW functional, as observed for graphene/Ni{111}.[46] The optB88-vdW functional, which we found to be particularly good in the description of free-standing *h*-BN, can find the chemisorbed minimum on Ni{111}, but it does not identify it as the global minimum for adsorption. However, for compatibility with the first part of this chapter, and to facilitate comparison between the free-standing and supported systems, we will discuss below the addition of extra layers and the Raman frequencies of supported *h*-BN as calculated with the optB88-vdW (at the correct chemisorbed minimum).

**Table 5.3** Corrugation and adsorption energies of the chemisorbed and physisorbed interface geometries for the *h*-BN/Ni{111} system, according to the listed functionals.

| Functional | Chemisorption | | Physisorption | |
|---|---|---|---|---|
| | corrugation (pm) | $E_{\mathrm{int}}$ (meV/atom) | corrugation (pm) | $E_{\mathrm{int}}$ (meV/atom) |
| **PBE** | 10.3 | 11.2 | 0.1 | 3.4 |
| **PBE-D2** | 11.3 | -54.9 | 2.2 | -88.2 |
| **PBE-D3** | 10.4 | -29.3 | 1.4 | -68.8 |
| **optB88-vdW** | 7.2 | -59.5 | 0.8 | -69.5 |
| **optB86b-vdW** | 9.9 | -84.0 | 1.4 | -62.0 |

**Table 5.4** shows the optimization results of few-layers, up to 3 ML, of *h*-BN on the Ni{111} surface. The increase in absolute value of $E_{\mathrm{int}}$ indicates that the deposition of extra *h*-BN monolayers should be a favorable process. The higher values in the predicted interlayer separation in bi- and tri-layers indicates a decoupling from the underlying substrate, which indicates the presence of two regions with distinctive properties. Experimental studies by Rokuta *et al.*[38] have demonstrated that orbital hybridization at the Ni{111} and *h*-BN nanosheets interface generates metallic bands. The experimental and theoretical work of multilayers *h*-BN on Ni{111} by Tonkikh and co-workers[43] also reported that the first *h*-BN layer at the interface to Ni is metallic. Furthermore, these authors found a decoupling of the second layer from the underlying substrate, which leads

to the restoring of the insulating nature of *h*-BN system. The computed density of states (DOS) projected on the *h*-BN (**Figure 5.11**) follows the same trend, in excellent agreement with the experiment reported in Ref. 43: the interface layer exhibits a metallic behavior whereas the surface layer (and second layer in case of the tri-layer system) has the same features to that of a free-standing (unstrained) BN sheet.

**Table 5.4** Average interlayer separation $d$ and interaction energy $E_{\text{int}}$ of mono-, bi- and tri-layers of *h*-BN supported on Ni{111} surface.

| **System** | **Interlayer separation $d$ (pm)** | | | **$E_{\text{int}}$ (meV/atom)** |
|---|---|---|---|---|
| | **Ni - 1st ML** | **1st - 2nd ML** | **2nd – 3rd ML** | |
| **1 ML** | 221 | - | - | -59.5 |
| **2ML** | 221 | 327 | - | -74.5 |
| **3ML** | 221 | 325 | 330 | -72.9 |

Finally, we discuss the calculated Raman frequency (1421.5 $\text{cm}^{-1}$) of the metal-supported *h*-BN monolayer in comparison with that of the free-standing system (1394.3 $\text{cm}^{-1}$) at its equilibrium cell parameter. The value for the supported system is larger, which is partially expected from the findings presented at the beginning of the Chapter: the in-plane compression associated with the interface formation should lead to an increase in the frequency of the in-plane modes. However, the difference (27.2 $\text{cm}^{-1}$) cannot be explained only on the basis of the associated contraction: the Raman frequency of a free-standing *h*-BN layer, compressed to match the cell parameter of Ni{111}, is 1402.0 $\text{cm}^{-1}$, which represents an increase of only 7.7 $\text{cm}^{-1}$ with respect to the uncompressed system. Therefore, there is clearly a "direct" support-induced effect, which produces most of the Raman frequency upshift. This effect is likely to be related to the charge transfer from Ni to BN, which alters the rigidity of the in-plane BN bonds.

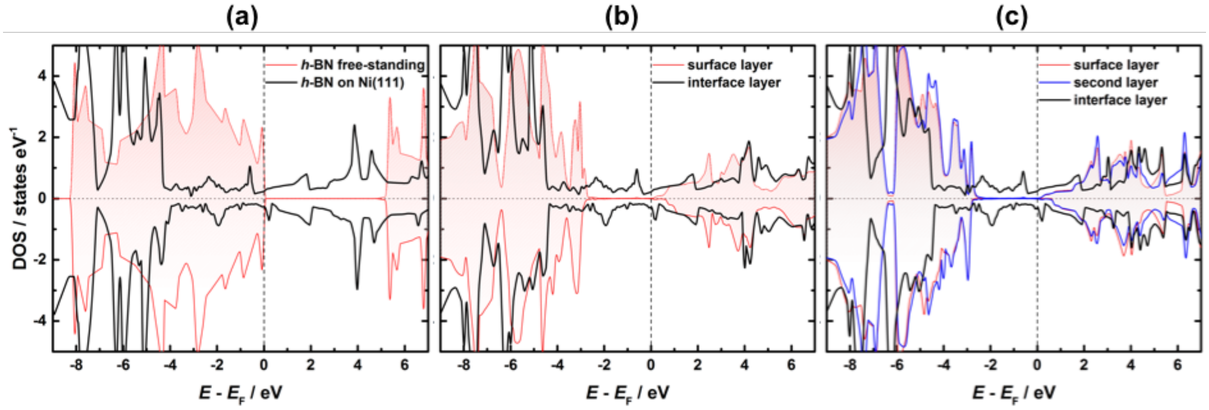

**Figure 5.11** Layered resolved density of sates (DOS) for (a) mono- (b) bi- and (c) tri-layers of *h*-BN supported on Ni{111} surface. Panel (a) exhibits also the DOS computed for a free-standing (unstrained) monolayer.

The latter finding is important for understanding the Raman signature of *h*-BN monolayers in supported systems. We have shown before that there is a small intrinsic signature, i.e. a difference in Raman frequency between bulk and monolayer that is not due to support effects, but support-induced effects appear to be dominant. The results above indicate that the influence of the support cannot be simply reduced to interface strain effects: direct interactions, in the form of charge transfer and chemisorption, may constitute the dominant effect determining the magnitude of the Raman shift. Therefore, a detailed understanding of the nature of the *h*-BN/support interaction is necessary to elucidate the origin of Raman shifts in specific supported *h*-BN systems.

## 5.4 CONCLUSIONS

In summary, new insights into the origin of the Raman signature of *h*-BN monolayer (difference in Raman frequency with respect to the bulk) have been proposed. First, we have demonstrated that the origin of the Raman signature in unsupported systems is clearly related to a difference in the in-plane cell parameter between the bulk and the monolayer. We prefer this statement over the conclusion (e.g., in Ref. 15) that the Raman frequencies are determined by the level of strain. The bulk and the single layer have slightly different equilibrium cell parameters, which means that both systems will have different Raman frequencies in the absence of strain. Our calculations show that the "direct" effect of inter-layer interactions on Raman frequency (i.e. the effect arising without considering the difference in cell parameter) is very small; most of the effect arises from the lattice contraction.

We have shown that the best dispersion-corrected functionals (those with explicit non-local correlation) indeed predict, in a zero-temperature calculation, a contraction of lattice parameter from bulk to monolayer that can quantitatively explain the Raman shift observed in supported samples. While this could be at first interpreted as a confirmation of the existence of an intrinsic Raman shift, the simulation of the behavior at finite temperatures add a caveat: it was showed that the different thermal expansion of bulk and monolayer partially "erases" the intrinsic Raman signature. Our final conclusion of a weak intrinsic Raman signature is in agreement with the most recent experimental results using suspended samples by Cai *et al.*[15], and tend to support the conclusion by these authors that the stronger Raman signature in supported samples is predominantly a substrate-induced effect.

Finally, we have demonstrated that non-local correlation functional predict the presence of two minima in the interaction energy between *h*-BN and Ni{111}: one geometrically flat that can be identified as a physisorbed state and, one with appreciable corrugation of the *h*-BN lattice and shorter interface distance, which can be identified as a chemisorbed state. In the chemisorbed state, which is the one reported in most experiments, there is a significant charge transfer from Ni to BN, which we have found to result in a large increase in the Raman frequency of the supported *h*-BN. This "direct" effect is stronger than the "indirect" effect due to the lattice contraction associated with the interface formation.

## 5.5 REFERENCES

1 J. Ontaneda, A. Singh, U. V Waghmare and R. Grau-Crespo, *J. Phys. Condens. Matter*, 2018, **30**, 185701.

2 T. Ishii, T. Sato, Y. Sekikawa and M. Iwata, *J. Cryst. Growth*, 1981, **52**, 285–289.

3 D. Golberg, Y. Bando, Y. Huang, T. Terao, M. Mitome, C. Tang and C. Zhi, *ACS Nano*, 2010, **4**, 2979–93.

4 C. Lee, Q. Li, W. Kalb, X.-Z. Liu, H. Berger, R. W. Carpick and J. Hone, *Science*, 2010, **328**, 76–80.

5 A. F. Young, C. R. Dean, I. Meric, S. Sorgenfrei, H. Ren, K. Watanabe, T. Taniguchi, J. Hone, K. L. Shepard and P. Kim, *Phys. Rev. B*, 2012, **85**, 235458.

6 C. R. Dean, A. F. Young, I. Meric, C. Lee, L. Wang, S. Sorgenfrei, K. Watanabe, T. Taniguchi, P. Kim, K. L. Shepard and J. Hone, *Nat. Nanotechnol.*, 2010, **5**, 722–6.

7 L. Song, L. Ci, H. Lu, P. B. Sorokin, C. Jin, J. Ni, A. G. Kvashnin, D. G. Kvashnin, J. Lou, B. I. Yakobson and P. M. Ajayan, *Nano Lett.*, 2010, **10**, 3209–15.

8 L. Britnell, R. V Gorbachev, R. Jalil, B. D. Belle, F. Schedin, M. I. Katsnelson, L. Eaves, S. V Morozov, A. S. Mayorov, N. M. R. Peres, A. H. C. Neto, J. Leist, A. K. Geim, L. A. Ponomarenko and K. S. Novoselov, *Nano Lett.*, 2012, **12**, 1707–10.

9 P. Blake, E. W. Hill, A. H. Castro Neto, K. S. Novoselov, D. Jiang, R. Yang, T. J. Booth and A. K. Geim, *Appl. Phys. Lett.*, 2007, **91**, 063124.

10 A. C. Ferrari, J. C. Meyer, V. Scardaci, C. Casiraghi, M. Lazzeri, F. Mauri, S. Piscanec, D. Jiang, K. S. Novoselov, S. Roth and A. K. Geim, *Phys. Rev. Lett.*, 2006, **97**, 187401.

11 R. V. Gorbachev, I. Riaz, R. R. Nair, R. Jalil, L. Britnell, B. D. Belle, E. W. Hill, K. S. Novoselov, K. Watanabe, T. Taniguchi, A. K. Geim and P. Blake, *Small*, 2011, **7**, 465–8.

12 S. N. Shirodkar, U. V. Waghmare, T. S. Fisher and R. Grau-Crespo, *Phys. Chem. Chem. Phys.*, 2015, **17**, 13547–13552.

13 F. A. Rasmussen, P. S. Schmidt, K. T. Winther and K. S. Thygesen, *Phys. Rev. B*, 2016, **94**, 155406.

14 R. Arenal, A. C. Ferrari, S. Reich, L. Wirtz, J.-Y. Mevellec, S. Lefrant, A. Rubio and A. Loiseau, *Nano Lett.*, 2006, **6**, 1812–6.

15 Q. Cai, D. Scullion, A. Falin, K. Watanabe, T. Taniguchi, Y. Chen, E. J. G. Santos and L. Li, *Nanoscale*, 2017, **9**, 3059–3067.

16 G. Kresse and J. Furthmüller, *Comput. Mater. Sci.*, 1996, **6**, 15–50.

17 G. Kresse and J. Furthmüller, *Phys. Rev. B*, 1996, **54**, 11169–11186.

18 P. E. Blöchl, *Phys. Rev. B*, 1994, **50**, 17953–17979.

19 G. Kresse and D. Joubert, *Phys. Rev. B*, 1999, **59**, 1758–1775.

20 G. P. Francis and M. C. Payne, *J. Phys. Condens. Matter*, 1990, **2**, 4395–4404.

21 H. J. Monkhorst and J. D. Pack, *Phys. Rev. B*, 1976, **13**, 5188–5192.

22 R. S. Pease, *Acta Crystallogr.*, 1952, **5**, 356–361.

23 J. P. Perdew and A. Zunger, *Phys. Rev. B*, 1981, **23**, 5048–5079.

24 J. P. Perdew, K. Burke and M. Ernzerhof, *Phys. Rev. Lett.*, 1996, **77**, 3865–3868.

25 S. Grimme, *J. Comput. Chem.*, 2006, **27**, 1787–99.

26 S. Grimme, J. Antony, S. Ehrlich and H. Krieg, *J. Chem. Phys.*, 2010, **132**, 154104.

27 M. Dion, H. Rydberg, E. Schröder, D. C. Langreth and B. I. Lundqvist, *Phys. Rev. Lett.*, 2004, **92**, 246401–1.

28 K. Lee, É. D. Murray, L. Kong, B. I. Lundqvist and D. C. Langreth, *Phys. Rev. B*, 2010, **82**, 081101.

29 J. Klimeš, D. R. Bowler and A. Michaelides, *J. Phys. Condens. Matter*, 2010, **22**, 022201.

30 J. Klimeš, D. R. Bowler and A. Michaelides, *Phys. Rev. B*, 2011, **83**, 195131.

31 N. Mounet and N. Marzari, *Phys. Rev. B*, 2005, **71**, 205214.

32 W. Paszkowicz, J. B. Pelka, M. Knapp, T. Szyszko and S. Podsiadlo, *Appl. Phys. A Mater. Sci. Process.*, 2002, **75**, 431–435.

33 L. A. Girifalco and M. Hodak, *Phys. Rev. B*, 2002, **65**, 125404.

34 M. Hasegawa and K. Nishidate, *Phys. Rev. B*, 2004, **70**, 205431.

35 G. Graziano, J. Klimeš, F. Fernandez-Alonso and A. Michaelides, *J. Phys. Condens. Matter*, 2012, **24**, 424216.

36 J. W. Jiang, B. S. Wang, J. S. Wang and H. S. Park, *J. Phys. Condens. Matter*, 2015, **27**, 083001.

37 R. W. G. Wyckoff, *Crystal Structures, Volume 1*, Interscience Publishers, New York, Second., 1963.

38 E. Rokuta, Y. Hasegawa, K. Suzuki, Y. Gamou, C. Oshima and A. Nagashima, *Phys. Rev. Lett.*, 1997, **79**, 4609–4612.

39 Y. Gamou, M. Terai, A. Nagashima and C. Oshima, *Sci. Reports Rerearch Institutes Tohoku Univ. Ser. A-Physics*, 1997, **44**, 211–214.

40 W. Auwärter, T. J. Kreutz, T. Greber and J. Osterwalder, *Surf. Sci.*, 1999, **429**, 229–236.

41 A. H. M. A. Wasey, S. Chakrabarty, G. P. Das and C. Majumder, *ACS Appl. Mater. Interfaces*, 2013, **5**, 10404–10408.

42 X. Gao, S. Wang and S. Lin, *ACS Appl. Mater. Interfaces*, 2016, **8**, 24238–24247.

43 A. A. Tonkikh, E. N. Voloshina, P. Werner, H. Blumtritt, B. Senkovskiy, G. Güntherodt, S. S. P. Parkin and Y. S. Dedkov, *Sci. Rep.*, 2016, **6**, 23547.

44 W. Zhao, S. M. Kozlov, O. Höfert, K. Gotterbarm, M. P. A. Lorenz, F. Viñes, C. Papp, A. Görling and H. P. Steinrück, *J. Phys. Chem. Lett.*, 2011, **2**, 759–764.

45 A. Nagashima, N. Tejima, Y. Gamou, T. Kawai and C. Oshima, *Phys. Rev. Lett.*, 1995, **75**, 3918–3921.

46 P. Janthon, F. Viñes, S. M. Kozlov, J. Limtrakul and F. Illas, *J. Chem. Phys.*, 2013, **138**, 244701.

# Concluding remarks and future work

The work presented in the different chapters of this thesis had the common theme of metal surfaces in interaction with different environments. The second common theme of the thesis is the synergy between theory and experiment in the investigation of such interactions. Not only we have calculated the electronic and geometric properties of these interfaces, but we have also attempted to simulate the output from different experimental techniques, in particular X-ray photoelectron spectroscopy (XPS), and to some extent near edge X-ray absorption fine structure (NEXAFS) and Raman too. This has led to a more direct comparison between theory and experiment, and an increased synergy between the two approaches.

For example, the XPS data on methyl acetoacetate (MAA) adsorbed on Ni surfaces was not enough on its own, or even in combination with NEXAFS, to elucidate the preferred adsorption mode. The theoretical calculation of adsorption energies for different modes was not sufficient either, because some modes of adsorption (e.g. those involving adatom formation) are kinetically hindered, or because different modes are of similar adsorption strength. However, by putting together the experimental and simulated XPS data for the most stable modes, it was possible to unambiguously elucidate the dominant adsorption geometry for two different Ni surfaces.

Similarly, the electronic structure of the Pd/Re(0001) interface could only be understood properly after our Density Functional Theory (DFT) calculations, which were motivated, and ended up explaining, existing XPS data on this system. Our theoretical work led to a general model of analogy between charge transfer and strain in the electronic properties of bimetallic interfaces.

Finally, the work on hexagonal boron nitride (*h*-BN) and its interaction with the Ni{111} surface was also focused on a particular type of experimental measurement of this system: the Raman spectrum. The problem of the Raman signature of the *h*-BN monolayer led us to interesting and useful insights about the physics of the interactions between boron nitride layers, and between boron nitride and the Ni support.

This good synergy between experiment and theory allowed us to tackle the complex phenomena happening on the surface of the metal-based systems examined here. Of course, other similar problems can be tackled through the combination of XPS, NEXAFS and Raman with DFT simulations. After all, output from DFT-simulated spectroscopic techniques has been proved to be reliable and of enormous help. Therefore, future work includes the applicability of the same methodology in order to fill some of the gaps still present in the comprehension of these systems.

For instance, the enantioselective hydrogenation of bio-related molecules over Ni surfaces requires surface chiral modifiers to lead the otherwise racemic-mixture reaction towards a high enantiomeric excess. A step forward, therefore, would be to investigate the co-adsorption of MAA and the simplest surface chiral modifier, alanine, on Ni surfaces. Other well-known modifier molecules are tartaric acid and glutamic acid, and it would be useful to consider them too. These studies would enable us to determine the exact geometry of the modifier-MAA complex at the molecular level and consequently establish the reaction mechanism where one enantiomer is favored over the other. As this co-adsorption mechanism can be even more complex than that of MAA alone, core-level shift calculations should be helpful in the assignment of peaks in the XPS spectra.

The proposed mechanism of charge transfer discussed in Chapter 4 can be useful to explain the core and valence electronic structure of some bimetallic interfaces. However, such a mechanism is currently limited to heteroepitaxial systems with negligible strain. The future work, therefore, should be extended to investigate the role of charge transfer in heteroepitaxial systems where strain is not negligible. A good case of study could be the deposition of thin films of Pt on Ru(0001) surfaces. These studies might help to improve the mechanism of the *d*-band center and its role in determining the strength of adsorption of atoms and molecules on metal surfaces. In a similar fashion, core-level shift calculations can be used as evidence of the reliability of DFT output.

Chapter 5 discussed the “direct” Ni support effect on the upshift in the Raman signature of monolayer *h*-BN. While this is likely related to the net charge transfer from Ni to *h*-BN, the actual details of the mechanism have yet to be determined. One of the more important future extensions of this part of the work will involve the consideration of more “inert” supports, so we can fully understand the support-induced effect on the Raman signature of *h*-BN. Good candidates can be substrates based on $SiO_2$. It would also be nice to extend the current simulations to address some potential applications of the *h*-BN/metal interface; for example, the catalytic properties of metal-supported *h*-BN.

We hope that the contributions and suggestions presented in this thesis will stimulate further experiment-theory collaborative work towards a more complete understanding of these phenomena.